Laboratory and Computational Evaluation of Mast Arm Foundations Under Torsion and Lateral Loading

by

Olga L. Rojas Esparza

A dissertation submitted to the Graduate Faculty of
Auburn University
in partial fulfillment of the
requirements for the Degree of
Doctor of Philosophy

Auburn, Alabama
August 8, 2026

Keywords: drilled shaft foundations, lateral loading, torsional loading, soil-pile interaction

Approved by

J. Brian Anderson, Chair, Elton Z. & Lois G. Huff Endowed Professor, Department of Civil and Environmental Engineering
Jack Montgomery, Alice H. & John M. Ozier Associate Professor, Department of Civil and Environmental Engineering
James S. Davidson, Professor, Department of Civil and Environmental Engineering
Jorge Rueda Benavides, David Dixon Associate Professor, Department of Civil and Environmental Engineering
Sheena C. Stewart, Director of Professional Development, Graduate School

Abstract

Drilled shaft foundations are commonly used to support traffic signal mast arm structures because of their ability to resist large lateral, overturning, and torsional loads. Although current design procedures generally evaluate lateral and torsional loading independently, field observations and previous research indicate that these loading modes may interact, particularly under extreme wind events. This study investigates the behavior of drilled shaft foundations subjected to pure torsional, pure lateral, and combined lateral-torsional loading through a comprehensive program of full-scale testing and numerical modeling.

Seven full-scale load tests were performed on two 36-in-diameter drilled shafts constructed within a controlled geotechnical chamber at Auburn University. The testing program included pure torsional loading, pure lateral loading, combined lateral-torsional loading, and sequential loading cases in two distinct phases. In Phase I, shafts were constructed in place through excavation and concrete placement. In Phase II, the shafts were exhumed, reinstalled, and surrounded by recompacted sand to evaluate the influence of construction method and shaft-soil interface conditions. Load, displacement, rotation, and strain measurements were collected throughout the testing program.

The experimental results showed that torsional and lateral behavior are strongly influenced by loading sequence and shaft installation conditions. Pure torsional tests in both phases yielded similar ultimate torsional capacities of approximately 145-148 kip-ft; however, the recompacted Phase II configuration exhibited substantially higher initial torsional stiffness. Combined lateral-torsional loading reduced the mobilized torsional

stiffness and altered the progression of resistance mobilization, requiring larger rotations to achieve the same torque levels observed under pure torsion. Sequential loading tests indicated that prior torsional loading reduced lateral stiffness and delayed the mobilization of resistance, although differences in ultimate lateral capacity were less pronounced.

Numerical models were developed using FB-MultiPier and back-calculated against the measured load-displacement and torque-rotation responses. The best-fit estimation demonstrated that stiffness-related parameters, particularly shear modulus and horizontal subgrade reaction, were highly sensitive to construction effects, loading history, and stress path. Strength-related parameters, including unit weight, friction angle, and torsional shear resistance, exhibited comparatively smaller adjustments. The results demonstrate that conventional uncoupled design approaches do not adequately represent the behavior of drilled shafts under realistic loading conditions and highlight the need to consider construction effects, shaft-soil interface conditions, and load interactions in foundation design for mast arm structures.

Artificial Intelligence (AI) Use Disclosure Statement

In the preparation of this dissertation, the following Artificial Intelligence (AI) tools were used: Grammarly, ChatGPT, and Copilot. These tools were mainly employed to verify document writing and locate references online. The author acknowledges full responsibility for the intellectual content of this work and has ensured that all AI-assisted sections have been reviewed and revised for accuracy and appropriate academic style. All AI-generated content was reviewed and validated for relevance, appropriateness, and accuracy before incorporation into the final document to maintain scholarly integrity of this research.

Digital Accessibility Disclosure Statement

In the preparation of this dissertation, the following digital accessibility tool was used to ensure this document complies with federal requirements: Accessibility check in Microsoft Word. The author acknowledges full responsibility for the intellectual content of this work and has made a good faith effort to comply with digital accessibility requirements in publishing, wherein the nature of the content does not significantly change in order to do so. Furthermore, all content has been reviewed and revised to meet these requirements prior to final publication.

Acknowledgments

To the Creator of the universe and everything beyond it, who provided me with the energy I needed to complete this part of my journey in this world.

I want to thank the many people who nurtured my life with guidance, support, and friendship. To my advisor and committee chair, Dr. Brian Anderson, thank you for your teachings, from which I learned so much, and for your support throughout this journey. To my committee members, Dr. Montgomery, Dr. Davidson, and Dr. Rueda, I greatly appreciate the wealth of knowledge you shared with me through your classes and meetings. I would also like to thank Dr. Sheena Stewart for agreeing to read my dissertation and serve on my committee, and for starting to cheer for me right after I met her.

I would like to thank the Alabama Department of Transportation for funding this project and for collaborating on the in-situ testing. I also want to thank the staff at the Advanced Structural Engineering Laboratory for providing such wonderful support during the testing phase of this research.

To my dear girlfriends, who filled my soul with support and love, served as a key source of strength that helped me get through the difficult times of this journey, and shared countless wonderful moments with me, I am deeply grateful.

I want to express my gratitude to my family in my home country for their unwavering support over the years, and especially to my mom for showing me that education is the key to freedom and the possibility to become anyone I aspire to be.

I am thankful for the opportunity life gave me to find a group of incredible friends whom I can call family in a place far away from home.

I also want to thank my colleagues for their support throughout these five years.

Finally, I want to thank the Creator for unexpectedly bringing fur babies into my life, filling it with unconditional love and an unparalleled feeling of safety.

Table of Contents

List of Tables

List of Figures

CHAPTER 1. Introduction

1.1. Background of Mast Arm Structures

Transportation infrastructure requires support structures for traffic signals and other equipment, including signs, sensors, and cameras. As vital elements of transportation systems, support structures must uphold their reliability, even in critical circumstances. Consequently, these structures are designed to ensure clear visibility, durability, and resistance to environmental factors, seismic activity, and vehicle impacts.

The design of traffic signal support structures requires the consideration of important factors such as wind loads, vibration and fatigue, seismic loads, material selection, and foundation design. Severe weather events like hurricanes for example, place considerable lateral and torsional stress on these structures and their foundations. Therefore, an effectively designed traffic signal support structure needs to incorporate structural, geotechnical, and environmental factors to guarantee safe and dependable operation over its lifespan.

The selection of an appropriate support structure depends on the specific site characteristics and the functional requirements of the installation. Typical configurations include strain poles, cantilever structures (e.g. mast arms), overhead sign structures, and pedestal poles. Strain poles and pedestal poles are typically employed in urban areas where space constraints require more compact designs. Conversely, cantilever structures, and overhead sign structures are commonly found in high-traffic corridors and major intersections, where drivers require clear visibility of traffic signals.

Mast arm structures consist of a vertical pole, which serves as the primary support element. This pole is anchored to the foundation, transferring loads to the soil.

Its height is determined to ensure visibility and clearance for large vehicles. Additionally, the pole must withstand the bending moments induced by the loads acting on the mast arm. The second component of a mast arm structure is the horizontal arm (beam) that extends from the vertical pole over the roadway. A schematic representation of a mast arm can be seen in **Figure 1-1**.

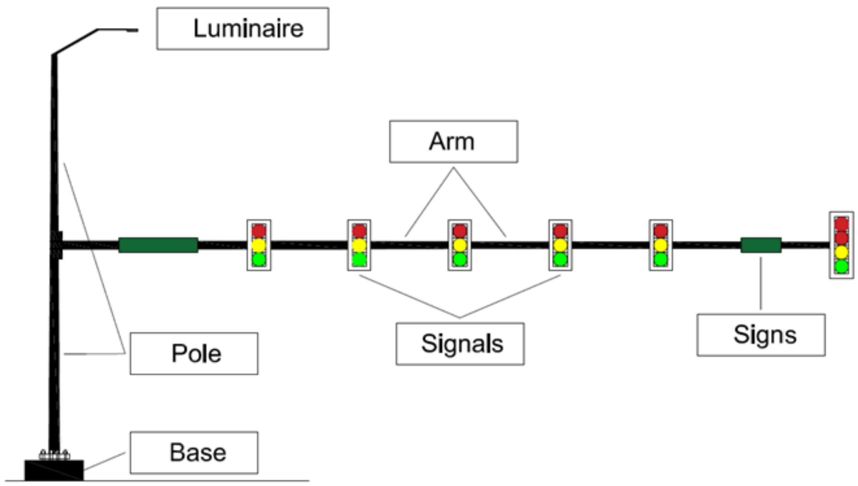

Figure 1-1. Typical Scheme of a Mast Arm (Rodriguez et al., 2020)

The length of the mast arm depends on the number of lanes it spans. Rodriguez et al. (2020) reported the range of mast arm lengths across several states in the USA. The reported lengths range between 10 ft and 80 ft.

1.1.1. Wind Effects on Mast Arm Structures

Wind is one of the most critical dynamic forces acting on mast arm structures, particularly in high-wind regions and hurricane-prone areas. The American Association of State Highway and Transportation Officials – AASHTO – defines the design specifications through the LRFD Specifications for Structural Support for Highway Signs, Luminaires, and Traffic Signals (AASHTO 2015).

Since 2000, the coastal regions of the southeastern United States have been impacted by multiple hurricanes. Mast arm failures during hurricane events have been a concern in the southeastern United States. For example, in 2004, Florida experienced four hurricanes – Charley, Frances, Ivan, and Jeanne – that caused around 20 mast arm failures statewide due to wind loads. While the overall number of such failures is relatively low, studies have identified specific causes and mitigation strategies (Faquir et al. 2005). **Figure 1-2** presents examples of mast arm failures that occurred in Florida in 2024.

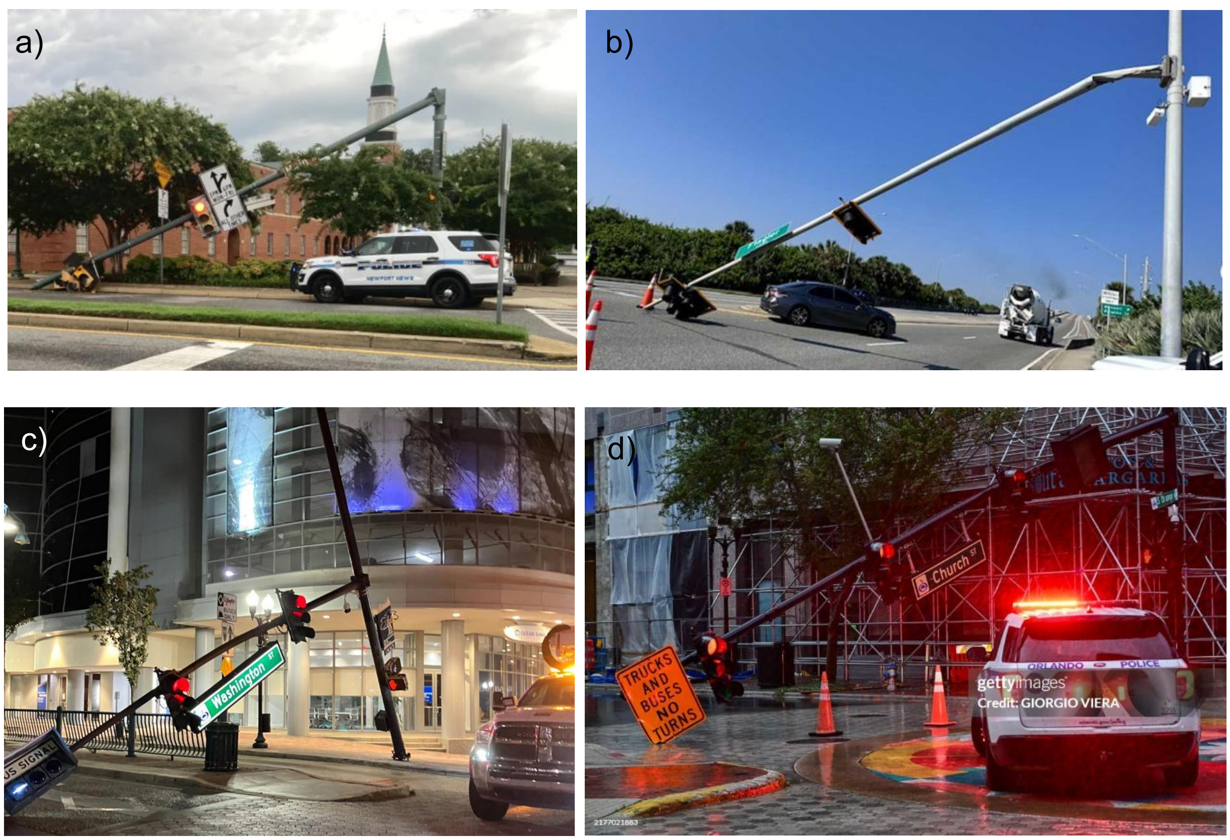

Figure 1-2. Mast Arm Failure in Florida: a) Newport News. Aug. 3, 2024 (The Virginian-Pilot, 2024), b) Flagler Beach, Aug. 14th, 2024 (FlaglerLive, 2024), c) Downtown Orlando, Hurricane Helene 2024 (MSN News, 2024), and d) Downtown Orlando, Hurricane Milton. Oct 10, 2024 (Getty Images, 2024)

The connections in the superstructure are, by design, the weak points of the system. The link between the mast arms and their foundations is crucial for maintaining structural stability, particularly when subjected to severe wind loads. The design of the anchors must facilitate the transfer of loads to the concrete and achieve the necessary tensile strength before any failure of the concrete occurs. Traditional anchor bolt systems have shown vulnerabilities, particularly in terms of concrete breakout (**Figure 1-3**) prompting extensive research into alternative connection methods.

Figure 1-3. Sign Support Structure Failure at the I-75 and SR 17 Interchange, Florida, Due to Hurricane Charley in 2004 (Faquir et al., 2005).

1.1.2. Effects of Wind Loading on the Foundation

The foundation system plays a critical role in the stability of mast arm structures, particularly in coastal and high-wind regions. Dynamic loads, such as wind, create lateral and overturning forces that are transmitted to the foundation (**Figure 1-4**). The foundation also endures moment loading, which can cause rotation of the structure. Potential failure modes that could arise and impact the performance of the mast arm structure are:

a) Loads make the mast arm pole rotate around a vertical axis, potentially impacting the visibility of signs or signage.

b) Loads cause the mast arm pole to rotate around a horizontal axis. When this rotation occurs horizontally, the cantilever arm can obstruct lanes on the roadway or create more critical safety issues, such as colliding with a vehicle at the moment of failure.

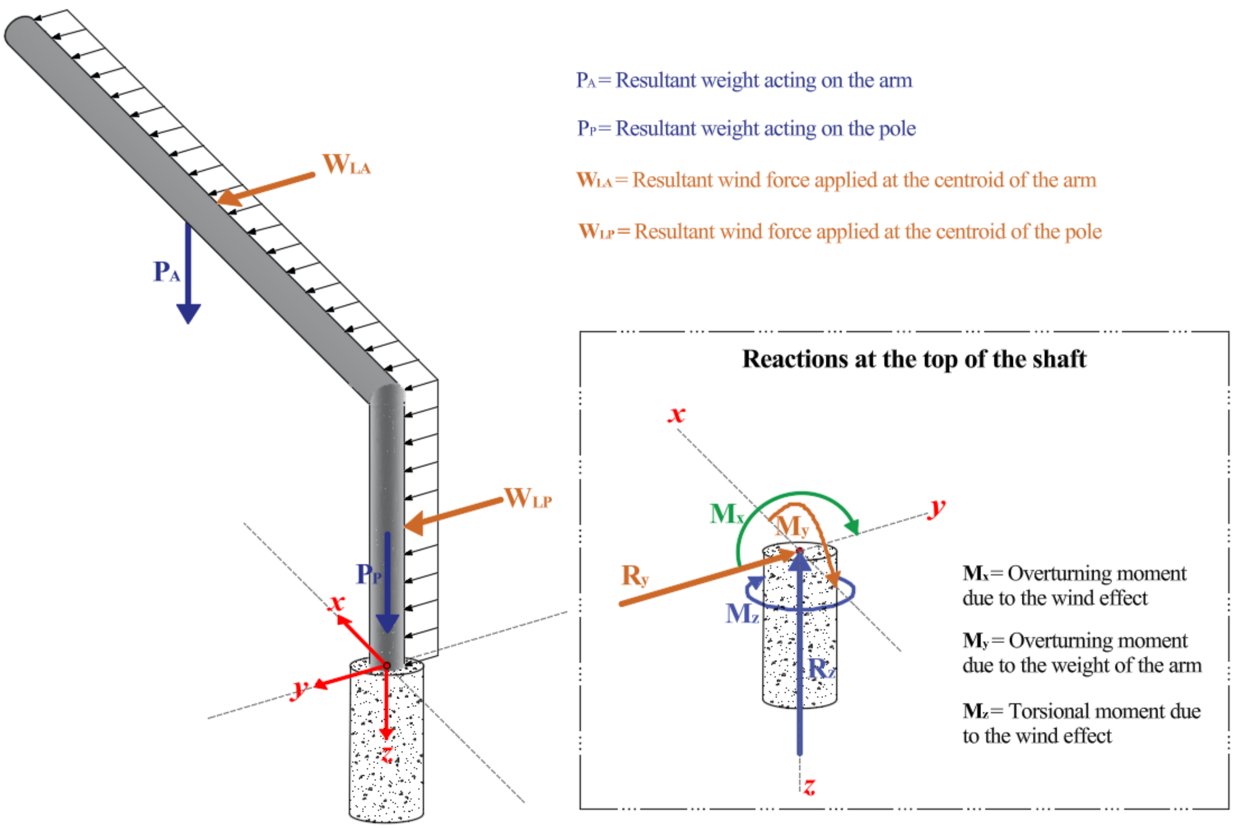

Figure 1-4. Representation of the forces acting on the mast arm and transferred to the shaft.

Drilled shaft foundations are commonly preferred to support mast arms for their strong load-bearing capacity and resistance to lateral and torsional forces. In unfavorable soil conditions or when groundwater levels are elevated, alternative solutions such as micropiles and jet-grouted piles can enhance stability.

1.2. Drilled Shaft Foundations

Drilled shaft foundations are cast-in-place deep foundations constructed by excavating a stabilized hole to place concrete and reinforcing. The diameter of drilled shafts is typically in the range of 3 to 12 feet. This type of foundation is constructed to support axial forces as a combination of side shear and end-bearing resistance. Due to the often substantially large diameter, drilled shafts are also capable of resisting large lateral and overturning forces. Figure 1-5 is a representation of the resistance generated at the shaft-soil interface.

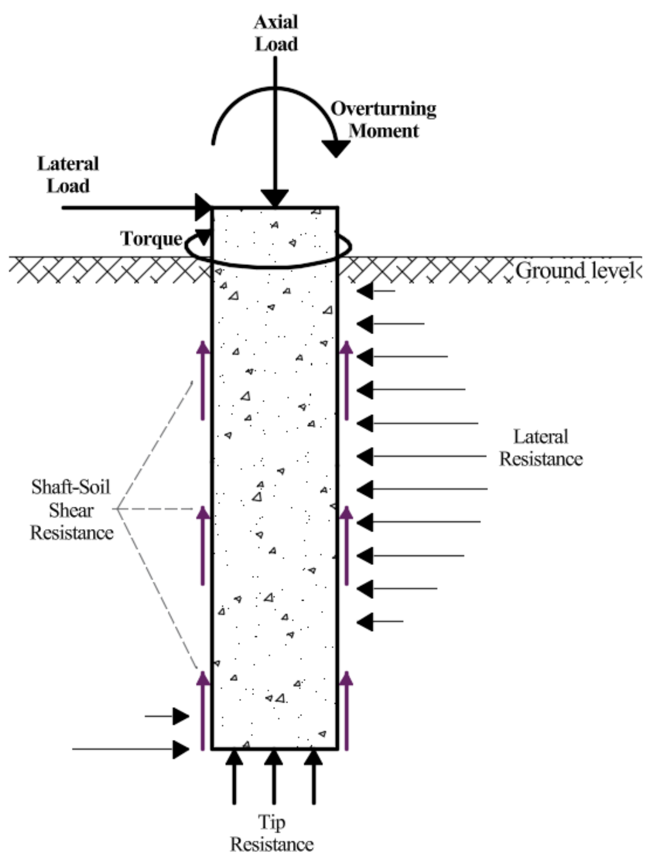

Figure 1-5. Representation of the Resistance of Drilled Shafts.

Considering the significant resistance of drilled shafts to lateral loads, their application is particularly important for mast arm structures, bridges, and transmission towers, where foundation stability is crucial for withstanding wind, seismic, and traffic-induced forces. Drilled shafts are also used to address slope stability issues and to construct earth-retaining structures, such as bridge abutments and highway walls. When drilled vertically, shafts can form walls either by overlapping or being adjacent to one another, and they can also serve as support for conventional walls (Brown et al., 2018)

1.2.1. Design Considerations for Drilled Shafts

The performance of drilled shafts is governed by axial capacity, lateral resistance, and torsional strength, all of which depend on soil properties, load combinations, and construction methods. Brown et al. (2018) provided an in-depth guideline on drilled shaft design based on field testing, numerical modeling, and empirical correlations. The guidelines were developed in accordance with the AASHTO LRFD Bridge Design Specifications (2018). The fundamental aspects of drilled shaft design include:

- **Axial Capacity:** Determined by side shear resistance and end-bearing capacity. Axial capacity predictions rely on in-situ testing such as the Standard Penetration Test (SPT), Cone Penetration Test (CPT), and Pressuremeter Test (PMT), and laboratory tests, such as Triaxial tests. These tests are used to determine the unit side friction resistance, q_s, and ultimate unit end bearing, q_t. While load settlement behavior is not the critical case, it is often modeled using the t-z approach popularized by Coyle and Reese (1966).

- **Lateral Resistance:** Before the widespread acceptance of computational methods, the Broms' approach was used as a simplified method of analysis (Broms 1964a, 1964b). Broms method provided an estimate of maximum lateral load at a service level deflection. Nowadays, the p-y method is the recommended approach for the evaluation of lateral resistance of drilled shafts (Brown et al. 2018). The p-y curves provide a nonlinear approximation of soil-structure interaction by representing the lateral soil response as a series of independent nonlinear springs. These curves relate the soil reaction (p) to lateral deflection (y) at discrete depths of the shaft. They can be used to estimate bending moments, shear forces, and lateral deflections for different soil condition profiles.
- **Torsional Resistance:** The torsional resistance of drilled shafts is approached similarly to lateral resistance. The torsional response is represented by independent nonlinear springs (τ-θ) (Randolph, 1981). A maximum torsional shear resistance is determined in a similar way to the axial side friction. Several methods have been developed for determining the peak shear capacity. Aguilar (2018) reported three torsional failure criteria based on previous research. The first failure criterion occurs when the shear stress no longer increases, but the rotation continues to rise. The second failure criterion is based on traffic sign support serviceability requirements, with a 15-degree twist angle. The third proposed failure criterion is the sum of the shaft's elastic torsional deformation and the toe twist angle. Aguilar (2018)

also presented a review of methods for determining the nominal torsional resistance of drilled shafts, which is summarized below.

Cohesive soil

- *α method (O'Neill and Reese 1999)*

$T_s = \frac{1}{2}\pi D^2 \int_0^L f_s(z)dz$, where $f_s = \alpha s_u$ (1)

s_u = undrained shear strength of the soil

α = adhesion factor

= 0 for a length of 5 ft (1.52 m) at head of the shaft

= 0 for a length of D just above shaft toe

$\alpha = 0.55 for \frac{s_u}{p_a} \leq 1.5$ (2)

$\alpha = 0.55 - 0.1\left(\frac{s_u}{p_a} - 1.5\right) for 1.5 \leq \frac{s_u}{p_a} \leq 2.5$ (3)

- *Colorado DOT (Stuedlein et al. 2016)*

$T_s = \frac{1}{2}\pi D^2 (L - 1.5D) f_s$, where $f_s = s_u$ (4)

- *Florida DOT (FDOT 2012)*

$T_s = \frac{1}{2}\pi D^2 (L - 1.5) f_s$, where $f_s = 0.55 s_u$ (5)

Cohesionless soil

- *β method (O'Neill and Reese 1999)*

$f_s = \beta\sigma_v^{'} \leq 600ksf$, for $0.25 \leq \beta \leq 1.2$ (6)

$\beta = 1.5 - 0.135\sqrt{z}$, for $N_{60} \geq 15$ (7)

$\beta = \frac{N_{60}}{15}\left(1.5 - 0.135\sqrt{z}\right)$, for $N_{60} < 15$ (8)

- *Colorado DOT (Stuedlein et al. 2016)*

$T_s = \frac{1}{2}\pi D^2 L f_s$, where $f_s = K\sigma_v^{'} \tan\delta$ (9)

K = coefficient of lateral earth pressure

δ = soil-concrete interface friction angle

$$K = \frac{2L}{3D}\left(1 - \sin\phi'\right) \quad (10)$$

- *Florida DOT (FDOT 2017)*

$T_s = \frac{1}{2}\pi D^2 L f_s$ where $f_s = \sigma'_{vz}\omega_{fdot}$ (11)

ω_{fdot} = load transfer ratio where the allowable shaft rotation may exceed 10 degrees

ω_{fdot} =1.5 for granular soils where uncorrected SPT N_{values} are 15 or greater.

ω_{fdot} =1.5 N_{value}/15 for uncorrected N_{values} greater than or equal to 5 and less than 15.

- *Florida DOT Structure Design Office (Tawfiq 2000)*

$T_s = \frac{1}{2}\pi D^2 L f_s$ where $f_s = K_0\sigma'_{vz}\tan\delta$ (12)

K_0 = coefficient of lateral pressure at rest

c-φ soils

- *Florida DOT District 7 (Tawfiq 2000)*

$$T_s = \frac{1}{2}\pi D^2 (L - 5) f_s \quad (13)$$

$f_s = \alpha s_u + K\sigma'_{vz}\tan\delta$, where $K_0 < K < 1.75$ (14)

α = adhesion factor as proposed by the α method

1.2.2. Lateral Design of Drilled Shafts

Lateral loading considerations and flexural strength generally influence the diameter of drilled shafts. These factors also determine the embedded length for structures like signs and lighting foundations. The lateral loads affecting drilled shafts for highway structures arise from earth pressure, wind loads, centrifugal and braking forces from vehicles. Additionally, forces from "extreme events" like vessel impacts and earthquakes contribute to these loads (Brown et al. 2018).

Structures such as signs and high mast lighting arms are loaded relatively lightly in the axial direction. However, they are substantially loaded with lateral shear and overturning moments due to wind loads acting against the projected area of the structure, and wind gusts producing transient, often cyclic forces. Forces from vehicle impact may also be a significant design component.

Drilled shaft foundations supporting sign structures can be constructed as two-shaft and single-shaft supports, as shown in **Figure 1-6**. The two-shaft system works as a “push-pull” couple by adding tension to one shaft and compression to the other, while the single-shaft foundation resists the shear and moment produced by wind loading through bending.

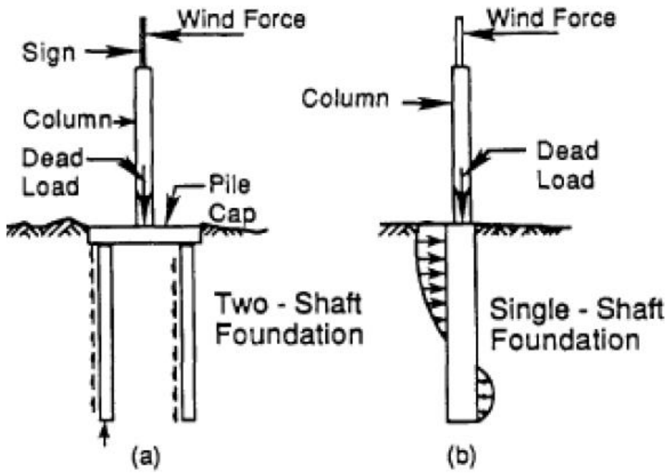

Figure 1-6. Foundation for Sign Structure (a) Two-Shaft Foundation; (b) Single-Shaft Foundation (Brown et al. 2018).

The lateral design of a drilled shaft may be controlled by structural (structural strength limit state) or geotechnical strength conditions (geotechnical strength limit state) or by serviceability requirements (service limit state). For the Structural Strength Limit State, the size of the shaft and reinforcement must provide the required strength to resist all the imposed loads on the drilled shaft, such as shear, axial forces, and bending moments. The Geotechnical Strength Limit State consists of the resistance of the drilled shaft to overturning; the size and depth of penetration of the shaft must be enough to support the factored loads without failing. The most critical case for the geotechnical strength limit is often associated with transient wind or extreme events such as hurricanes (Brown et al., 2018). The Service Limit State refers to deformations; the size and depth of the drilled shaft must be sufficient to keep lateral deformations and rotations within tolerable levels.

The *p-y* method is a widely used approach for analyzing and designing laterally loaded drilled shafts and piles, effectively capturing the nonlinear interaction between soil and structure. It is the recommended method for lateral load design, as it accounts for combined axial and lateral loads, distributed loads from flowing water or creeping soil, nonlinear bending behavior, layered soil conditions, and nonlinear soil response (Brown et al. 2018).

When a lateral load is applied to a drilled shaft, it induces lateral deflection, which in turn generates a soil reaction in the opposite direction. This soil resistance, denoted as p, is a nonlinear function of deflection y, forming what are known as p-y curves (**Figure 1-7**). These curves model the stiffness and strength of the soil, incorporating factors such as shear strength, Young’s modulus, groundwater conditions, shaft diameter, depth, and the nature of loading (static or cyclic).

In numerical modeling, the p-y method replaces the surrounding soil with nonlinear springs, where each depth z along the shaft corresponds to a unique p-y relationship. This approach enables engineers to simulate complex soil-structure interactions and optimize foundation performance under lateral loading conditions.

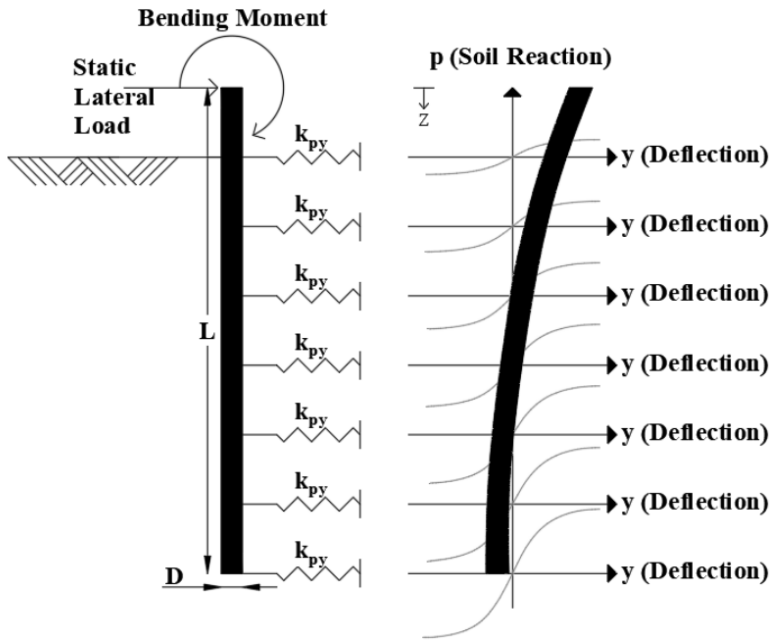

Figure 1-7. Representation of a Drilled Shaft Foundation Under Lateral Loading Conditions (Tommy et al. 2023).

The diameter of the shaft and depth of penetration must be adequate to withstand all the predicted factored design loads without failure. For the geotechnical strength analysis, the p-y method is used on the trial analysis for the diameter and penetration depth of the shaft. Based on Brown et al. (2018), the following considerations are taken for this analysis:

- A simple linear elastic model is used for the shaft (beam element) rather than the nonlinear stress-strain model. Deflections are not a controlling consideration.
- The parameters used for soil modeling are those that better reflect the least favorable conditions of the governing soil.

- The deflections are computed using a type of “pushover analysis”. The lateral loading is applied in multiples of the total design force to evaluate how progressively failure occurs in the structure.
- Although deflections are not considered a controlling parameter of the geotechnical limit state, these must be checked to ensure the computed value is reasonable (10% of the shaft diameter) and the dimensions of the shaft are sufficient for the strength requirements.

A resistance factor is used to ensure the geotechnical strength of the shaft for lateral resistance is enough to satisfy a ductile load response and to provide a reserve strength for site variability and other eventualities. Brown et al. (2018) recommend the resistance factors presented in **Table 1-2**.

Table 1-1. Recommended Geotechnical Strength Limit State Resistance Factors for Lateral Loading of Drilled Shafts (computed using p-y Method). (Brown et al., 2018)

Condition	Resistance Factor, φ
Overturning resistance of an individual or single row of elastic shafts, free to rotate at the head	0.67
Pushover of an elastic shaft within a multiple-row group, with moment connection to the cap	0.8
Extreme event strength cases	0.8

1.2.3. Torsional Design of Drilled Shafts

The torsional loading or twisting forces acting on drilled shaft foundations are derived from asymmetrical wind forces, eccentric loading, and other dynamic events. These external forces generate a moment, causing the shaft to twist around its vertical axis. The interaction between the shaft and the surrounding soil provides torsional resistance, especially through side friction, which, in some cases, is the factor that governs the failure mechanism. Therefore, the diameter of the shaft is crucial for its torsional resistance. Larger diameters result in a greater surface area in contact with the soil, leading to increased torsional resistance. The governing lateral-torsional design of a drilled shaft may depend on the type of structure the foundation is bearing. Drilled shafts supporting bridges will likely be designed to withstand axial or lateral loads. In contrast, the governing design of shafts supporting mast arms used as cantilever signs will possibly be based on the torsional loading component.

The mechanisms governing torsional load transfer in deep foundations remain poorly understood, and no nationally accepted design standard exists for determining the appropriate shaft size to resist torsional loads. There is no mention in the LRFD Specifications for Structural Supports for Highway Signs, Luminaires, and Traffic Signals – AASHTO (2015), or the Drilled Shafts: Construction Procedures and Design Methods – Brown et al. (2018) about torsion and/or torsional resistance. Aguilar et al. (2018) studied the torsional resistance of drilled shaft foundations, highlighting the lack of standardized design procedures for torsional loading.

1.3. Motivation and Goals

The literature emphasizes the shortcomings in current design methodologies and the need for integrated experimental and computational modeling to enhance the understanding of lateral-torsional interactions. While numerical modeling and small-scale testing provide valuable insights, they cannot fully replace full-scale experimental data. Many studies rely on finite element models, p-y curves, and empirical formulations, but the accuracy of these approaches remains uncertain without full-scale experimental validation. Besides, torsional behavior is not fully captured in small-scale experiments or centrifuge tests considering that the soil particles cannot be scaled in the same way as the structural elements.

In general, the literature underscores the urgent need for large-scale validation efforts to enhance the reliability of design codes and engineering practices, particularly in the context of extreme wind events and the coupled lateral and torsional effects in drilled shafts (Aguilar et al. 2018; Brown et al. 2018; Chung et al. 2017; McVay et al. 2014). Researchers suggest that large-scale tests should be conducted under realistic loading conditions, including combined lateral and torsional loads, to refine current design guidelines (Chung et al., 2017; McVay et al., 2014).

This research aims to address some of these gaps by studying the combined lateral and torsional effects in drilled shafts supporting mast arm structures subjected to extreme wind loads. The study will involve conducting full-scale load tests on drilled shafts under torsional and combined lateral-torsional loads, along with numerical modeling of soil-structure interaction using the software FB-MultiPier. The results will improve the understanding of soil-structure interaction and how combined lateral-torsional forces influence the behavior of drilled shafts, potentially leading to more optimized foundation designs.

The design methods of coupled lateral-torsional drilled shafts under extreme loads (such as high wind) often oversimplify the effects of soil-structure interaction. Conventional foundation analysis methods typically address lateral and torsional loading separately. Research conducted by the University of North Carolina Charlotte has examined foundation practices for coastal mast arm structures across various States. This study highlights the need for further research to gain deeper insights into the performance of drilled shafts subjected to simultaneous lateral and torsional loads. (Rodriguez et al. 2020).

In Florida, experimental studies have evaluated the behavior of drilled shaft foundations subjected to simultaneous lateral and torsional loads. Results from centrifuge tests showed that lateral loading at different points along the mast arm increases the torque on the foundation, suggesting that traditional design methods may neglect these interactions (Hu, 2003; Hu et al., 2006). The University of Florida also conducted full-scale load tests on drilled shafts that support mast arms during significant wind-load events (McVay et al., 2014; Thiyyakkandi et al., 2016). The studies indicated notable decreases in lateral resistance when torque is applied simultaneously and emphasized the need for a unified analysis that accounts for the combined effects of these forces.

1.4. Research Objectives

This study aims to quantify and analyze the coupled response of drilled shaft foundations supporting mast arm structures under simultaneous lateral and torsional loading. It expands on earlier studies from Florida, North Carolina, and the Auburn Highway Research Center by integrating full-scale experimental tests with computational models. The goal is to improve understanding of soil–structure interaction under complex loading conditions. The specific objectives are to:

1. Evaluate the coupled behavior of lateral and torsional forces acting simultaneously on drilled shaft foundations.
2. Design and execute seven full-scale tests on two drilled shaft foundations, including tests under pure torsional loading, combined lateral-torsional loading, and lateral loading.
3. Develop and best-fit estimate numerical models using FB-MultiPier to simulate the full-scale tests.
4. Identify the principal factors influencing the coupled lateral-torsional behavior of drilled shafts and evaluate trends that may support the future development of design-oriented correlations and reduction factors for practical applications.

CHAPTER 2. Literature Review

2.1. Studies of Mast Arm Structures

Several studies have been conducted to analyze the impact of wind on mast arms, focusing on fatigue resistance, structural behavior, and design improvements to mitigate wind-related failures. Chung et al. (2017) established design criteria aimed at enhancing fatigue resistance for cantilevered mast arm structures utilized in traffic signal systems, focusing particularly on wind-induced vibrations and the cumulative effects of structural fatigue. Their research presented a comprehensive set of design guidelines to strengthen structural integrity against repetitive wind loading. The results highlighted the critical importance of creating fatigue-resistant designs, especially in areas prone to severe wind conditions, to ensure long-term durability and safety of the mast arm structures.

Building on this research, a comprehensive investigation was conducted by Bridge et al. (2018), supported by the Florida Department of Transportation (FDOT), to examine the effects of wind on mast arms. This analysis included a review of the current FDOT procedures for the design and analysis of mast arm structures, as well as experimental assessments to determine their residual capacity. The findings from both the review and experiments suggested that certain wind-load parameters, such as the Height and Exposure Factor (K_Z) and Drag Coefficient (C_d), might be unnecessarily conservative, particularly for mast arm segments shielded by attachments like signs or signals. Experimental wind tunnel tests confirmed that shielding with attachments reduces wind load; thus, the researchers proposed an incremental drag coefficient (C_{di}) to factor this effect into design calculations. The study advises utilizing these revised wind load parameters for analyzing existing mast arm structures to evaluate whether the modifications permit the addition of more hardware installations.

2.2. Studies of Mast Arm Foundations

Failures in traditional foundation designs, especially in resisting lateral and torsional loads, have prompted extensive research into alternative foundation solutions. The following studies explore various approaches to enhancing mast arm foundations, concentrating on geotechnical considerations, stress distribution, and innovative foundation techniques.

Building on the assessment of foundation performance across different installation methods, Thiyyakkandi et al. (2017) examined the effectiveness of jetted and grouted precast piles as alternative foundation solutions for mast arm structures. The focus was on analyzing the lateral and torsional load resistance of these piles in various soil types, utilizing centrifuge modeling and full-scale load tests. Results showed that jetted piles, which are installed using high-pressure water or air, initially displayed reduced resistance due to soil disruption during installation. Nevertheless, as time passed, soil reconsolidation enhanced load transfer efficiency, positioning jetted piles as a practical option in loose granular soils, where the jetting method can facilitate the installation. In contrast, grouted piles, which utilize cement-based grout to strengthen the pile-soil interaction, exhibited greater initial stiffness and better load-bearing capacity, especially under combined lateral and torsional loads. The study emphasized the importance of incorporating both lateral and torsional loads in foundation designs for mast arms, as the interaction between these load types significantly affects structural stability. While jetted piles present a cost-effective choice for non-critical applications, grouted piles offer improved stability, making them more appropriate for areas prone to high winds or seismic activity, where foundation performance is vital for long-term durability (Thiyyakkandi et al., 2017).

Rodriguez et al. (2020) conducted a state-of-practice – SOP – review on foundation systems used for coastal traffic signal mast arm structures, evaluating design methodologies and wind load considerations across various state Departments of Transportation (DOTs), as shown in **Figure 2-1**. The study found that single drilled shafts are the most widely used type of foundation. Some agencies, such as NCDOT, VDOT, and ALDOT, have previously integrated drilled shafts with wing walls to improve torsional capacity. However, challenges related to constructability, alignment precision, and concrete placement have prompted agencies like ALDOT to phase out this method in favor of simplified foundation designs (Rodriguez et al. 2020). The SOP report also highlights significant variations in wind load factors across different DOTs due to discrepancies in Allowable Stress Design (ASD) vs. Load and Resistance Factor Design (LRFD) methodologies.

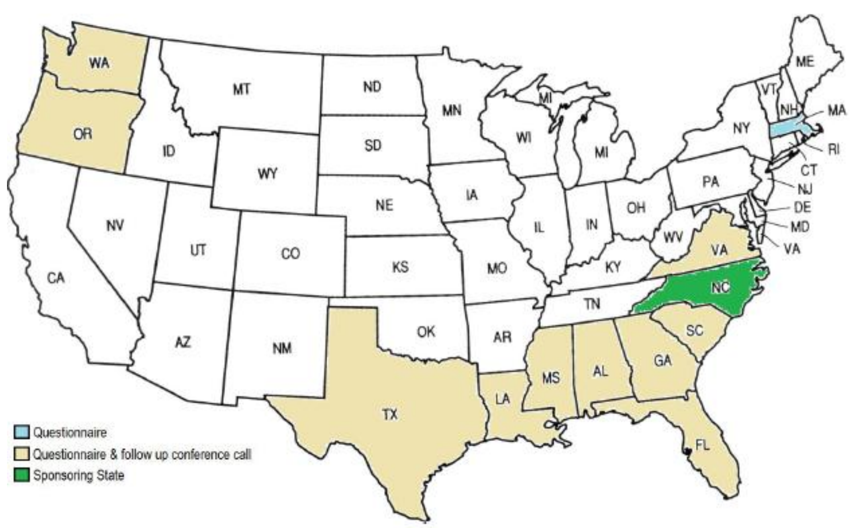

Figure 2-1. Participants of the State of Practice (SOP) Study. (Rodriguez et al., 2020)

None of the 12 DOT States involved in the SOP research accounted for coupled effects. They examined lateral and torsional effects independently, without considering the simultaneous action of lateral, axial, flexural, and torsional loads during extreme events, such as hurricanes. This simplification may lead to an underestimation of the actual demands on foundations.

Using a hypothetical drilled shaft and soil parameters, the study compared the results of the different design approaches used by the NCDOT and the FDOT. This indicated that torsion loading governs the minimum required shaft embedment, as it necessitates a significantly greater embedment depth than that required to resist axial or lateral (bending) loads. Rodriguez et al. (2020) highlights the critical need for design procedures that incorporate the combined effects of lateral and torsional loading, emphasizing the importance of continued research to better understand the performance of drilled shafts under these complex demands. The study also explored alternative foundation systems, such as micropiles, large-diameter driven pipe piles, and finned pipe piles (SPINFIN piles), as potential solutions, particularly in regions characterized by poor soil conditions.

2.3. Studies of Lateral Design of Drilled Shafts

Extensive research has been conducted over the past several decades to understand the behavior of drilled shafts subjected to lateral loading, given their widespread use in bridge foundations, traffic structures, and other critical infrastructure. One of the earliest and most influential contributions was made by Broms (1964a, 1964b), who developed simplified methods for evaluating the lateral resistance of piles in both cohesive and cohesionless soils. His work laid the foundation for many design approaches still in use today. Later, Reese et al. (1974) significantly advanced this field by introducing more refined analyses based on field tests and numerical modeling, which led to the development of the well-known p-y curve method for lateral load analysis. These contributions have been pivotal in enabling engineers to model soil-pile interaction more realistically and to account for nonlinear soil behavior under lateral loads.

Since then, numerous studies have expanded upon these methods, incorporating full-scale lateral load tests and advanced modeling techniques. For instance, Prakash & Sharma (1990) explored the effects of pile flexibility and soil layering, while Matlock (1970) provided a widely used model for soft clays under cyclic lateral loading. More recent efforts, such as those by Rollins et al. (2005), have included full-scale lateral load tests aimed at validating and calibrating analytical models, contributing valuable empirical data to the field. These studies have not only improved the reliability of pile design under lateral loads but also revealed the critical importance of considering soil type, pile geometry, and loading conditions. Overall, the literature provides a robust framework for lateral analysis. Some researchers, (such as Anderson 1997; Eslami and Ebrahimipour 2024) and some agencies as the Federal Highway Administration (Kalavar and Ealy 2000), have compiled lateral load testing results in databases.

2.4. Studies of Torsional Design of Drilled Shafts

Although no standardized design methodology currently exists, several significant studies have attempted to predict the torsional response of foundation elements. Some analytical models used assume idealized conditions and focus on the strength of the shaft material, while others incorporate complex soil-structure interactions.

The analytical and numerical modeling approaches have been developed by using:

- **Boundary element methods** (Basack and Sen 2014; Poulos 1975)
- **Discrete element analyses** (Chow 1985)
- **Nonlinear spring models** (Georgiadis 1987; Georgiadis and Saflekou 1990)– Combined axial and torsional loads.
- **Closed-form analytical solutions** (Randolph 1981; Guo et al. 2007; Guo and Randolph 1996; Hache and Valsangkar 1988; Zhang 2010)
- **Dynamic models** (Cai et al. 2006; Chen et al. 2008; Wang et al. 2008)

Conversely, physical tests have been developed and can be classified into three primary types:

- **Small-scale 1g model tests** on driven piles and drilled shafts (Dutt and O'Neill 1983; Poulos 1975; Randolph 1983; Tawfiq 2000)
- **Centrifuge tests (multi-g loading)** (Bizaliele 1992; Laue and Sonntag 1998;Hu et al. 2006; Hu 2003; Zhang and Kong 2006), where torsional induced shear strains were measured along the test specimens.
- **Full-scale 1g loading tests** (Stoll 1972; Tawfiq 2000; Thiyyakkandi et al. 2016; Li et al. 2017).

Among these studies, torsional load transfer was only directly investigated in one small-scale model test by Dutt and O'Neill (1983).

Aguilar (2018), and Aguilar et al. (2018) developed a statistical comparison of the methods proposed in the literature review for torsional resistance of drilled shaft foundations. The α method (cohesive soils), β method (cohesionless soils), and CDOT (Colorado DOT method) were considered the best fits because they provided the lowest COV and a limited average error in the study. A similar conclusion was reached by Li et al. (2017) and Thiyyakkandi et al. (2016). However, the good agreement between the measured and the predicted torsional capacity values would be a result of compensating errors in the integration along the shaft length; when comparing the unit shear resistance plots, the values differ significantly from the measured ones (Aguilar et al., 2018).

While some public agencies have provided design guidance for the ultimate resistance of torsionally loaded foundations (e.g., Hu 2003), these approaches do not address the rotation (θ) associated with ultimate torsional resistance (Nusairat et al., 2004). The lack of widespread adoption of these methods in state or national codes may stem from the limited availability of experimental torsional load transfer data, particularly from full-scale tests.

2.5. Studies of Combined Lateral and Torsional Loading

The interaction between axial, lateral, and torsional forces plays a crucial role in drilled shaft behavior. McVay et al. (2014) highlighted that torsional stiffness is affected by lateral displacement, requiring comprehensive numerical simulations to model realistic foundation responses. Key findings include the increase of soil confinement and torsional resistance enhancing from the interaction of axial and torsional loads. On the contrary, torsional stiffness decreases as lateral loads increase, which is critical for mast arm structures exposed to high winds (McVay et al. 2014).

The following studies evaluate the performance of drilled shafts under combined lateral and torsional loads. They also examine the effectiveness of jet-grouted piles and post-grouting techniques as viable alternatives in situations where traditional drilled shaft designs may have limitations in torsional capacity and load transfer efficiency.

McVay et al. (2010) investigated the efficiency of grout-tipped drilled shafts and jet-grouted piles, focusing on their group behavior and load transfer characteristics. The study emphasized that while jet-grouted piles behaved as a single block under axial loading, grout-tipped drilled shafts functioned independently with minimal group interaction. Experimental results demonstrated that jet-grouted piles outperformed drilled shafts in both axial and torsional capacities, making them a cost-effective alternative in applications where high torsional demands are present. Additionally, the study highlighted the benefits of staged tip grouting, which significantly increased drilled shaft capacity by preloading the tip resistance and improving skin friction. The findings suggested that current FDOT torsional design methodologies overestimate the resistance of drilled shafts, and recommended revisions to better account for field performance (McVay et al., 2014).

Thiyyakkandi et al. (2016) expanded on these findings by performing comprehensive tests on drilled shaft foundations designed for mast arm structures, assessing how torsion interacts with lateral loading (**Figure 2-2**). The study utilized the mast arm-shaft connection method suggested by Cook and Jenner (2010). Instead of traditional anchor bolts, it featured an embedded pipe reinforced with welded stiffener plates. This alternative connection facilitates a more direct load transfer from the mast arm to the drilled shaft, thereby lowering stress concentrations and mitigating the potential for concrete breakout failures (Thiyyakkandi et al. 2016).

Their results reported a significant reduction in the lateral resistance (of three drilled shafts) due to the influence of torque (**Figure 2-3**), and a reduction of torsional resistance by approximately 20% caused by the impact of lateral load when compared to the predicted resistance using static methods such as α (clay) and β (sand) methods. The variation in lateral resistance reduction with the torque-to-lateral-load ratio was similar across different L/D ratios. This reduction was comparable to that identified by the centrifuge studies of Hu et al. (2006).

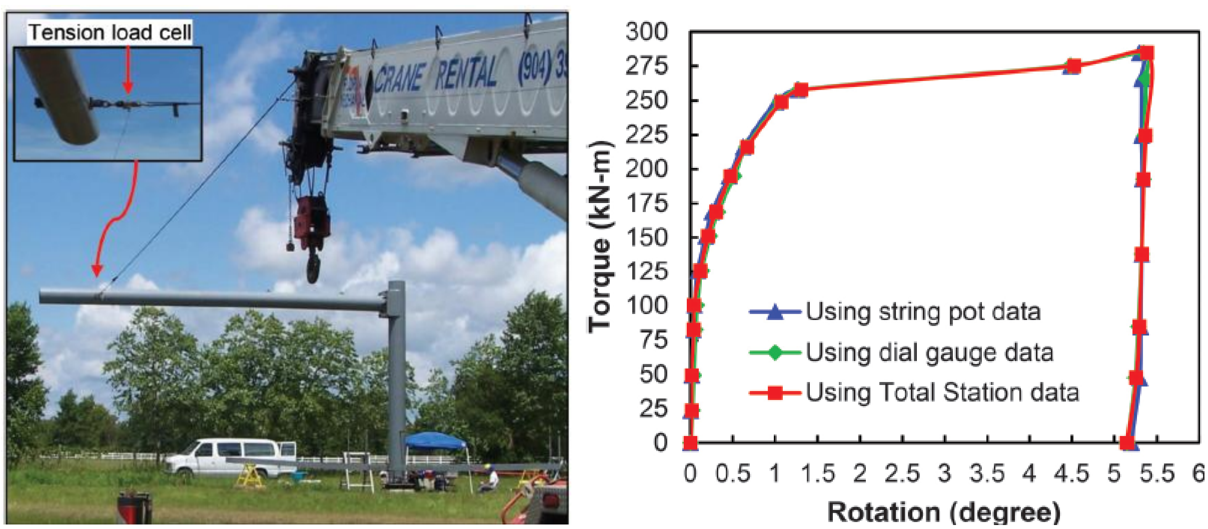

Figure 2-2. Lateral load applied to the mast arm, and rotation measurements (Thiyyakkandi et al. 2016)

Figure 2-4 displays the measured response during the combined load test (blue continued line) and the results when applying a lateral loading on top of the pole (lateral load and moment only, no torque). Based on their findings, the authors emphasized the importance of integrated load analysis in foundation design. Furthermore, the research highlighted that torsional forces were considerable, underscoring the need to include torsional-lateral interactions in FDOT design guidelines for more accurate predictions of foundation performance amid extreme wind events (Thiyyakkandi et al. 2016).

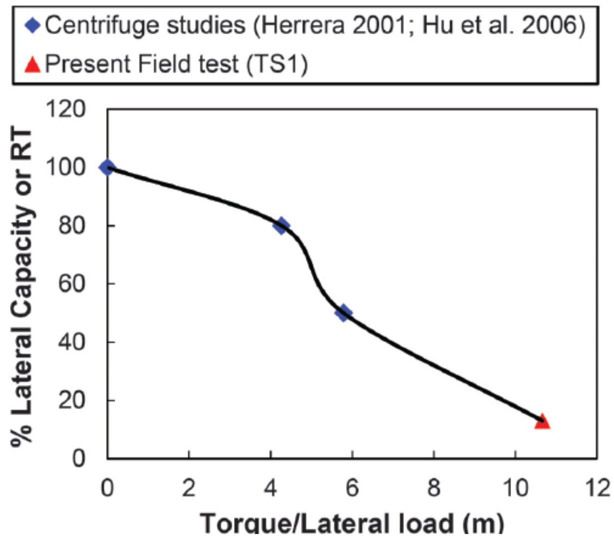

Figure 2-3. Lateral resistance reduction factor due to torsion for ratio L/D = 3. (Thiyyakkandi et al. 2016)

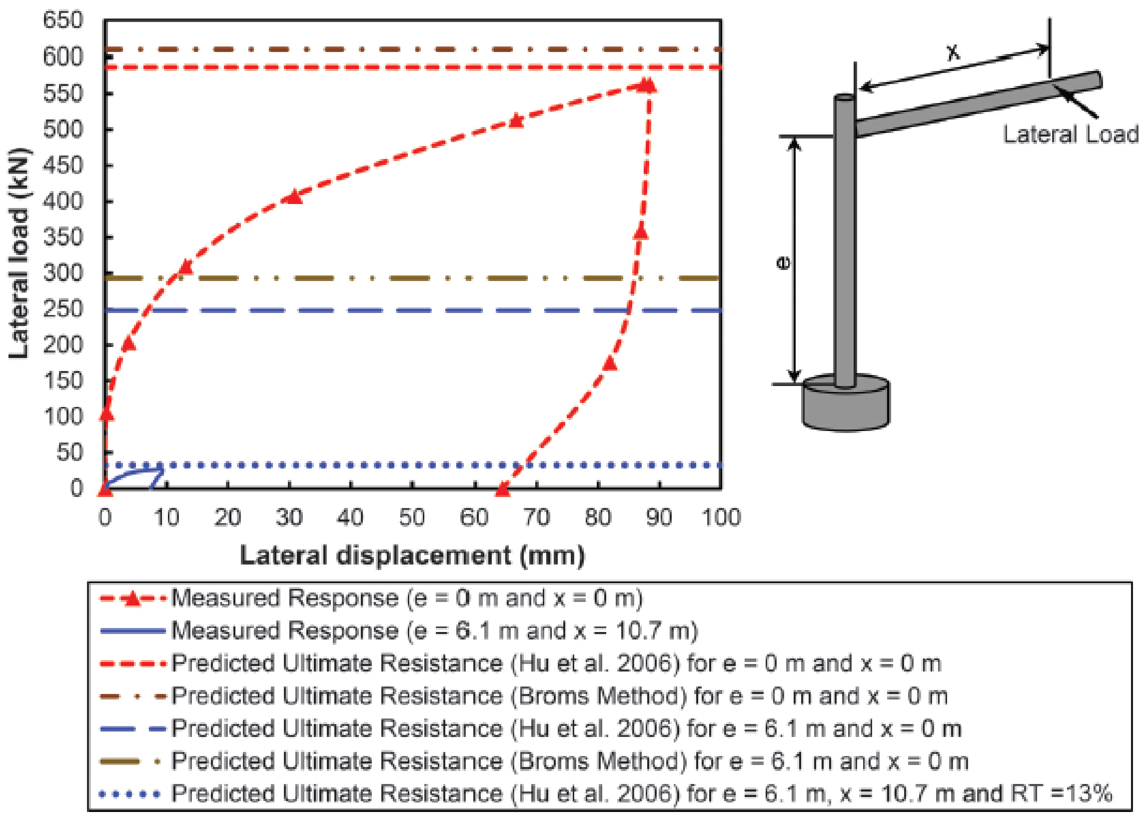

Figure 2-4. Measured and calculated lateral resistance for shaft TS2 of Thiyyakkandi et al. (2016)

Li et al. (2017) investigated the transfer of torsional loads in drilled shafts, with a focus on the distribution of shear stress along the shaft-soil interface. This investigation developed full-scale field experiments to understand the torsional capacity and load transfer. The results revealed that frictional forces at the shaft-soil interface primarily counter torsion, with additional resistance provided by the base at the tip of the shaft. As the torsional load increased, shear stresses accumulated along the shaft, eventually causing soil yielding and a reduction in torsional resistance. Furthermore, the study revealed that cohesive soils exhibited a gradual loss of strength, resulting in larger rotation angles prior to failure, whereas granular soils provided enhanced torsional resistance due to higher interparticle friction. These findings highlight the need for adjustments to the embedment depth of drilled shafts and reinforcement techniques to improve torsional stability (Li et al. 2017).

Huang (2019) further investigated the behavior of drilled shafts under combined lateral and vertical loads, emphasizing their performance during hurricane-level wind events. The study found that larger diameter shafts with greater embedment depths exhibited superior performance, as they distributed stresses more efficiently. Additionally, it recommended incorporating site-specific geotechnical evaluations to optimize foundation designs based on regional soil conditions. The findings underscored the importance of updating design models to account for coupled loading scenarios, particularly in hurricane-prone areas where wind-induced torsional effects are substantial (Huang, 2019).

The studies mentioned above emphasize the critical role of torsional effects in drilled shaft design, highlighting the necessity for enhanced load transfer models and alternative foundation solutions. McVay et al. (2010) and Thiyyakkandi et al. (2016) demonstrated that jet-grouted piles outperform traditional drilled shafts in both axial and torsional capacities, establishing them as a viable alternative for high-torsion applications. Li et al. (2017) and Huang (2019) reinforced the significance of coupled load analysis. Torsion significantly impacts lateral resistance, which is frequently overlooked in standard design methods.

CHAPTER 3. Methodology

This study examines the singular and combined lateral and torsional responses of drilled shaft foundations constructed to support mast arm structures under coupled and individual loads. The methodology used in this research, described in this chapter, integrates numerical modeling and experimental validation to evaluate the impact of soil-structure interaction on foundation performance.

Seven full-scale (1:1) experiments were conducted using two drilled shafts (3 ft diameter) constructed in a controlled geotechnical chamber to evaluate their behavior under lateral and torsional loads. Then, numerical models were developed in FB-MultiPier, and best-fit estimates were made to match the load test results.

The plan of work, phases of the tests, dimensions, and elements incorporated in this experimental research were considered based on the soil properties and preliminary numerical analysis, which will be detailed in the present chapter.

3.1. Soil Characterization

The foundation material within the Geotechnical Chamber is M&M sand. A series of laboratory (sieve analyses, direct shear, and triaxial tests) and in-situ tests (sand cone tests, SPT - Standard Penetration Tests, CPT - Cone Penetration Tests, and DMT - Marchetti Dilatometer Tests) were conducted.

The sieve analyses were conducted in accordance with ASTM C136/C136M-19 and indicated that the sand was poorly graded, with less than 1% fines, and a coefficient of uniformity of 4. As shown in the grain size distribution curves (**Figure 3-1**), the compacted sand used in the geo-chamber closely resembles the material tested by

Okafor (2024). Due to the close similarity in their gradation characteristics, the soil parameter values reported by Okafor (2024) were used in this study.

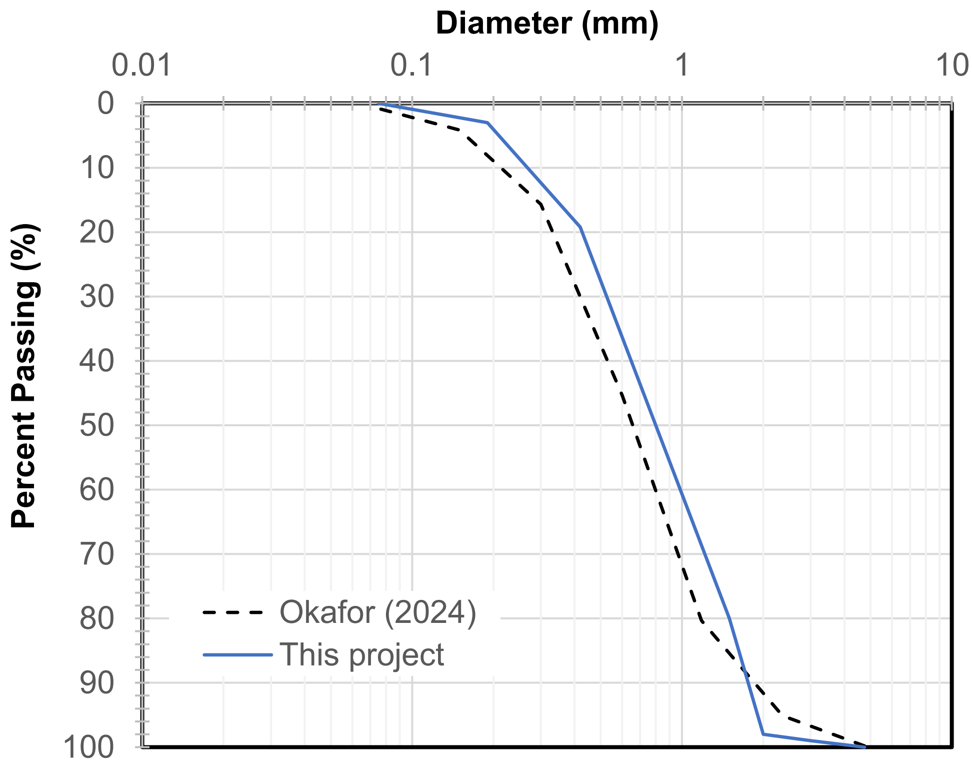

Figure 3-1. Grain size distribution

Laboratory tests performed by Okafor (2024), including direct shear and consolidated drained triaxial tests, yielded internal friction angles of 41° and 41.5°, respectively, and Young's modulus of approximately 5.2 ksi. During initial compaction, sand cone tests in accordance with the ASTM D1556 standard confirmed a compaction ratio near 100% and an average void ratio of 0.46. **Figure 3-2** shows a profile view and dimensions of the geotechnical chamber and drilled shaft used in this project, along with soil properties from Okafor (2024).

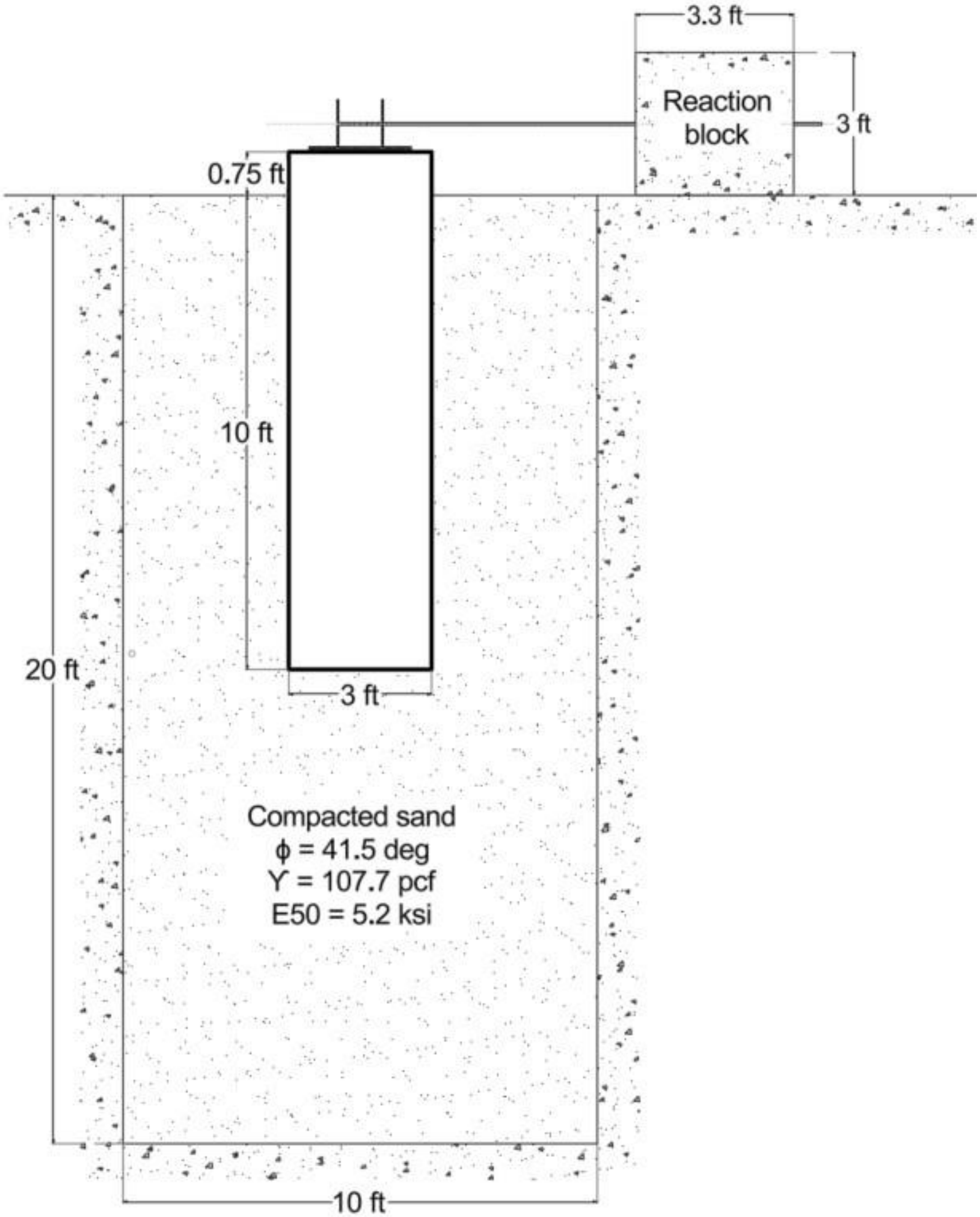

Figure 3-2 Geo-chamber, shaft, and soil profile parameters from Okafor (2024).

The in-situ tests were conducted in the geo-chamber following the completion of the initial compaction process and before the installation of the Phase I drilled shafts. Testing was performed using a CME 550X drill rig provided by ALDOT (**Figure 3-3**), which has a pulldown capacity of 18,650 lb.

Figure 3-3. Drill rig used for the in-situ tests at the geotechnical chamber

To maximize penetration depth, the drill rig was anchored to the laboratory strong floor using chains, as illustrated in **Figure 3-3**. Nevertheless, the high relative density of the compacted sand significantly increased penetration resistance, limiting the advancement of the in-situ testing equipment. Consequently, DMT and SPT soundings were terminated at approximately 6 ft to avoid damage to the testing instruments. Although penetration depth was restricted, the data obtained were internally consistent and showed good agreement among the different testing methods, supporting their reliability for subsurface characterization. The results of CPT and SPT tests are represented in **Figure 3-4**.

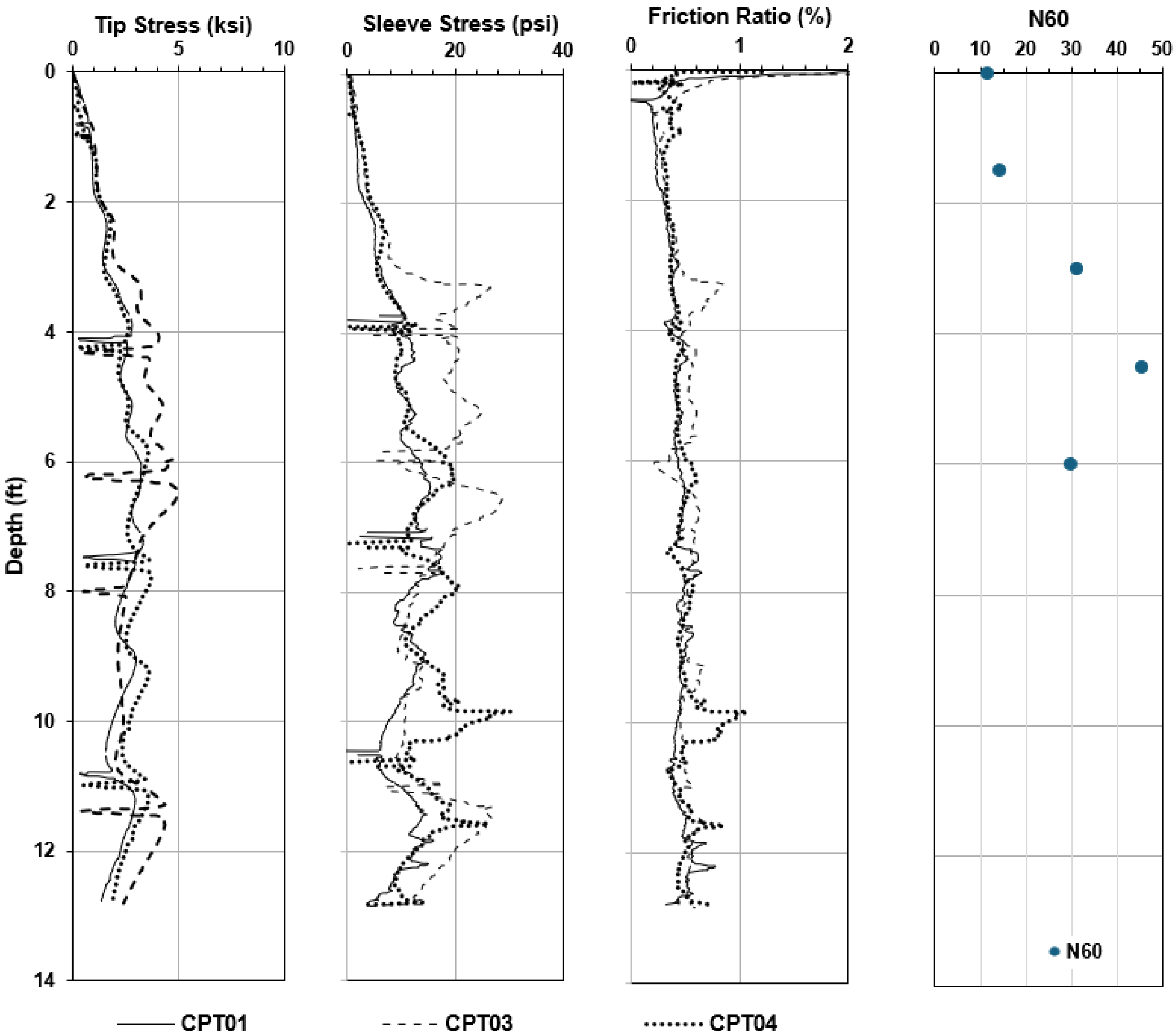

Figure 3-4. Results of CPT and SPT tests

Figure 3-5 presents some of the estimated parameters from the CPT and DMT tests. Both CPT and DMT results indicated a peak internal friction angle of approximately 45°, which is consistent with the expected behavior of a well-compacted, poorly graded sand with minimal fines contentSoil parameters were estimated using the interpretation software CPeT-IT, developed by Gregg Drilling & Testing Inc. and Professor Peter Robertson. The correlations used by the software are defined in the

Users' Manual v3.0, published online by GeoLogismiki (2022). The average estimated values corresponding with **Figure 3-5** are summarized in **Table 3-1**.

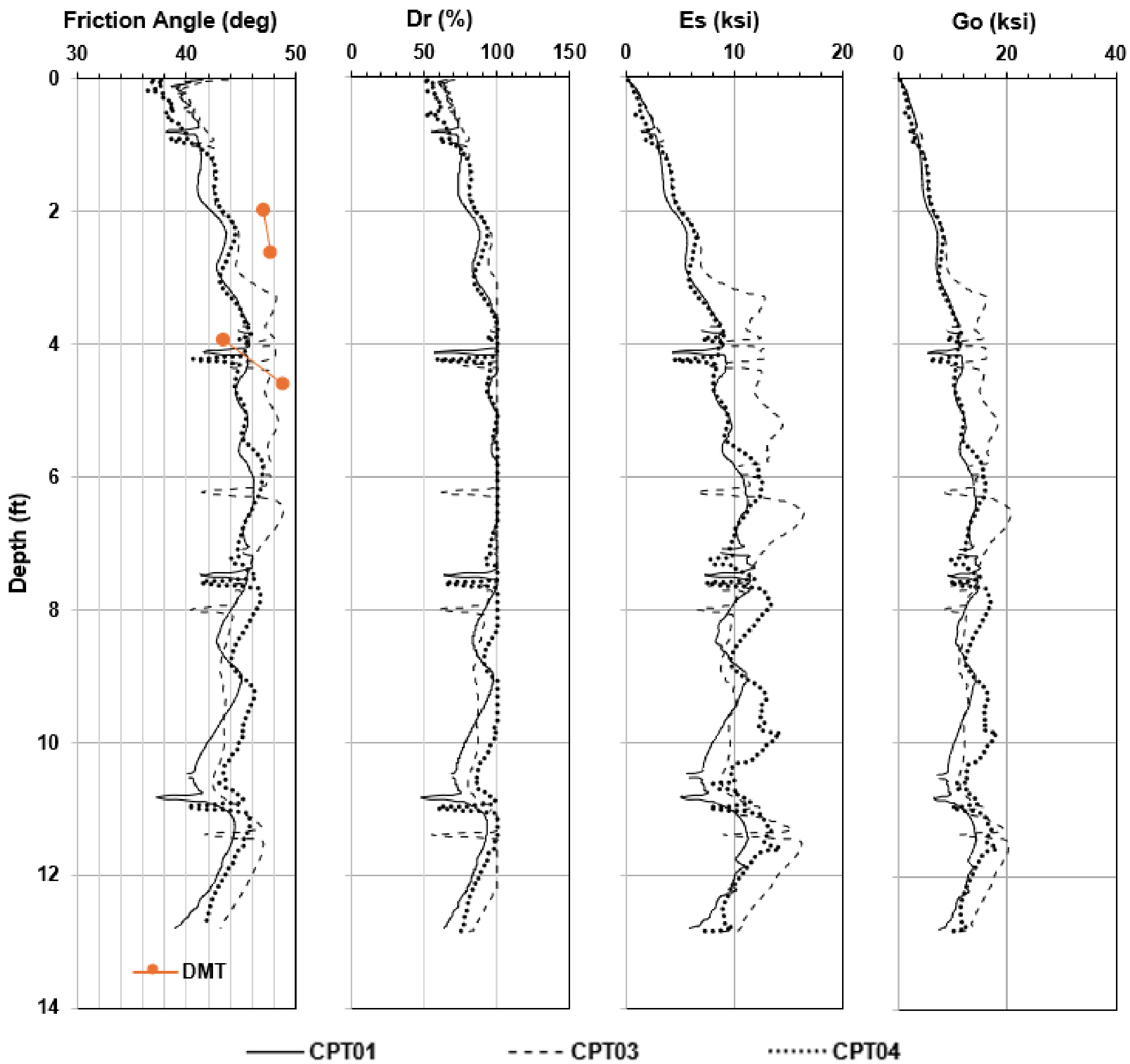

Figure 3-5. Estimated results of the CPT and DMT tests

Table 3-1. Parameters estimated from CPT test using CPeT-IT software

	Estimated Soil Parameters from CPT Test				
CPT	**Friction angle (deg)**	**M (ksi)**	**Dr (%)**	**Es (ksi)**	**Go (ksi)**
CPT01	43.4	10.0	86.7	8.0	10.2
CPT03	44.9	12.3	91.1	9.8	12.5
CPT04	44.1	11.1	90.4	8.9	11.3
Avg	44.1	11.1	89.4	8.9	11.3

3.2. Small-Scale Physical Models

The impact of the shaft construction method – either cast-in-place or precast – on the side resistance of the shaft was assessed through the testing of several small-scale specimens. The goal was to detect any performance differences related to each technique. According to this plan, two cast-in-place (**Figure 3-6**a) and two precast shafts (**Figure 3-6**c), each measuring 6 inches in. diameter and 20 in. in length, were built and tested within a scaled geotechnical chamber made from a wooden box. However, it is important to note that the precast shafts were not driven into the soil (as the real construction process); instead, they were installed in the box before positioning the soil, and then, the sand was compacted around it. **Figure 3-7** shows the setup of the loading system used for the small-scale tests. The torque arm length was 8.5 inches.

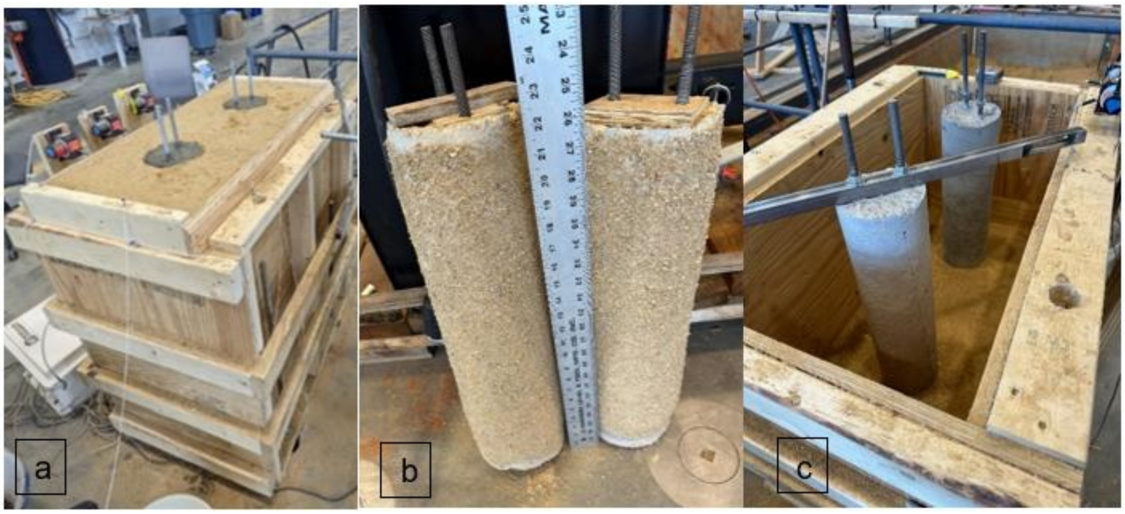

Figure 3-6. a) cast-in or in-situ specimen setup, b) exhumed cast-in specimens, and c) precast specimens test set-up

Observations from the tests revealed that displacements at POT 2 consistently exceeded those recorded at POT 1 (see **Figure 3-7**). This behavior indicates that the system was not loaded purely in torsion under the application of a single lateral eccentric force. Instead, lateral and bending effects were also mobilized and should be considered when evaluating this load case.

The average ultimate load capacities from the small-scale tests were 295 lbs for the cast-in-place (in-situ) specimens and 200 lbs for the precast specimens. The results show that cast-in-place shafts consistently had higher ultimate capacities than their precast counterparts (**Figure 3-8**). This is expected, as all specimens were embedded in compacted sand with a high internal friction angle (41° based on triaxial tests). The rough texture of the cast-in-place (**Figure 3-6**c) shafts enhanced soil–structure interaction, whereas the smoother surfaces of the precast elements resulted in reduced friction and lower load capacity.

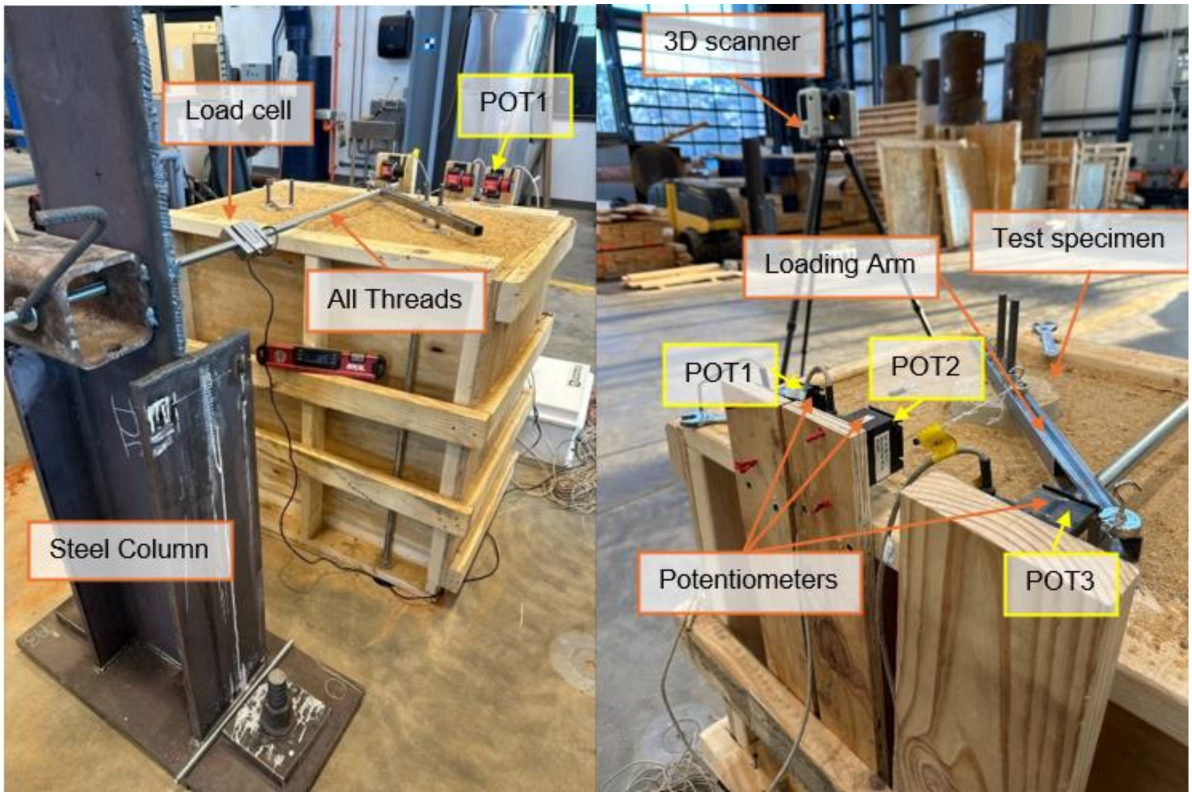

Figure 3-7. Small-Scale Test Configuration

Figure 3-8 also emphasizes the difference in shaft rotation at the point of yielding between cast-in-place and precast specimens. Cast-in-place shafts demonstrated a significantly higher rotational capacity, yielding at approximately 7 degrees of rotation. Conversely, precast specimens yielded at a much lower rotation of around 1.1 degrees. This indicates that cast-in-place shafts can bear higher ultimate loads and exhibit greater ductility when subjected to eccentric loadings.

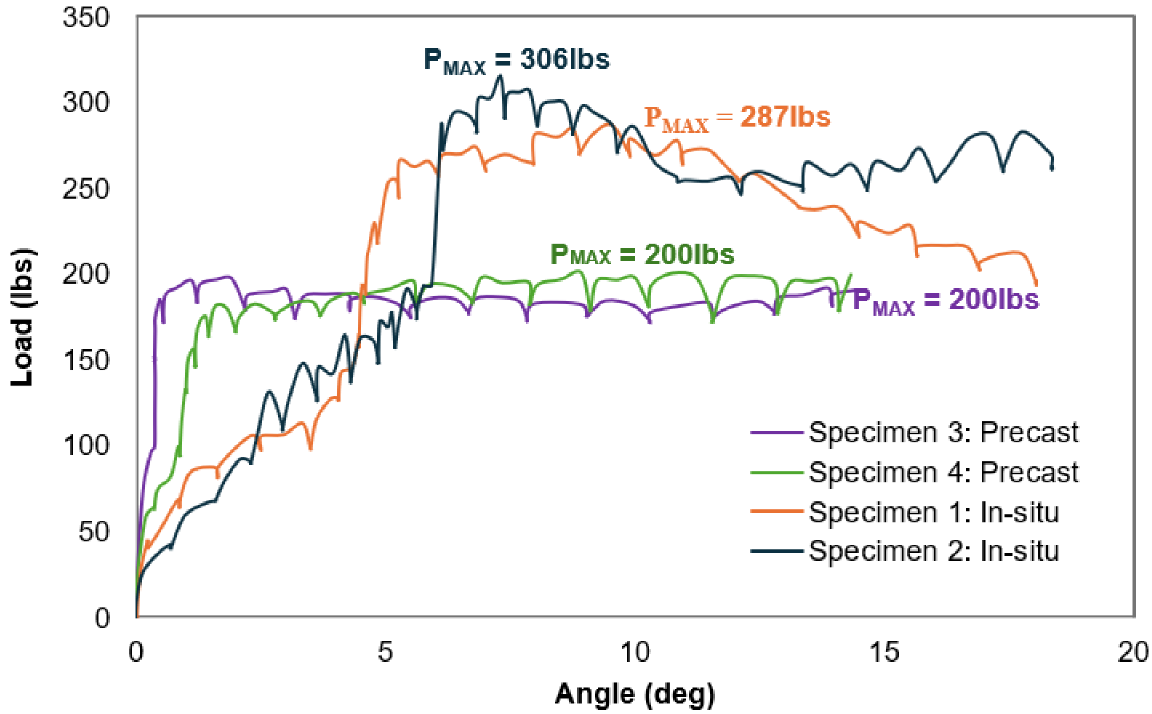

Figure 3-8. Small-Scale test results (Load vs. Rotation).

The shear strength mobilized along the shaft–soil interface at failure, assuming a uniform distribution of shear stress, is defined by the following expression:

$$\tau \frac{T_{ult}}{2\pi r L_{max}} \tag{15}$$

where:

T_{ult} = Ultimate torque (torque at failure)

r, L = radius and embedded length of the shaft

Using the small-scale test results, the calculated average interface shear strength was approximately 321 psf for the cast-in-place (in-situ) specimens and 216 psf for the precast specimens. This represents a reduction of approximately 30% in the interface shear strength for the precast shafts compared to the cast-in-place ones, highlighting the influence of the construction method on soil–structure interaction performance.

3.3. Preliminary Modeling

Numerical modeling serves as an effective method for capturing the nonlinear responses of both the soil and the foundation across various loading scenarios. In contrast to conventional analytical techniques, which often rely on oversimplified assumptions, numerical modeling provides a more comprehensive representation of soil behavior, material properties, and load transfer mechanisms.

3.3.1. FB-MultiPier – Florida Bridge Software Institute

FB-MultiPier (FBMP) is a hybrid modeling software that combines finite element methods for structural components with nonlinear springs to simulate soil behavior. Rather than relying on a full 3D continuum, it adopts a nonlinear Beam-on-Winkler Foundation (BWF) approach to analyze piles subjected to lateral loads (**Figure 3-9**). Originally developed for bridge foundation analysis, FBMP offers a specialized and efficient platform for modeling soil-structure interaction.

In FBMP, the drilled shaft is discretized using beam elements, while the surrounding soil is represented through nonlinear springs assigned at user-defined nodes. This modeling approach provides a practical balance between computational simplicity and the ability to capture essential soil nonlinearities.

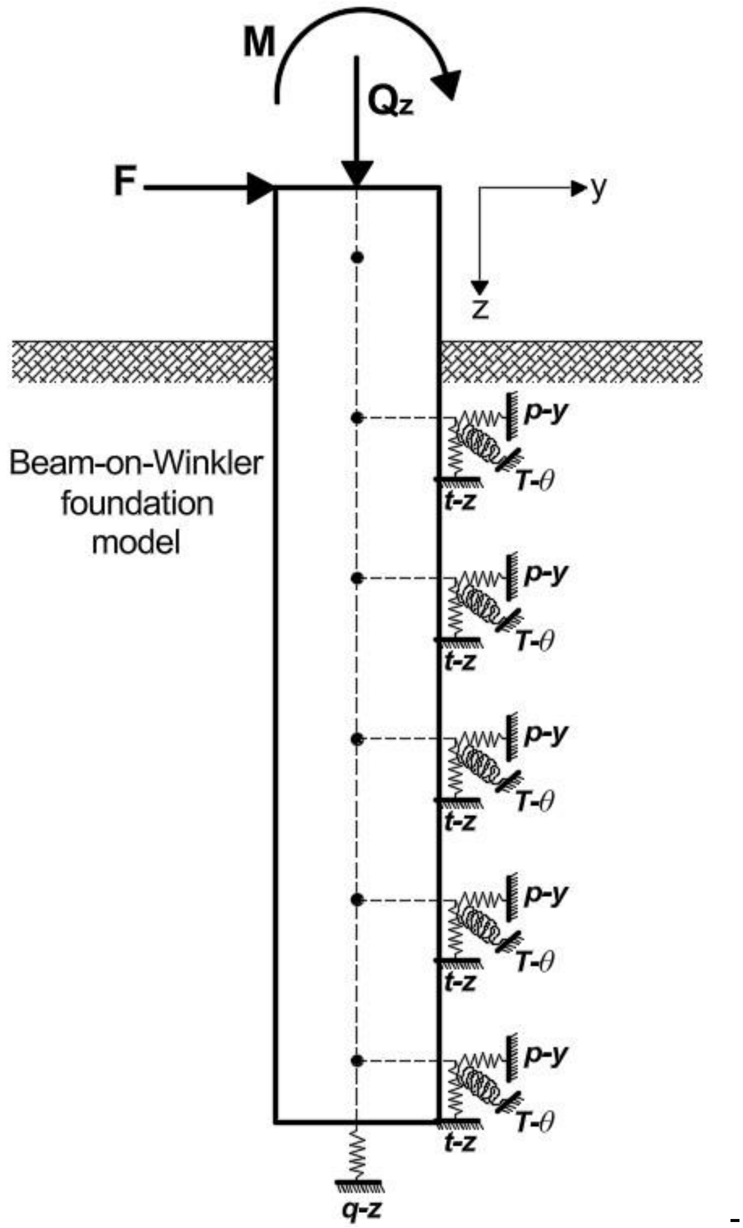

Figure 3-9. Representation of a Beam-on-Winkler foundation model similar to the one used by FBMP.

3.3.2. Nonlinear Behavior of Structural Materials

The internal demands of the concrete members (pile/shaft) in nonlinear analysis in FBMP are dependent on the compressive strength (f_c') and Young's modulus (E_c). As represented in **Figure 3-10**, the tensile portion of the curve is assumed linear up to a stress of f_r, and the compression portion of the curve is nonlinear and defined by the modified Hognestad parabola.

The stress-strain of steel reinforcement is assumed to be elastic-plastic and similar for tension and compression. As well as the concrete, the yield stress f_y and the modulus of elasticity E_s are the input parameters.

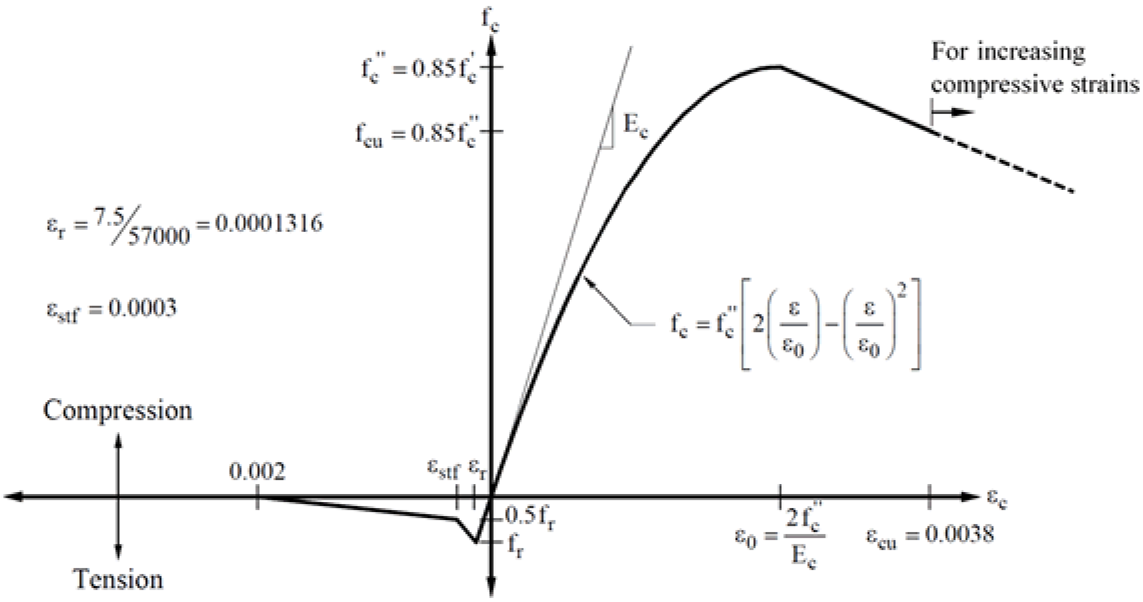

Figure 3-10. Default Stress-Strain Curve for Concrete (FBMP 2025)

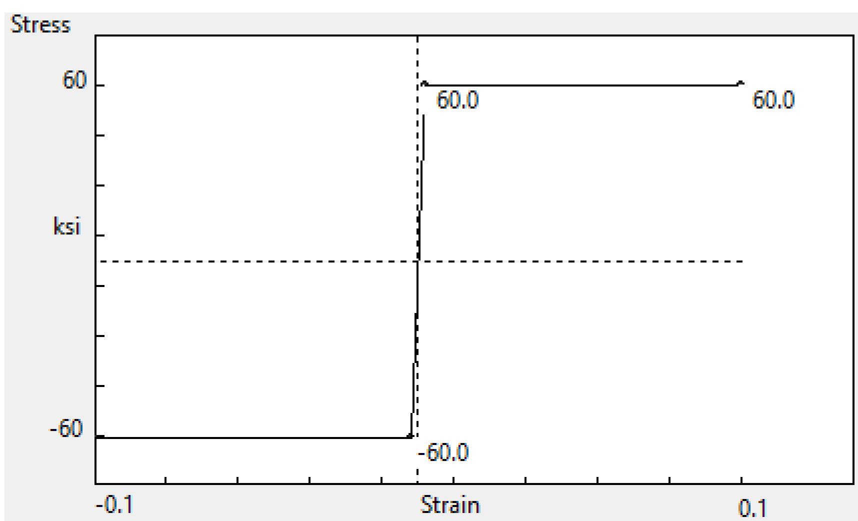

Figure 3-11. Stress-Strain Curve for Mild Steel of f_y = 60 ksi (FBMP 2025)

3.3.3. Nonlinear Behavior of Soils in FBMP

Axial Soil Resistance

The axial soil resistance is composed of friction and tip resistance. FBMP presents several options for the Axial t-z and Q-z curves for cohesive and non-cohesive soils and driven or drilled piles/shafts. The models for drilled shafts are based on FHWA guidance for side shear and end bearing. For side friction, the ultimate values are determined by a (clay) and b (sand) that are generally attributed to O'Neill and Reese (1999). In terms of end bearing, a modified Terzaghi equation is used for clay while sand is based on the average N_{60} corrected SPT blowcount in the vicinity of the shaft bottom. Trendlines for load settlement, which are also attributed to Reese and O'Neill (1989) are implemented for t-z and Q-z curves. The end bearing and side friction curves in sand and clay are presented in **Figure 3-12**.

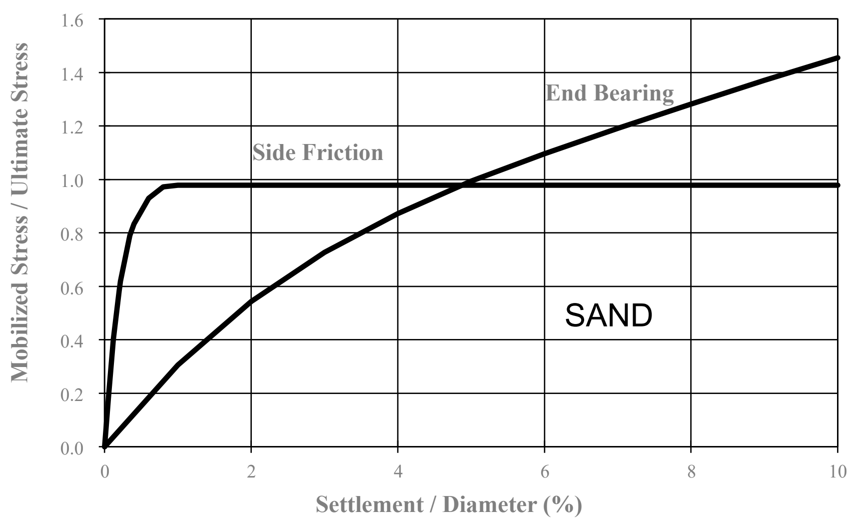

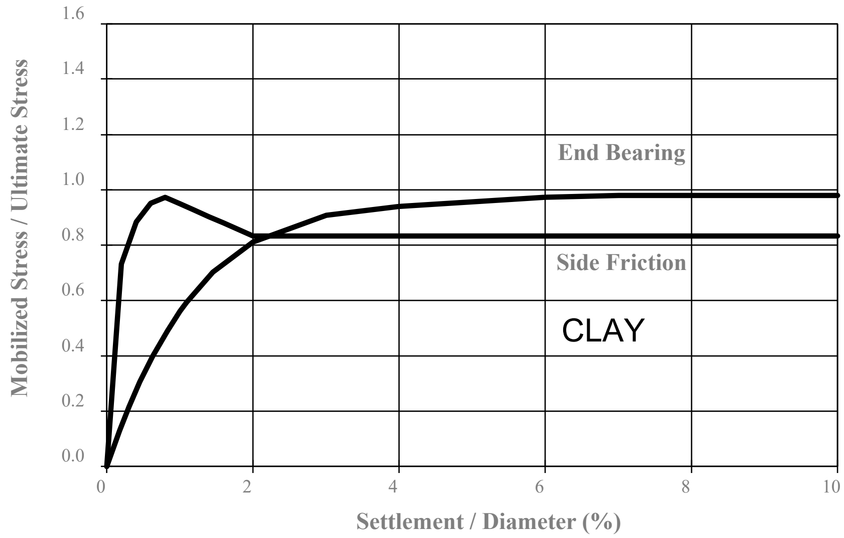

Figure 3-12 t-z and Q-z trendlines for sand and clay based on Reese and O'Neill (1989)

Lateral Soil Resistance

The *p-y* curves model the stiffness and strength of the surrounding soil by representing it as a series of nonlinear springs distributed along the length of the shaft. These curves define the soil resistance per unit length (*p*) as a nonlinear function of lateral deflection (*y*), effectively capturing both the initial stiffness and the ultimate resistance of the soil at different depths.

In FB-MultiPier (FBMP), p-y curves are automatically generated based on input soil properties such as unit weight, internal friction angle, and modulus of subgrade reaction, along with empirical relationships specified by the user. The shaft is discretized into segments, with a unique p-y curve assigned at each depth node, as explained in **Figure 3-9**. This enables FBMP to model a realistic, depth-dependent soil response to lateral loads. **Figure 3-13** presents one of many methods available in FBMP to construct p-y curves.

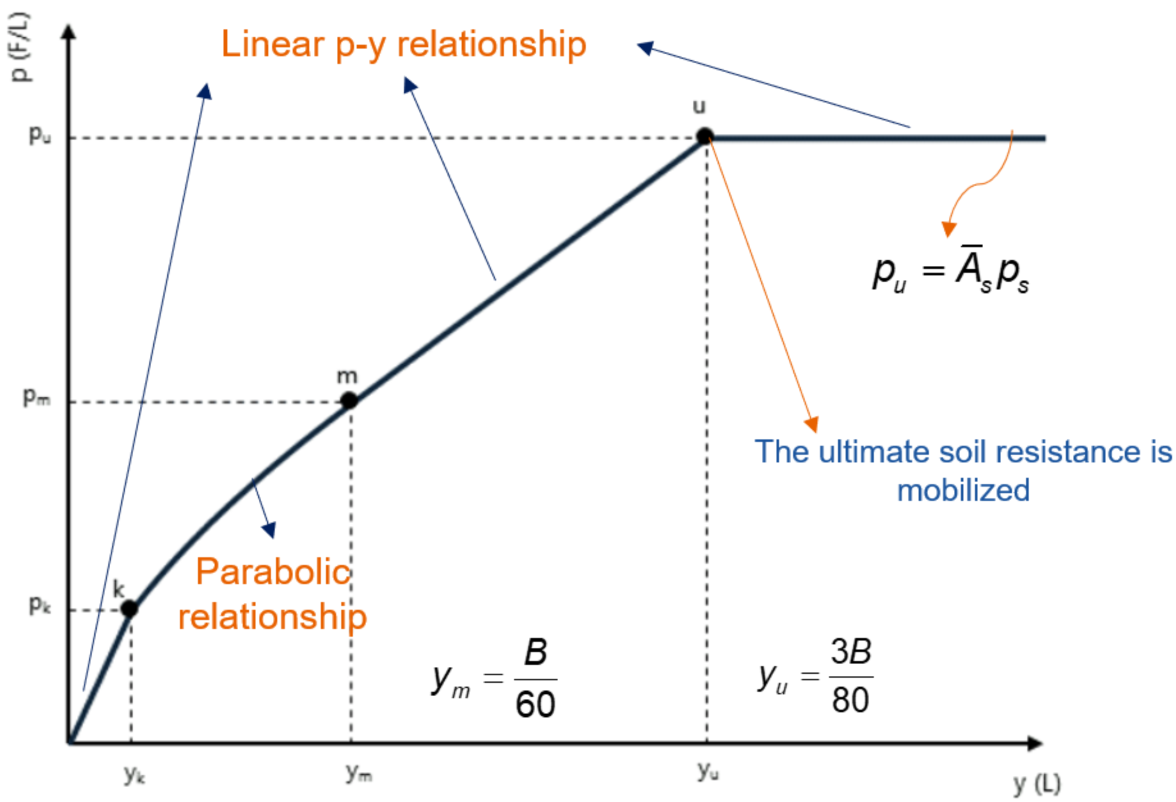

Figure 3-13. Procedure to construct the sand p-y relationship (Reese et al. 1974)

Torsional Soil Resistance

Among the soil interaction models, the torsional resistance model is considered the most undeveloped. It is an implementation of work by Randolph (1981). An ultimate side shear T_{ult}, is used to define the limit of the curve, as shown in **Figure 3-14**. The shear modulus and Poisson's Ratio for the soil are used to define the increase of torsional resistance with rotation.

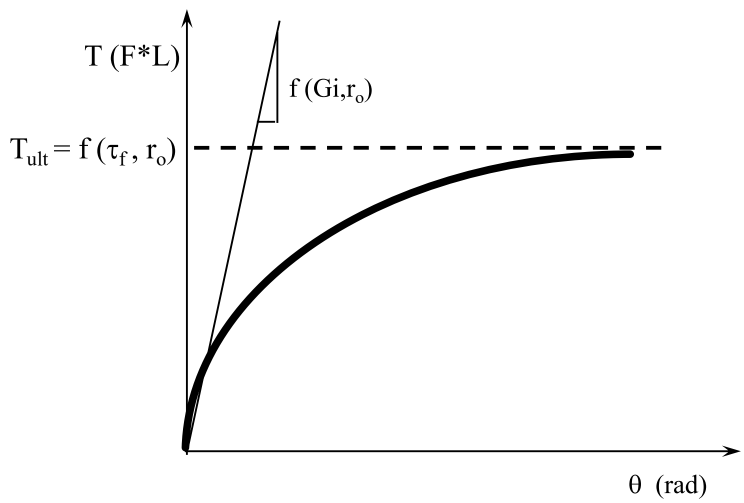

Figure 3-14. Torsional resistance model by Randolph (1981) implemented in FBMP

3.3.4. Preliminary Models of the Research

During the initial analysis and load test planning, nonlinear models were created in FB-MultiPier to assess and improve different options for the full-scale load test setup. **Figure 3-15** illustrates the load test configuration, locating the key points of interest for analysis. In the figure, red nodes denote the H-Pile, which acted as the “arm” where lateral and torsional loads were applied, and yellow nodes indicate the top and bottom of the shaft. The structural input parameters entered into the software are listed in Table 3-2.

Lateral Loading

For this model, the p-y curves presented in **Figure 3-16** reflect the behavior of a well-compacted sand profile, consistent with in-situ test results presented in 3.1. The curves show a nonlinear softening response at shallow depths and a stiffer, more confined response at greater depths – behavior typical of dense sands. These curves form the backbone of the lateral analysis in FBMP and are essential for predicting realistic deflection and moment profiles along the shaft.

Table 3-2. Input concrete and reinforcement parameters.

Shaft/Concrete Properties	
Diameter (in)	36
Embedded length (in)	120
f_c' (ksi)	4.5
E_c (ksi)	3861
υ_c	0.2
γ_c (pcf)	150
Reinforcement/Steel Properties	
F_y (ksi)	60
F_u (ksi)	75
E_r (ksi)	29000
γ_r (pcf)	490
υ_r	0.3
Longitudinal steel	14#8
Transverse steel	#4@6in

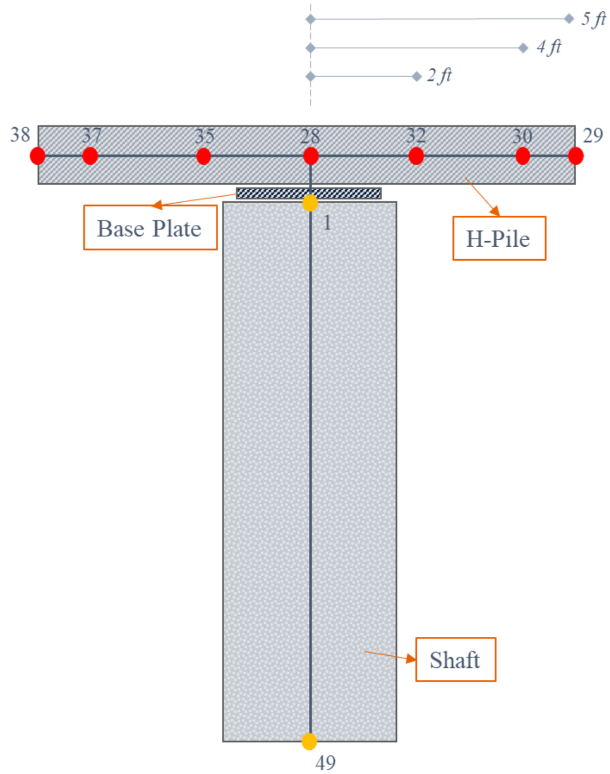

Figure 3-15. Schematic load test configuration (elevation view without soil).

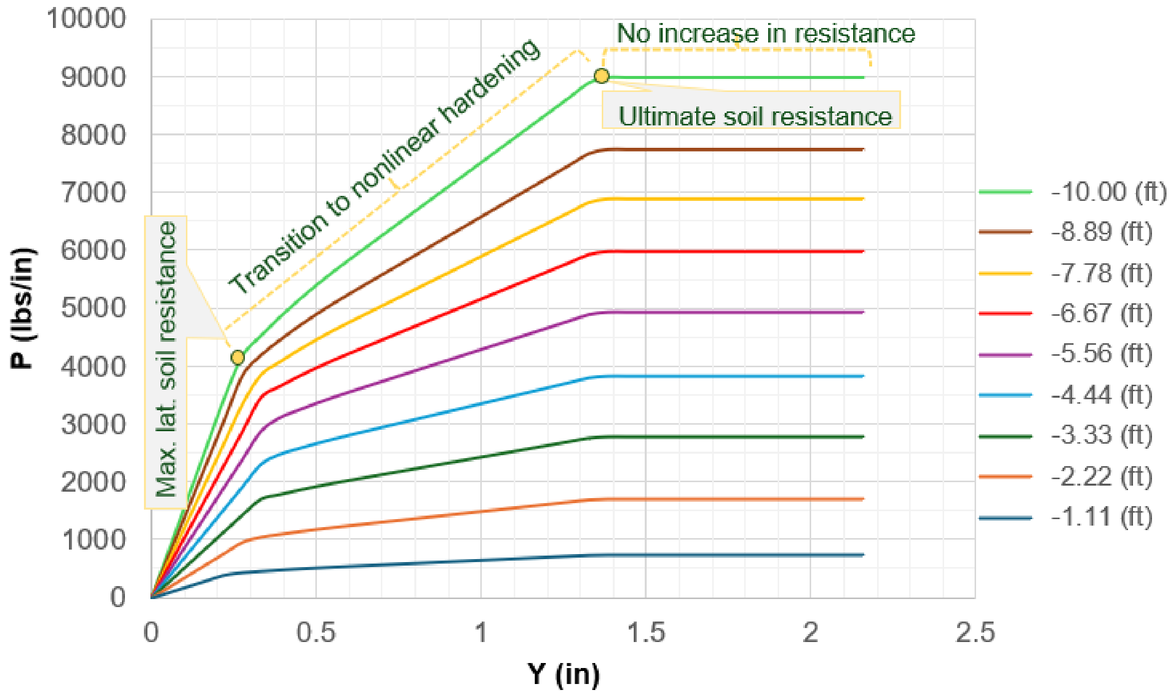

Figure 3-16. P-Y curves generated in FBMP

Single Lateral Load

To evaluate the pure lateral response of the shaft, two scenarios were analyzed. In both cases, a single lateral force was applied along the longitudinal axis of the shaft, but the application point was varied.

Scenario 1: Top of shaft - Node #1 (refer to Figure 3-15)

The maximum load applied, within convergence limits, was 103 kips. The analysis yielded a maximum bending moment of 539 kip-ft, a shear force of 190 kips, and a demand-to-capacity (D/C) ratio (defined as the ratio between the structural demand of the shaft and the available capacity) of 0.77. The D/C ratio reflects how close the shaft is to its structural failure.

Scenario 2: Center of H-Pile - Node #28 (refer to Figure 3-15)

The maximum load reached 97.9 kips, along with a slight increase in the bending moment (555 kip-ft) and shear (194 kips), leading to a marginally higher D/C ratio 0.79.

The comparison between this case and the load applied directly at the shaft top shows slight differences in demand and capacity utilization. However, this setup better simulates the behavior of mast arm structures, where wind loads act on elevated components. In this case scenario, the lateral load has a significant influence on shaft behavior, with demand reaching nearly 80% of the structural capacity, even in the absence of torsion. Based on this analysis, lateral loads in subsequent simulations and tests will be applied at the H-Pile rather than at the shaft top with little or no impact on the results.

Dual Lateral Load

To refine the load test configuration, a dual lateral load setup was analyzed and compared against the single-load case at node #28. Two dual load configurations were considered:

- At nodes **#30 and #37** (arm length: 4 ft)
- At nodes **#29 and #38** (arm length: 5 ft)

In both cases, the system converged at a load of 49 kips per actuator, resulting in maximum internal forces and D/C ratios that were nearly identical to those in the single-load scenario. For practical and constructability reasons, the 4-ft arm configuration (nodes #30 and #37) was selected for the lateral load test. This configuration enables the application of tension-only loads (instead of compression) using hydraulic actuators at both points.

The results of the lateral displacement from the numerical modeling of the dual lateral load at nodes #30 and #37 are presented in **Figure 3-17**. The shaft reached a maximum lateral displacement of 13.4 inches at ground level under the ultimate load in FB-MultiPier. It is important to clarify that this value is unlikely to be observed during the full-scale test; the data shown in this section are derived solely from the numerical model and aim to improve comprehension of the predictive capabilities of the program.

The inflection point (where the lateral displacement equals zero and the direction of bending reverses) was consistently located at a depth of approximately 7.3 feet, as shown in **Figure 3-17**. This behavior is characteristic of a short pile response, where the shaft rotates predominantly as a rigid body, influenced by its limited embedment and overall stiffness.

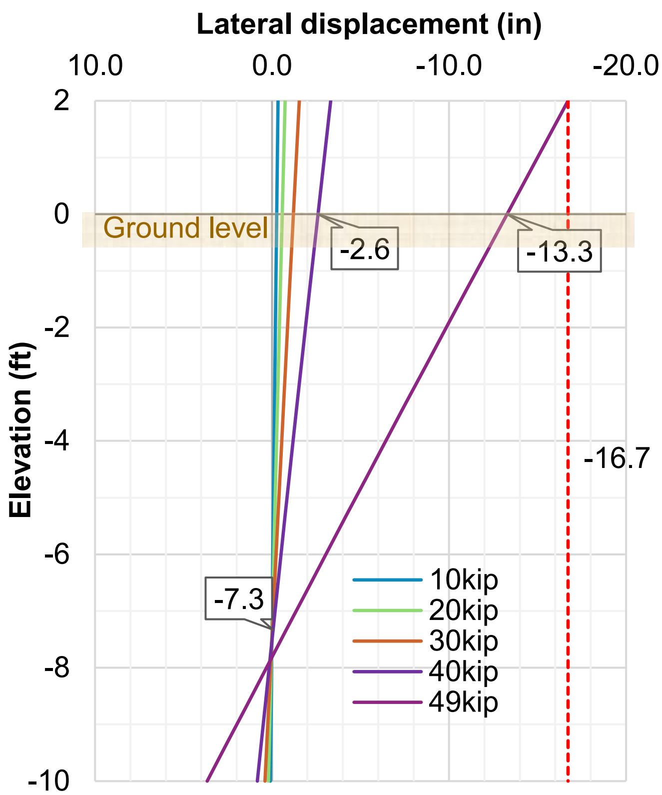

Figure 3-17. Lateral displacement of the shaft due to dual lateral load application.

To better understand the surface soil response, the displacement evolution between the 40-kips and 49-kips loads was investigated by running the model with 2-kips increments within that range. The results indicated a gradual and consistent increase in displacement, with no evidence of sudden failure or abrupt behavioral shifts. However, beyond a load of approximately 44 kips, corresponding to a lateral displacement of about 3.9 inches, the rate of displacement increase became noticeably steeper, suggesting that the soil-structure system was approaching its near-ultimate lateral capacity.

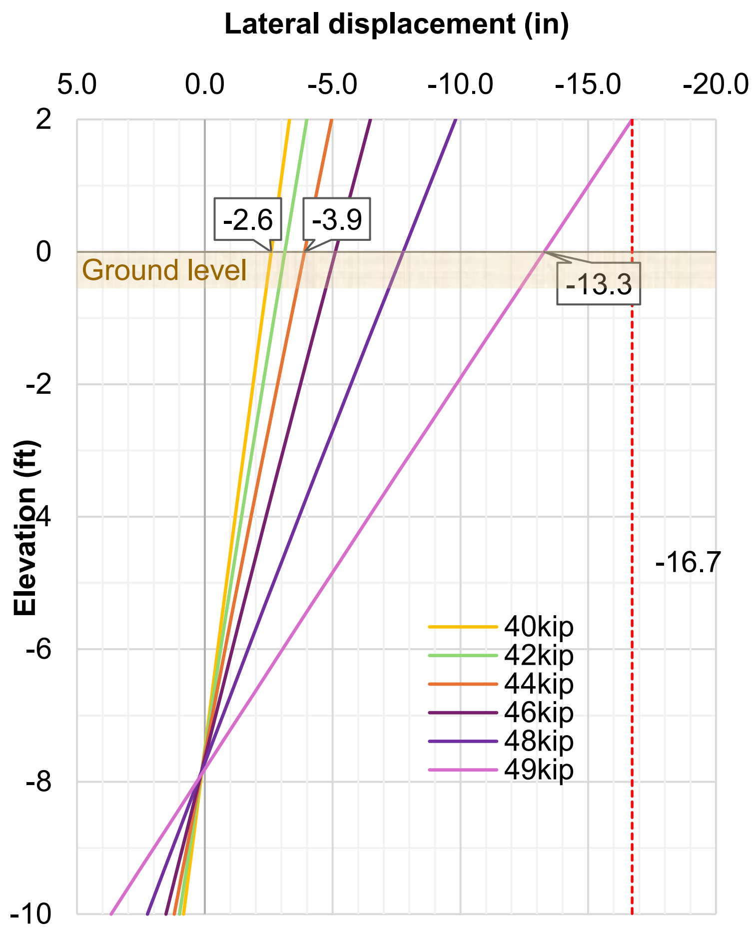

Figure 3-18. Lateral Displacements in the Range of 40 to 49 kips Loads.

Based on the displacement results of **Figure 3-18**, the load-displacement curve at ground level (0.0 ft embedment) was extracted and is shown in **Figure 3-19**. At this level, the soil consists of compacted sand with limited confinement. As expected, the curve displays a typical shallow sand response, characterized by an initial stiff slope followed by nonlinear softening. The peak lateral resistance of 25 lb occurs at a displacement of 0.8 inches, after which the resistance continues increasing gradually. The ultimate resistance of 48 lb is reached approximately at 7.0 inches, beyond which the curve plateaus, indicating that the lateral capacity of the soil has been fully mobilized.

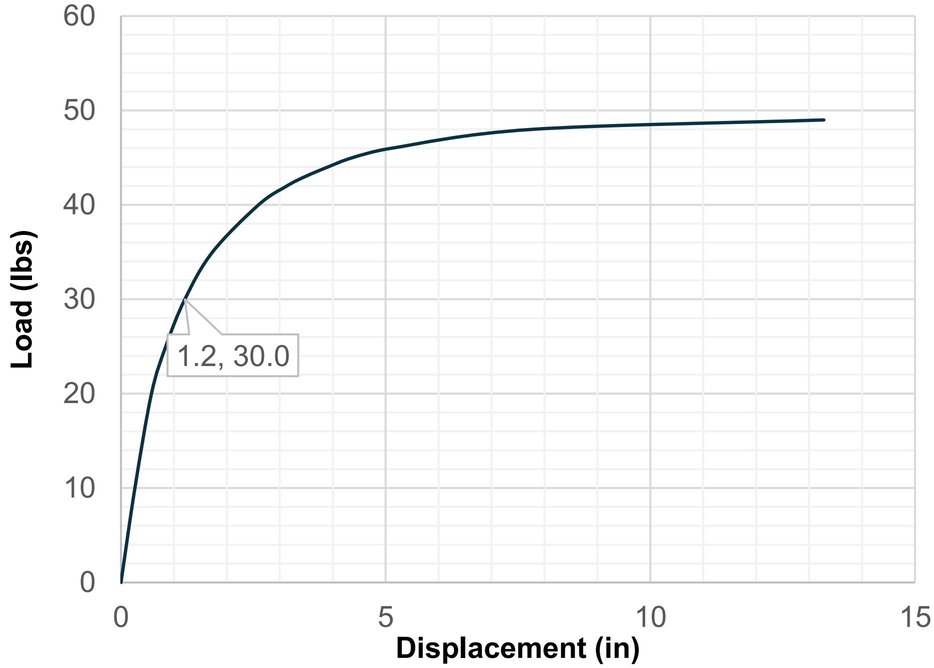

Figure 3-19. Load vs. displacement curve at depth = 0 ft (ground level)

Pure Torsional Loading

A dual-force loading configuration was proposed to induce a controlled and pure torsional response in one of the shafts. To evaluate this approach, an FB-MultiPier model was developed using a pair of equal and opposite lateral forces (dual loads) applied through a 4 ft moment arm, as illustrated in Figure 3-20, to simulate pure torsional loading.

The demand-to-capacity (D/C) ratio remained below 0.01, indicating negligible structural demand on the shaft. This extremely low ratio confirms that the shaft stays well within its structural capacity under torsional loading. Consequently, failure due to torsion is not expected, and the observed behavior is primarily governed by soil-structure interaction rather than structural limitations.

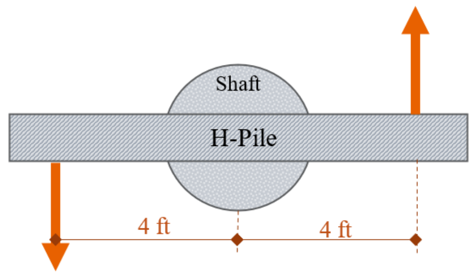

Figure 3-20. Plan view of the dual-force configuration for the model.

The maximum dual loads applied reached 12.7 kips per side, acting through the 4 ft arm, while maintaining FB-MultiPier convergence. Results indicated that torsional resistance in the soil initially concentrated near the top of the shaft under low loading conditions. This suggests that the upper soil portion mobilizes first. As the applied torsional load increased, the resistance became more evenly distributed along the shaft, indicating progressive mobilization of the deeper soil.

Figure 3-21 presents the rotation profiles obtained from FBMP under pure torsional loading. To improve clarity and highlight the large variation in rotation magnitudes, a break in the x-axis was introduced. The maximum rotation of the shaft was 4.95°, with a significant increase observed between the 10 kips load (0.16°) and the ultimate value.

This behavior aligns with the T-θ curve generated by FB-MultiPier (**Figure 3-22**), which governs the relationship between applied torque and rotational deformation. The shape of this curve is dependent on the assigned shear modulus, which defines the torsional stiffness of the system and controls its nonlinear response.

In this model, a shear modulus of 3 ksi was assigned to represent the dense sand. It was calculated based on the Young's modulus (E) and Poisson ratio (υ) of the soil, as defined in Equation 16. The Young's modulus is derived from the triaxial tests reported by Okafor (2024). The shear modulus value used produced a steep initial slope in the T-θ curve before yielding, indicating high initial stiffness under small deformations, followed by progressive softening as the system approached its ultimate capacity.

$$G = \frac{E}{2(1 + \upsilon)} \tag{16}$$

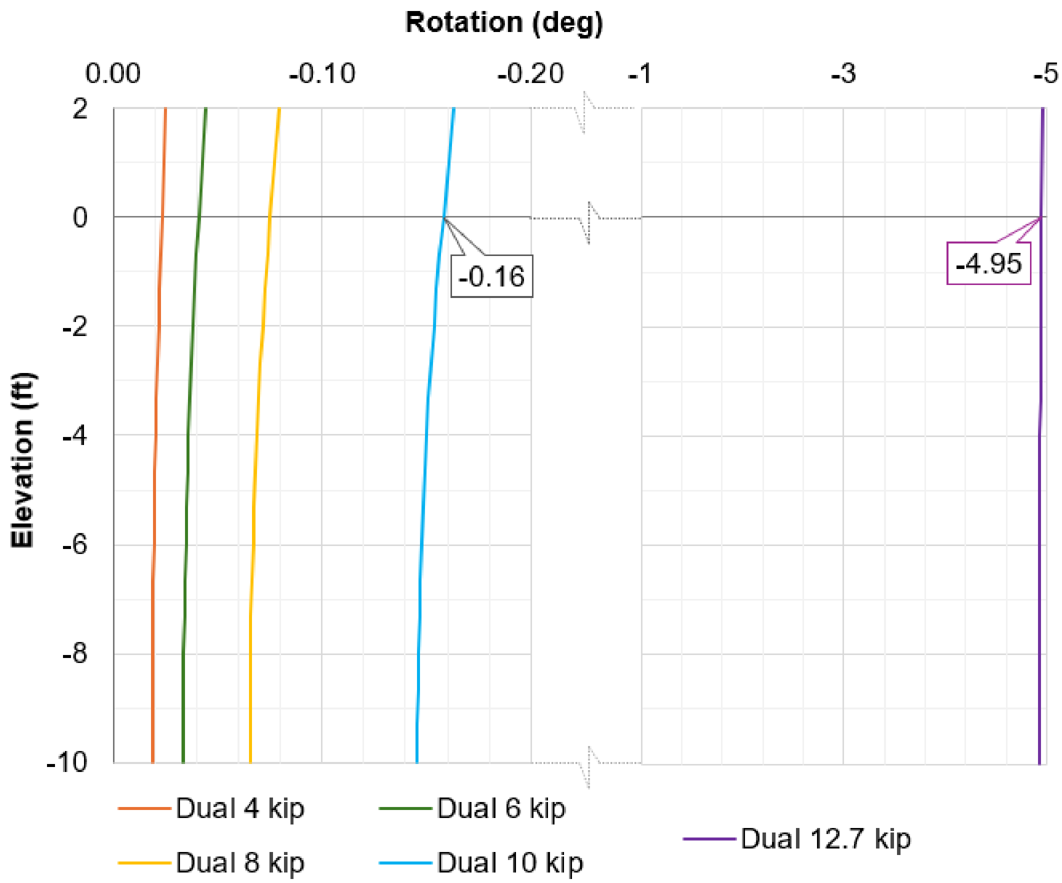

Figure 3-21. Shaft rotation under increasing dual loading and increasing moment

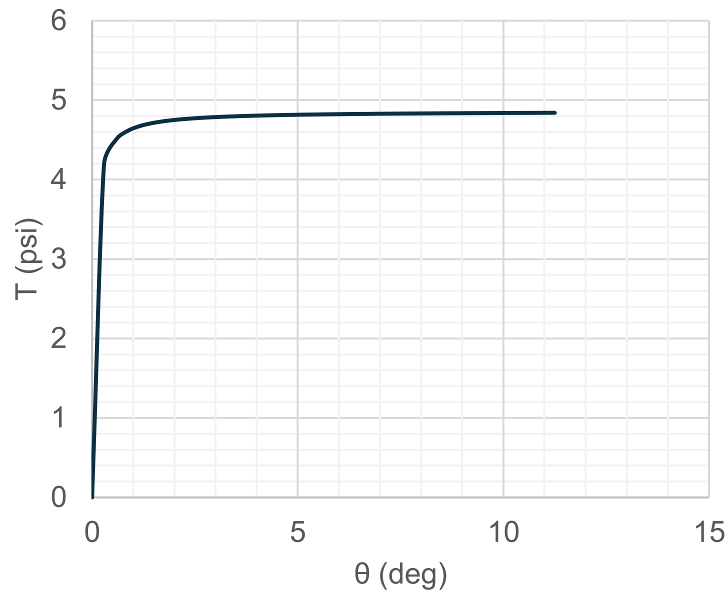

Figure 3-22. T-θ curve defined by FBMP

Combined Load Effects

A single eccentric load applied through a 4 ft arm was also analyzed in FB-MultiPier, reaching a maximum load of 26 kips. Compared to the pure torsional scenario, the demand-to-capacity (D/C) ratio values were noticeably higher, reflecting the additional bending effects induced by the eccentric load. Nonetheless, the values remain low overall (maximum value of 0.17), indicating that the structural capacity of the shaft is not significantly compromised. The maximum rotation at the top of the shaft corresponded to 9.1° as shown in **Figure 3-23**.

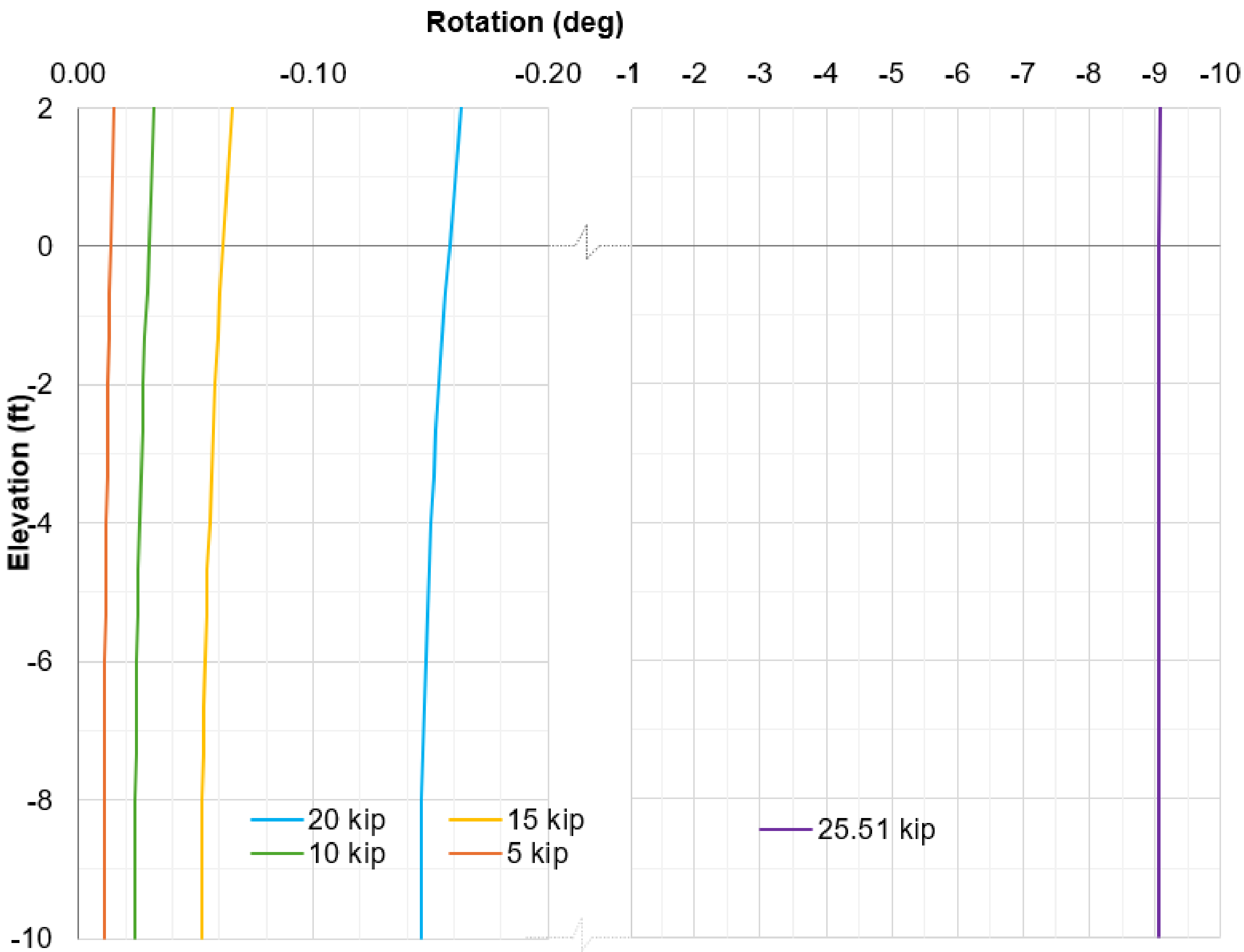

Figure 3-23. Shaft rotation under increasing eccentric loading.

3.4. Load Testing Planning

The full-scale load tests were conducted in the Geotechnical Chamber located within the Advanced Structural Engineering Laboratory (ASEL) at Auburn University (**Figure 3-24**). This state-of-the-art facility provides a controlled environment for evaluating soil-structure interaction under simulated extreme loading conditions, ensuring precise measurements and reproducible results. The Geotechnical Chamber, strong floor, hydraulic actuators, and overhead cranes in this facility enable the testing.

Figure 3-24. Compacted Sand in Geotechnical Chamber.

3.4.1. Structural Design of Elements

Drilled Shafts

The drilled shaft was designed to resist the combined effects of axial, lateral, flexural, shear, and torsional demands expected during the full-scale testing program. A shaft diameter of 36 inches with 3 inches concrete cover, and effective length of 10 ft. was selected as a representative mast arm foundation, and the structural reinforcement layout consisted of fourteen No. 8 longitudinal bars with No. 4 ties spaced at 6 inches c/c. The applied design loads included a factored moment of 105 kip-ft, a lateral shear of 120 kips, an axial load of 4 kips, and a factored torsional demand of 140 kip-ft. Structural capacity calculations were performed in accordance with ACI 318-19 requirements for strength design. Flexural resistance was governed by the compression block depth and reinforcement layout and resulted in a nominal moment capacity of 747 kip-ft, which exceeded the applied demand. Shear resistance, based on the combined contributions of concrete and transverse reinforcement, provided a nominal shear capacity of 150 kips, also exceeding the applied load. Axial capacity was dominated by concrete compression, resulting in a nominal factored axial strength of approximately 2800 kips, far greater than the applied axial load. Torsional resistance was evaluated using ACI 318-19 torsion provisions, with the threshold, cracking, and nominal torsional strengths computed based on the geometric and reinforcement properties of the shaft; the resulting nominal torsional capacity of 183 kip-ft was sufficient compared with the applied torsional demand. Minimum and maximum longitudinal reinforcement limits were satisfied, and transverse reinforcement exceeded the required minimum torsion and shear reinforcement ratios. Overall, the structural design of the shaft met all relevant strength and detailing requirements (Appendix A), ensuring adequate capacity for the combined loading conditions imposed during testing.

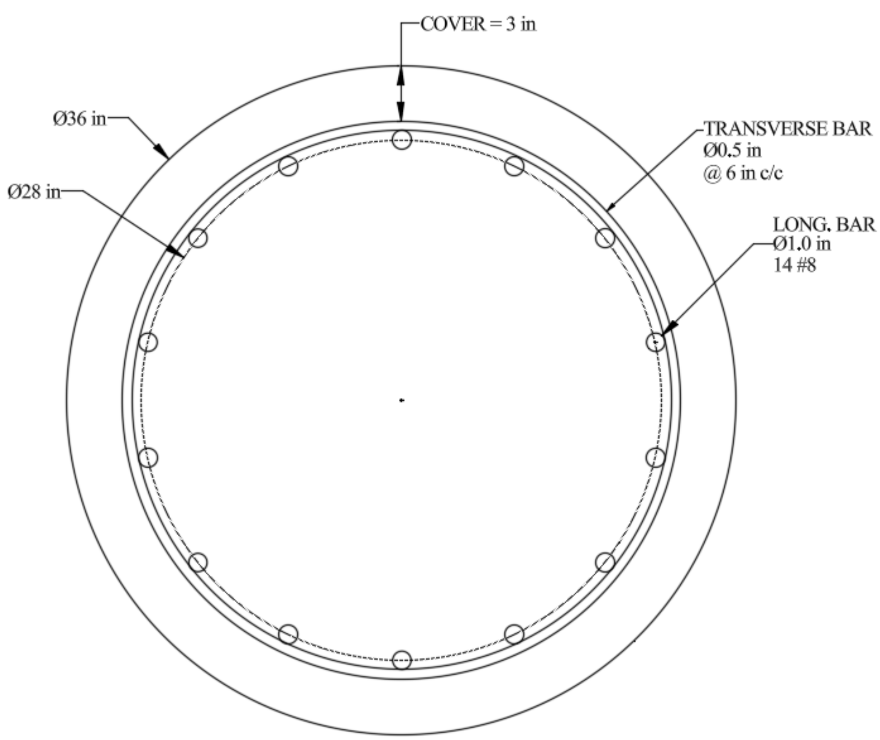

Figure 3-25. Structural design of the drilled shafts.

Anchor Bolt System

The anchor bolt system providing the connection between the drilled shaft and the arm loading system (H-beam) was designed to resist the combined tension and shear demands induced by eccentric loading during the full-scale testing program. The anchorage was designed in accordance with ACI 318-25, Chapter 17 provisions for cast-in headed anchors. The applied design load consisted of a factored eccentric force of 30 kips acting at a lever arm of 4 ft from the center of the shaft, resulting in combined tensile and shear demands on the anchor group.

The anchorage system consisted of six 1.25 in. diameter headed threaded bars, arranged on a 22 in. bolt circle, with a total length of 36 in. and an effective embedment depth of 30 in. into the concrete shaft. The anchors were specified with a yield strength of 120 ksi (Grade 150) and were terminated with Williams R73 1.25 in. hex nuts. Anchor spacing and edge distances satisfied the minimum requirements prescribed by ACI 318-25 to prevent group interaction and premature concrete failure.

Tensile capacity was evaluated considering steel strength of the anchors, concrete breakout strength of the anchor group, pullout strength of individual anchors, and concrete side-face blowout strength of headed anchors. Shear capacity was evaluated based on steel strength of anchors in shear, concrete breakout strength in shear, and concrete pryout strength. In all cases, the governing factored resistance exceeded the corresponding applied demand. The controlling limit states were identified through comparison of reduced strengths, and adequate reserve capacity was observed for all failure modes.

Overall, the anchor bolt system satisfied all applicable strength and detailing requirements of ACI 318-25 for the imposed loading conditions. Detailed calculations, governing failure modes, and design interaction results are provided in Appendix B.

Base Plate

The baseplate for the shaft loading system was designed in accordance with AISC provisions to ensure adequate strength under a load of 106 kips and a resulting bending moment of 145.3 kip-in. The plate geometry consisted of a 1.25 in. thick plate with a 22 in. bearing width on the H-pile and six 1.25 in. diameter anchor bolts. Tension rupture and tear-out of the plate were checked using the effective net area and bolt line geometry, and both limit states satisfied the required strength with factors of safety well above the AISC minimums. Shear yielding and shear rupture of the plate were also evaluated along the 22 in. bearing width, showing large reserve capacity relative to the applied shear demand. Plate bending was evaluated using both the elastic and plastic section modulus, with plastic bending capacity Mn = 34.18 kip-ft providing more than twice the required strength. Weld design was performed using E70 electrodes, with a 5/16 in. fillet weld along both sides of the H-pile providing a nominal weld capacity of 408 kips, well above the applied demand.

3.4.2. Instrumentation Plan

To evaluate the performance of drilled shafts under combined lateral and torsional loading, the full-scale testing system was instrumented to monitor structural response throughout the loading process. The instrumentation setup was designed to capture key parameters, including displacements, rotations, and stresses. This system included string potentiometers to measure horizontal and vertical displacements, vibrating wire (VW) load cells to monitor externally applied loads, and VW and foil strain gauges to track internal forces within the shaft. Hydraulic actuators were used to apply controlled lateral and torsional loads. Data from all sensors were continuously collected using a centralized datalogger, enabling real-time monitoring and high-resolution analysis of the structural behavior of the shaft during testing.

Internal Instrumentation of the Shaft

The rebar cage of the shaft was instrumented along two longitudinal reinforcement bars located on opposite sides of the cross-section. Instrumentation was installed at four different embedment depths along each of these two faces, as illustrated in **Figure 3-26**. The first instrumentation level was located at ground level, while the remaining three were spaced at 36-inch intervals along the vertical axis.

Each instrumentation level included one foil strain gauge oriented vertically and two vibrating wire (VW) strain gauges oriented at 45 degrees relative to the horizontal. Additionally, the second and fourth levels were equipped with a second set of torque-pattern foil strain gauges, also placed at 45 degrees. The vertical foil gauges captured axial strain, while the 45-degree gauges (both foil and VW) measured strain associated with shaft rotation or torsional deformation.

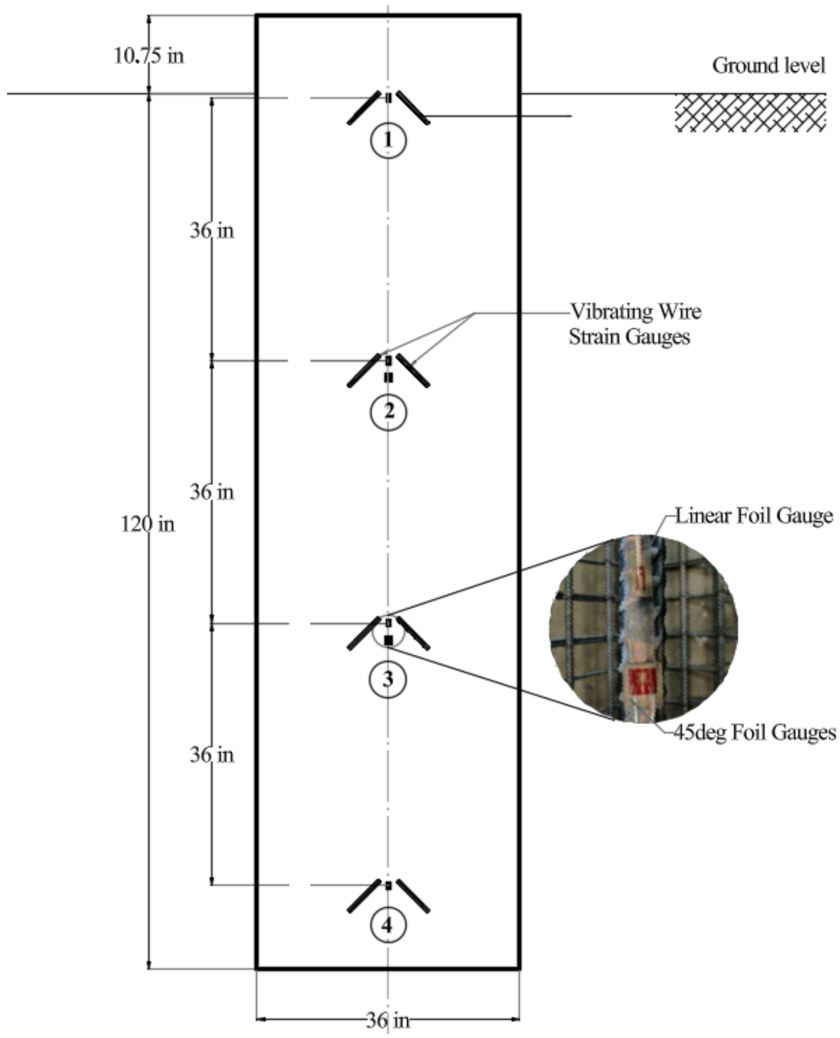

Figure 3-26. Internal instrumentation representation of the shafts.

Foil Strain Gauges

Foil strain gauges were used in this project to measure strain both along the longitudinal axis of the shaft and at a 45 degrees angle to the horizontal. This configuration leverages the fact that maximum shear stresses and strains typically occur on planes oriented at approximately 45 degrees to the shaft axis.

A foil strain gauge consists of a metallic foil arranged in a precise grid pattern and bonded to a thin backing material that provides mechanical support and electrical insulation from the surface to which it is attached. These gauges operate on the principle that when a conductor is stretched or compressed, its electrical resistance changes in a predictable way. As the structure deforms under applied loads, the strain gauge deforms proportionally, causing slight changes in both the length and cross-sectional area of the metallic grid. This deformation induces a corresponding change in electrical resistance, which is then converted into a measurable voltage signal through a Wheatstone bridge circuit.

Figure 3-27. Foil strain gauges used for this project (TML, n.d.)

Vibrating Wire Strain Gauges

To measure the torsional effects in the shafts, Vibrating Wire Strain Gauges were utilized. A VW strain gauge consists of a tightly stretched wire inside a protective housing, which is anchored to the material being monitored. When the material deforms due to applied loads, the strain gauge experiences tension or compression, changing the tension in the vibrating wire. The working principle is based on the relationship between wire tension and vibration frequency. An electromagnetic coil plucks the wire, causing it to vibrate at its natural frequency. This frequency is directly related to the strain in the material. By measuring the frequency shift, strain can be determined over long periods, making vibrating wire strain gauges particularly useful for long-term structural health monitoring.

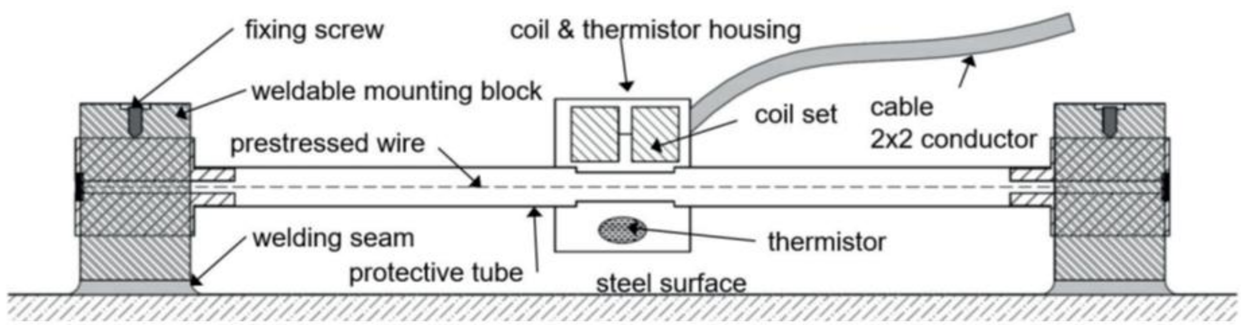

Figure 3-28. VW Strain Gauge Representation (GeoData, 2020)

String Potentiometers

String potentiometers were used to measure lateral and rotational displacements at the top of the drilled shafts. A string potentiometer, also known as a draw-wire sensor, is a device that measures displacement by converting linear motion into an electrical signal. It features a retractable steel or nylon cable wound around a precision drum connected to a rotary potentiometer. As the transducer cable extends or retracts with the displacement of the element, the drum or spool within the transducer housing rotates, leading to the rotation of the rotary sensor. The alteration in the resistance of the potentiometer results in an output voltage signal proportional to the linear extension or velocity of the cable (te.com).

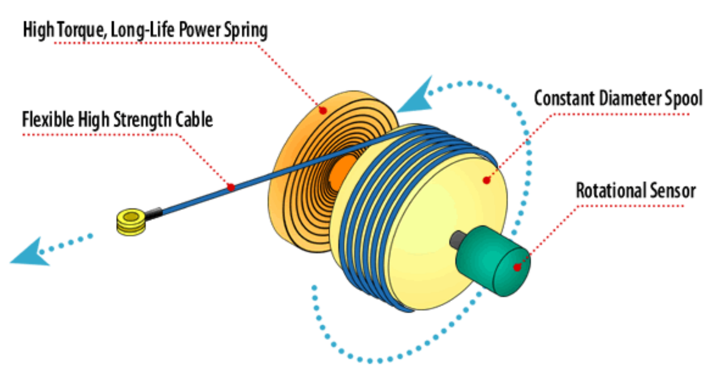

Figure 3-29. String Potentiometer Operation (TE Connectivity, n.d.)

Vibrating Wire Load Cells

The lateral and torsional loads exerted on the drilled shafts were measured and tracked using load cells. The load cells were located between the reaction block and the hydraulic jack to register the forces exerted through the pulling mechanism. Two Vibrating Wire (VW) load cells (3 in. diameter) rated at 200 kips were used for this purpose.

A load cell functions as a force transducer, converting an applied load into an electrical signal for accurate force measurement. The load cells acquired for the tests (4900 VW) features an annular design. This model includes a high-strength steel cylinder that contains embedded wire strain gauges (three to six) to measure changes in strain. The vibrating wire principle operates as follows: Inside the load cell, tightly stretched steel wires experience tension changes when the body of the load cell deforms slightly under applied load. The wire vibrates at a natural frequency (which depends on its tension). The variation in the frequency (Hz) is registered and converted into strain, which can then be analyzed to ascertain the magnitude of the applied force.

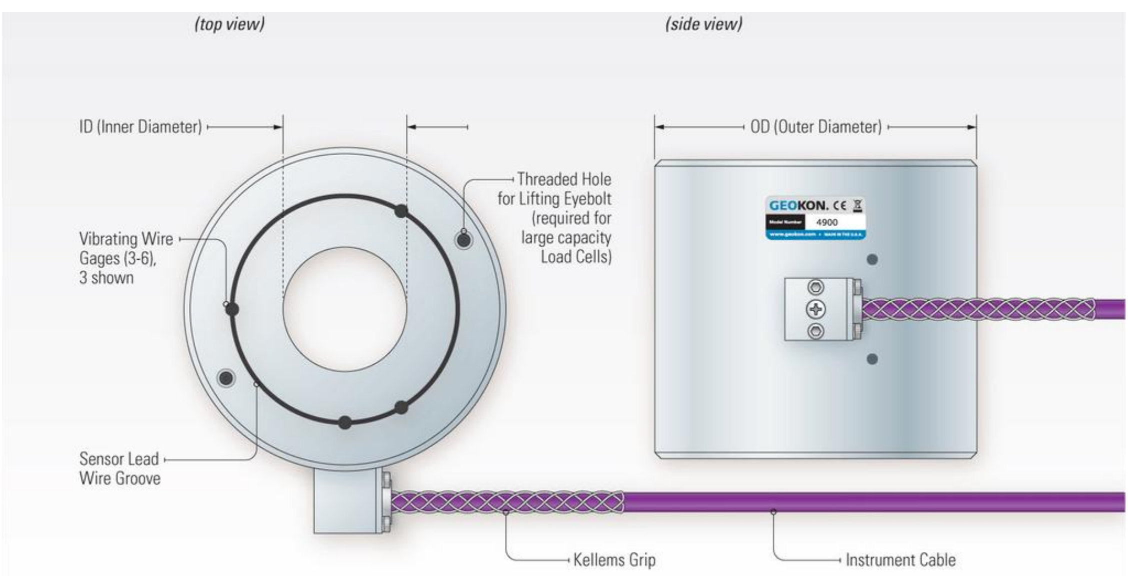

Figure 3-30. Acquired Load Cell Components. 4900 VW load cell. (Geokon, n.d.)

Data Logger

The signals from the potentiometers, load cells, and strain gauges were recorded in real-time using a data acquisition system that uses Campbell Scientific CR6 or CR1000 (**Figure 3-31**) dataloggers. Dataloggers are essential devices used to record measurements from sensors and instruments over time automatically. It typically serves three main functions: signal conditioning (applying calibration factors, filtering noise, or converting signals), data acquisition (collecting analog or digital signals from connected sensors), and data storage and communication (saving the measurements locally and transmitting them to external systems for monitoring or analysis).

Figure 3-31. CR1000 data logger (Campbell Scientific, n.d.)

The CR6 and CR1000 data loggers from Campbell Scientific share several core features that make them reliable and versatile geotechnical data acquisition tools. Both systems support data logging with timestamped records and offer real-time monitoring. They operate using CRBasic, a programming language for customized measurement schedules, control logic, and real-time calculations. These data loggers are compatible with a broad range of sensors, including those that measure voltage, current, resistance, digital pulses, and communication protocols like SDI-12, RS-232, and RS-485.

Hydraulic Jack

A hydraulic actuator is a mechanical device that converts the energy of pressurized hydraulic fluid (usually oil) into linear or rotary motion**.** The setup of a horizontal load actuator tends to be bigger and more complex than that of a general hydraulic jack. Instead of a conventional horizontal actuator, the system for the full-scale load tests will employ hydraulic jacks to apply pulling forces to an H-pile attached to the drilled shafts via anchor bolts. The jacks – Power Team SPX 60-ton hydraulic 10-1/8 double-acting cylinder center-hole models (**Figure 3-32**) – pulled all-thread bars connected to the H-Pile to apply the desired loads to the shafts.

Figure 3-32. 60 Ton hydraulic jack (Ohio Power Tool, n.d.)

CHAPTER 4. Full-Scale Load Tests

4.1. Instrumentation and Construction of Test Shafts

4.1.1. Instrumentation of Test Shafts

The reinforcement cages for the test shafts were prepared at ASEL in accordance with the design requirements previously described in 3.4.1. Each shaft was instrumented with strain gages to measure bending and shear strains during load testing at four levels along the shaft length as shown in Figure 4-1. Vibrating wire concrete embedded strain gages were installed at 45^{o} from the vertical (without contact to steel) to monitor shear strains, while resistance (foil) gages were installed on the rebars to monitor bending due to lateral loading. At levels 2 and 3, rosette foil gages were also installed to monitor shear strains as a backup to the VW gages. The gages were installed on two opposite sides of each shaft.

4.1.2. Construction of Test Shafts

Russo Corporation was contracted to perform the drilling operations in the Geotechnical Chamber. A Long Reach (LR75) Caterpillar 330 Next Gen excavator equipped with an auger drill bit (Figure 4-2) was used for the construction work. During a coordination meeting between the Russo crew and the Auburn research team, it was determined that the shafts would be constructed sequentially (i.e. one shaft per day) to allow for proper setup, alignment, and inspection between pours.

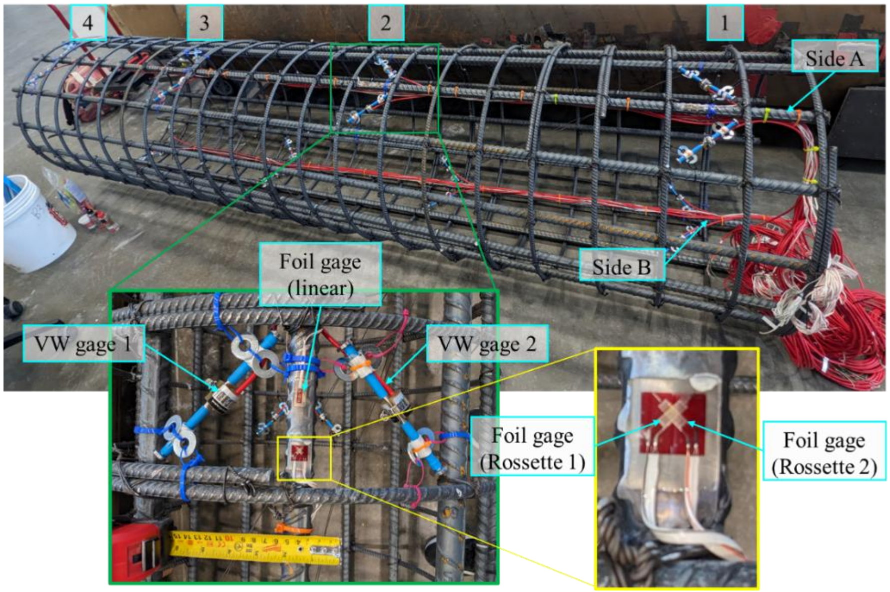

Figure 4-1. Installation of strain gages to monitor shaft response to loading

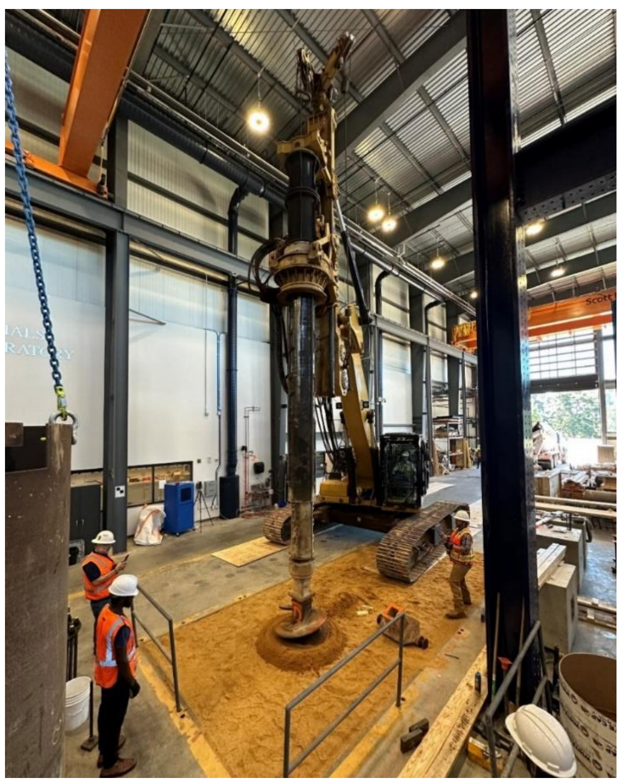

Figure 4-2. Excavating hole using the drill rig from Russo Corporation

The construction of each shaft followed the procedure outlined below:

- Step 1: The drill bit was centered and aligned with the layout marks, and the hole was pre-drilled without casing to a depth of approximately 4 ft.
- Step 2: The steel casing was positioned, vibrated into place, and drilling continued through the casing to the required depth of roughly 10 ft.
- Step 3: The reinforcing cage was lifted into position inside the casing and aligned according to the testing configuration.
- Step 4: Concrete was placed using a crane and hopper while the casing remained in place to maintain verticality and prevent soil collapse.
- Step 5: After the initial placement, the steel casing was pulled out, and a Sonotube® was positioned 11 in. above the strong-floor level. The Sonotube® was secured using timber bracing, and the anchor bolts were positioned and aligned in accordance with the test plan.
- Step 6: Concrete was poured into the Sonotube® to the final elevation to complete the shaft.

Figure 4-3 (a) through (f) illustrates the construction sequence for the test shafts constructed on the first day. The same sequence was followed on the second day for the second shaft and Figure 4-4 shows both completed shafts following construction. The first shaft was cast on 27 August 2025, and the second shaft was completed on 28 August 2025.

The thermocouple wires installed mid-length in both shafts were connected to a Campbell Scientific CR6 datalogger (housed in the white box in Figure 4-4) to monitor the temperature of the concrete over time. Temperatures were recorded in both shafts as well as in two cylindrical concrete specimens cast from each shaft. A brief interruption in data collection occurred due to a battery power outage; however, the available data was sufficient to characterize the overall temperature trends.

Figure 4-5 shows the temperature reading from 8/27/2025 to 9/22/2025. The heat of hydration clearly peaked on the second day after the construction of each shaft (~ 50C), rapidly reduced to ~32C in the next four days before the power outage, then generally stayed at 25C over the last 15 days indicating the completion of the hydration process.

Figure 4-3. Construction sequence illustrating steps 1 through 6 shown in panels (a) through (f) respectively for the first shaft

Figure 4-4. Both constructed shafts at the end of construction

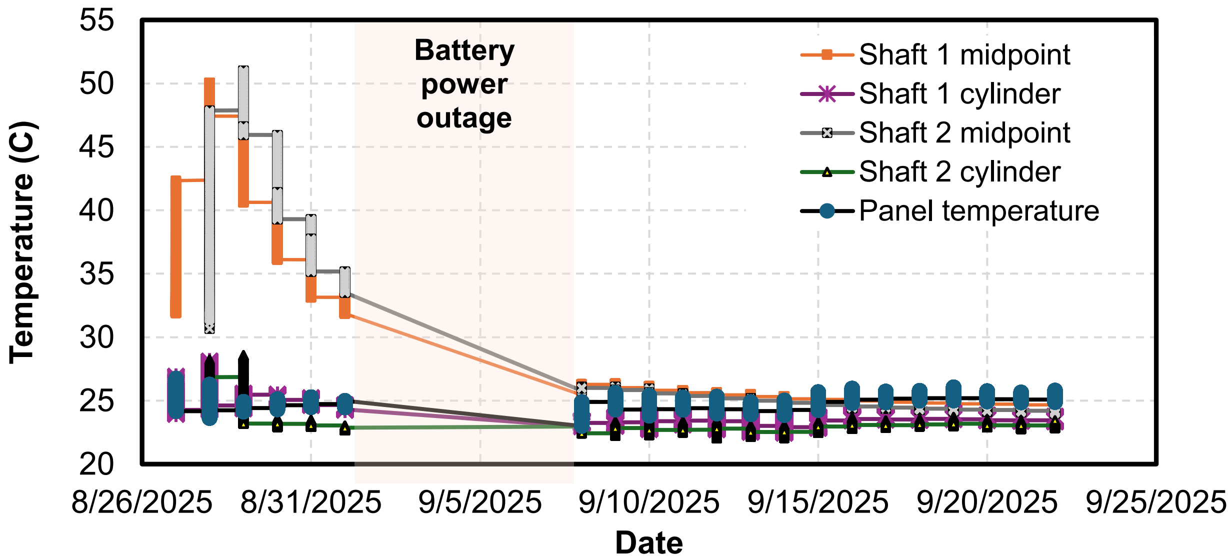

Figure 4-5. Plot of temperature history for both constructed shafts and the respective concrete cylinder specimens

Figure 4-6 presents the compressive strength results obtained from 4 × 8 inches cylindrical concrete specimens cast from Shaft 1 and Shaft 2. For Shaft 1, the average compressive strength was approximately 5500 psi at 7 days, increasing to about 6400 psi at 14 days, and reaching 7500 psi at 28 days. Similarly, for Shaft 2, the average strength was about 6250 psi at 7 days, increasing to approximately 7200 psi at 14 days, and achieving 8240 psi at 28 days. The consistent gain in strength with curing time indicates proper hydration and satisfactory concrete quality in both shafts.

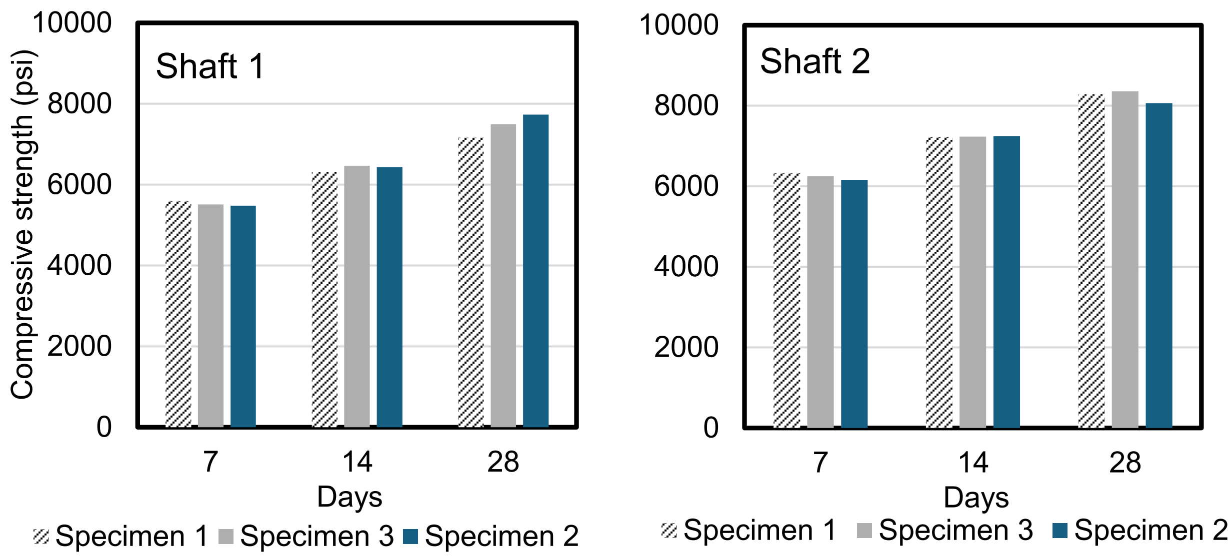

Figure 4-6. Compressive strength results from specimens from Shafts 1 and 2

4.2. Test Setup

The objectives of the tests were to: (1) characterize the structural and geotechnical response of the shafts under different loading modes, (2) identify potential interaction effects between torsional and lateral loading, and (3) provide experimental data for model validation. Figure 4-7 through Figure 4-9 provide details of the plan, back, and front views of the complete loading system.

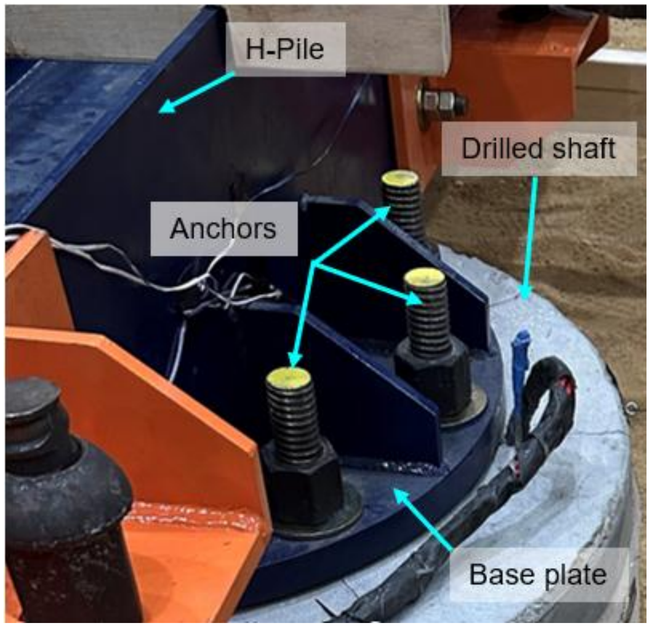

Figure 4-7. Fitting the plate holes with the anchors sticking out of the drilled shaft surface

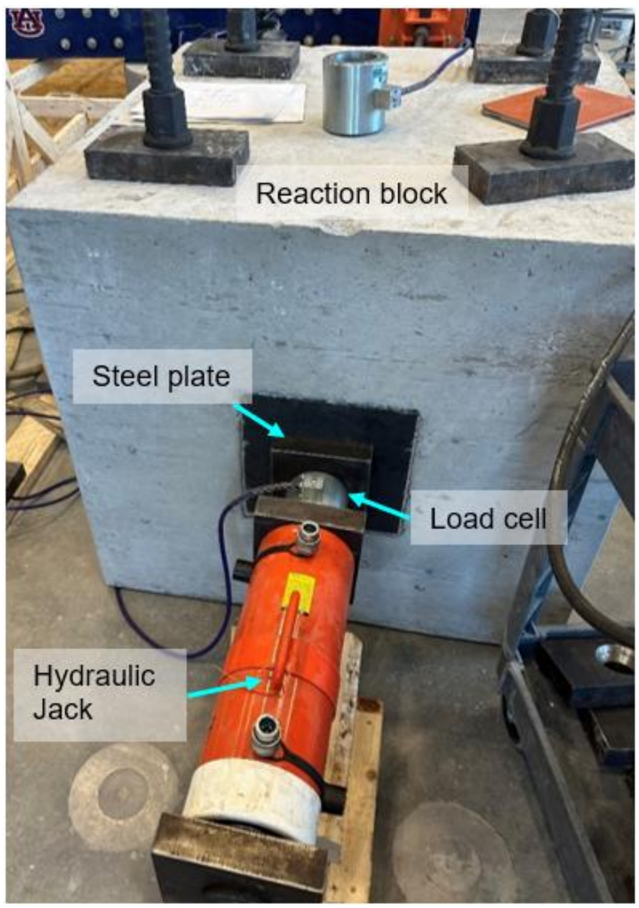

Figure 4-8. Load and reaction setup (back side)

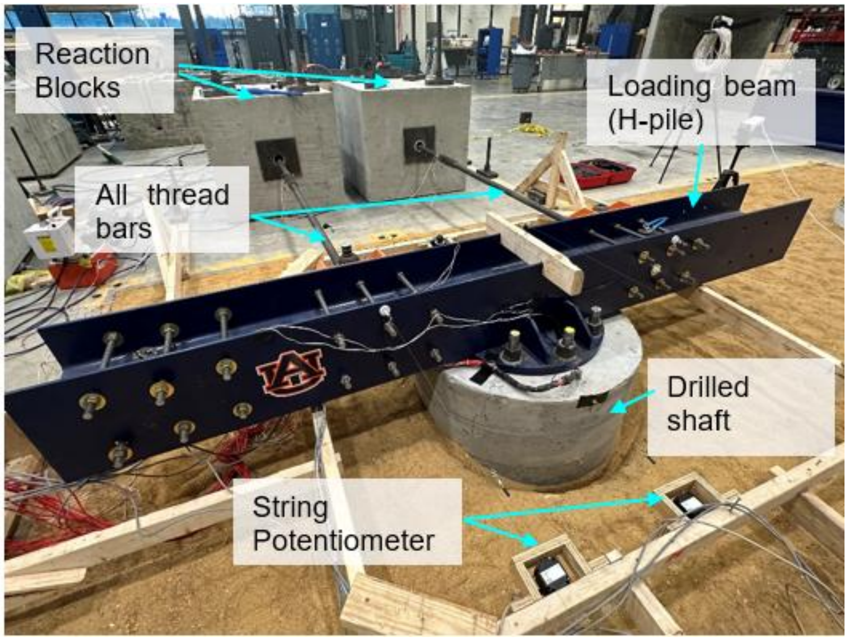

Figure 4-9. Loading mechanism, front side.

4.3. Load Testing

4.3.1. Phase I

- **Purely Torsional Test A (Shaft #1)**

The shaft was installed so that the longitudinal axis of the loading arm was initially oriented approximately 12° relative to the chamber's longitudinal axis. This setup ensured that, upon completion of the torsional loading sequence, the loading arm would rotate into alignment with the chamber for the subsequent lateral test.

Torsional loading was applied using two hydraulic jacks operating simultaneously in rotation-control mode. Each load step was held for approximately 20 minutes to allow stabilization and complete data acquisition.

The rotation-control increments were:

- 0.1° from 0° to 1.0°
- 0.3° from 1.0° to 5.0°

- ~1.0° increments from 5.0° to 12.0° (target rotation)

The system applied equal-magnitude, opposite-direction loads at 4 ft from the shaft center to produce a nearly pure torsional response (Figure 4-10). Slight load imbalance between the two sides was expected and considered acceptable. The total test duration was approximately 13 hours.

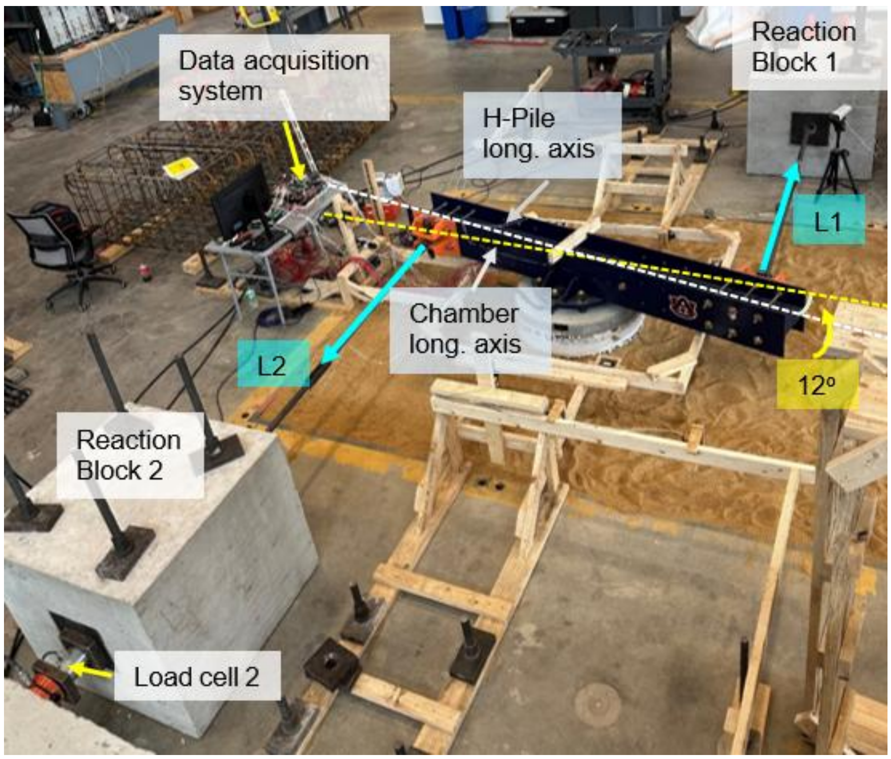

Figure 4-10. Loading setup of purely torsional test.

Loading Imbalance Event

After reaching ultimate capacity, the rotation was continued to 12° to align the shaft for the next test.

At step #32, a sudden load imbalance occurred:

- Load Cell 1 dropped from ~21 kips to ~9.6 kips
- Load Cell 2 spiked from ~19 kips to ~29.5 kips
- Rotation at event: ~9°

Surface cracking appeared at the shaft due to the imbalance (Figure 4-11a). Inspection revealed that the hydraulic jacks had reached a stroke length of approximately 10.7 in. (Figure 4-11b), exceeding the manufacturer limit of 10.125 in. Considering that the load cell 1 values were slightly higher throughout the test, the hydraulic jack 1 might have reached its maximum stroke length first. This likely caused the full hydraulic pressure to transfer to the opposite jack, triggering the imbalance.

Cracks followed the direction of rotation but did not exhibit the expected ~35° torsional failure cone. The widest crack (orange color) presented an approximate 90° propagation from the anchor to the shaft edge.

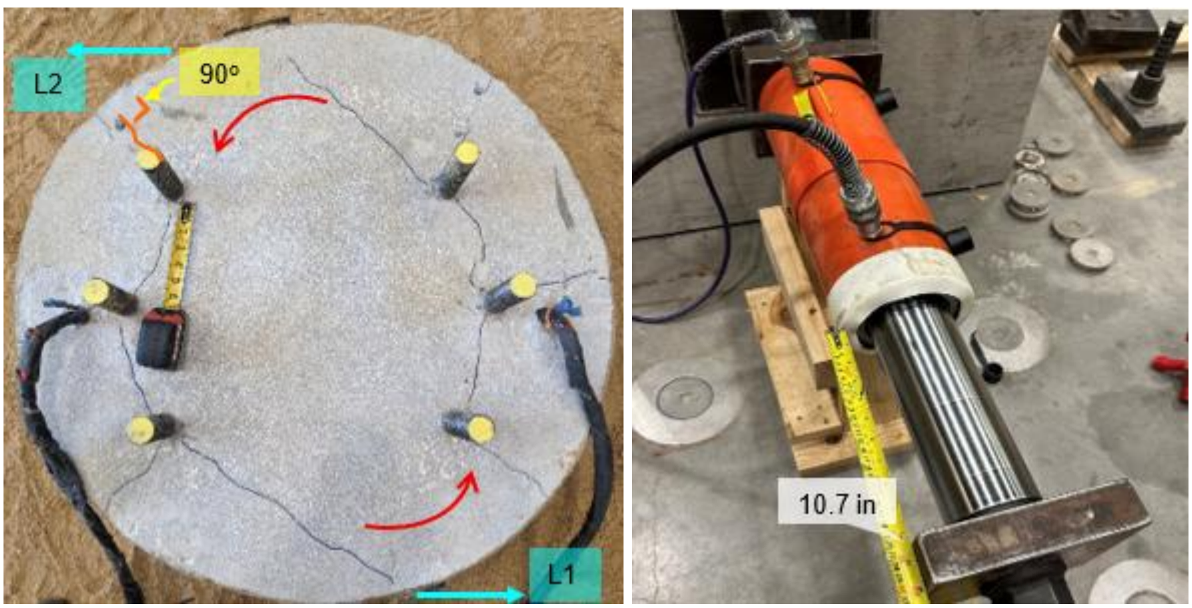

Figure 4-11. a) Cracks appeared on the shaft surface after a sudden imbalance, b) Stroke length reached by hydraulic jacks.

After unloading and pausing overnight, the system was reloaded without further imbalance, and the target rotation was successfully reached. The cracking did not compromise the structural integrity required to continue testing.

- **Lateral Load After Torsional Test A (Shaft #1)**

Following the torsional test, the reaction blocks were repositioned on the same loading side, at 2 ft from the shaft center. Equal-magnitude lateral loads were applied simultaneously at both locations (Figure 4-12).

Loads were applied in magnitude-controlled increments with ~20-minute hold periods. The test duration was approximately 3 hours.

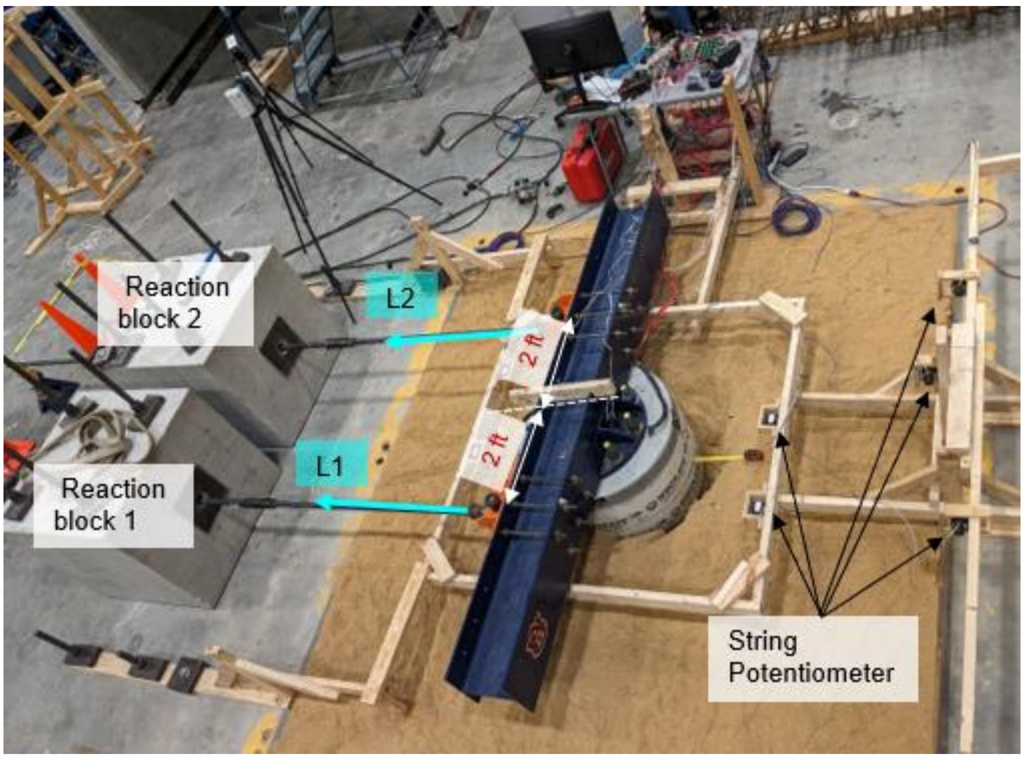

Figure 4-12. Lateral test setup applied to the torsionally failed drilled shaft

Observed lateral displacement patterns are shown in Figure 4-13 (back and front views). The orange lines in the front view of the figure represent the soil mobilization patterns due to the applied lateral load. Although the observed soil mobilization pattern extends to the chamber wall, the maximum lateral displacement during testing was approximately 4 in., a magnitude used only for experimental purposes and not representative of acceptable field performance. In practical applications, drilled shafts supporting mast arm structures would typically be governed by serviceability limits at substantially smaller displacements. Therefore, the confinement effects associated with interaction between the mobilized soil mass and the chamber boundaries are not expected to significantly influence shaft behavior within the displacement range relevant to design and serviceability considerations.

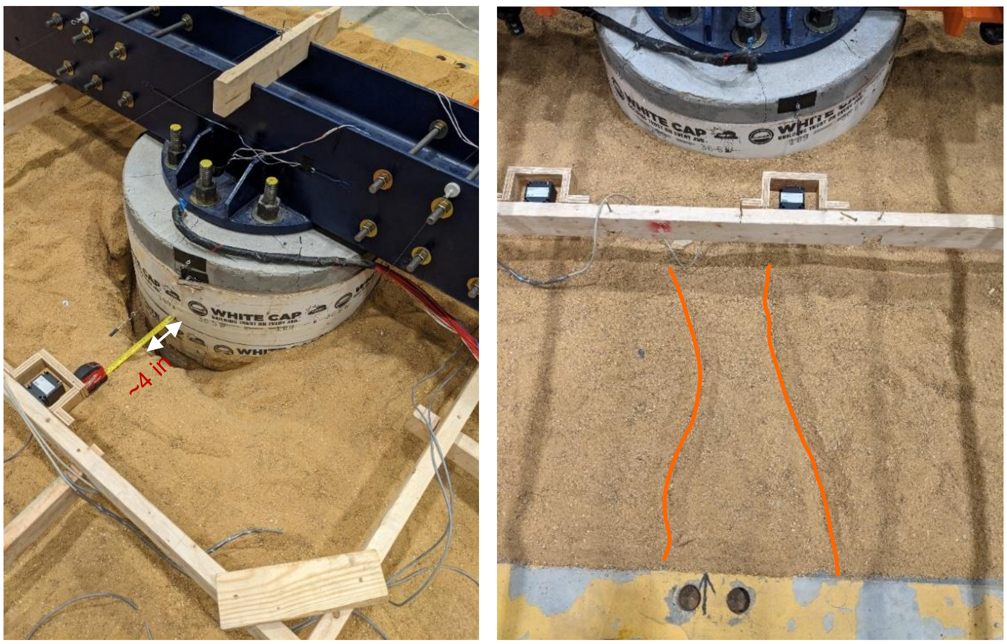

Figure 4-13. a) Lateral displacement of the shaft, back view, and b) front view

- **Combined Lateral-Torsional Test A (Shaft #2)**

A single lateral load was applied at one end of the loading arm (**Figure 4-14**) to simulate the eccentric loading caused by wind forces on a mast arm and to investigate the resulting combined lateral-torsional response of the shaft. This configuration produced simultaneous lateral displacement and torsional rotation. The test duration was approximately eight hours. Each load increment was held for 10 to 15 minutes to allow stabilization of the measured response before proceeding to the next step. Surface cracking observed during the test is shown in Figure 4-15.

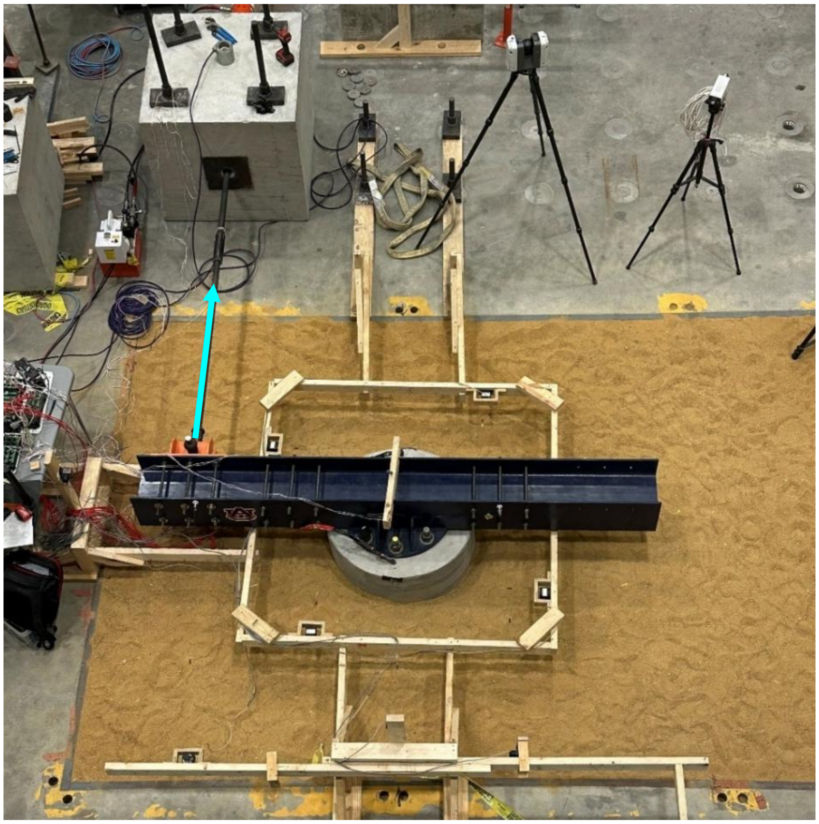

Figure 4-14. Loading setup of the combined lateral-torsional test

Figure 4-15. Cracks appeared at the surface of the shaft 2

- **Lateral Load After Combined Loading Test A (Shaft #2)**

The shaft was then subjected to a purely lateral load (**Figure 4-16)** to evaluate the post-combined-loading behavior. **Figure 4-17** shows the displacement response.

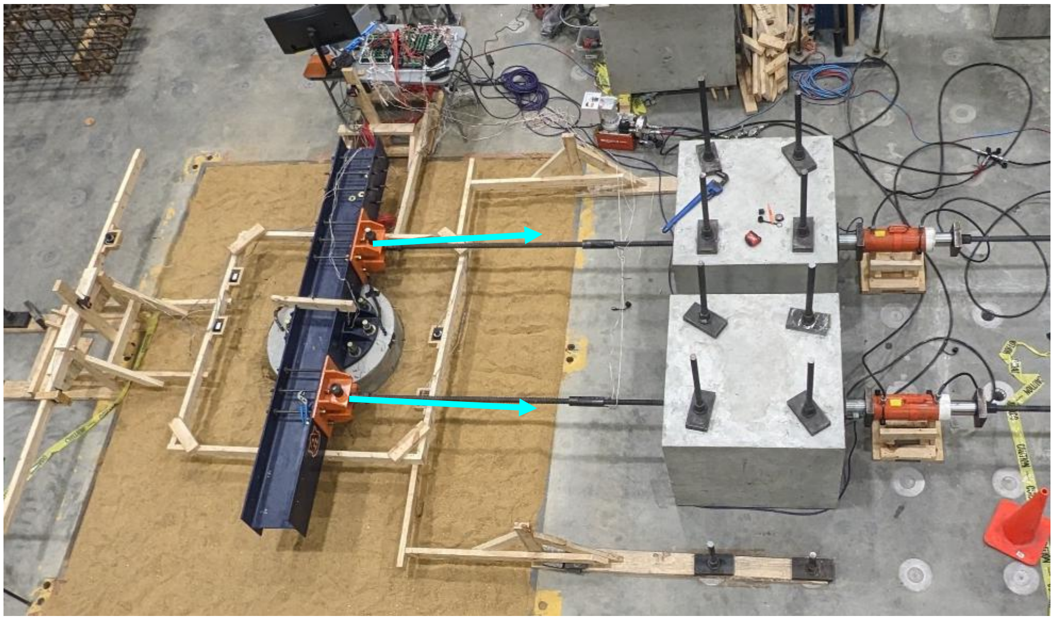

Figure 4-16. Loading setup of the purely lateral load after combined lateral-torsional test

Figure 4-17. Lateral displacement

- **EXCAVATION AND SHAFT EXHUMATION**

Following completion of Phase I, the surrounding soil was carefully excavated to expose both shafts. The objective was to document soil–structure interaction conditions, inspect cracking, and prepare for recompaction procedures.

Photographic documentation was collected at each stage and is presented in **Figure 4-18**.

Figure 4-18. Excavation and exhumation of the shafts

- **RECOMPACTION AND SHAFTS RE-INSTALLATION**

After exhumation, the soil was replaced and recompacted in controlled lifts to restore uniform boundary conditions.

The recompaction procedure included: placement of sand, alignment and re-installation of the shafts within the chamber, compaction using a vibratory plate tamper, verification of target density using sand-cone tests. This process ensured repeatable conditions for Phase II testing.

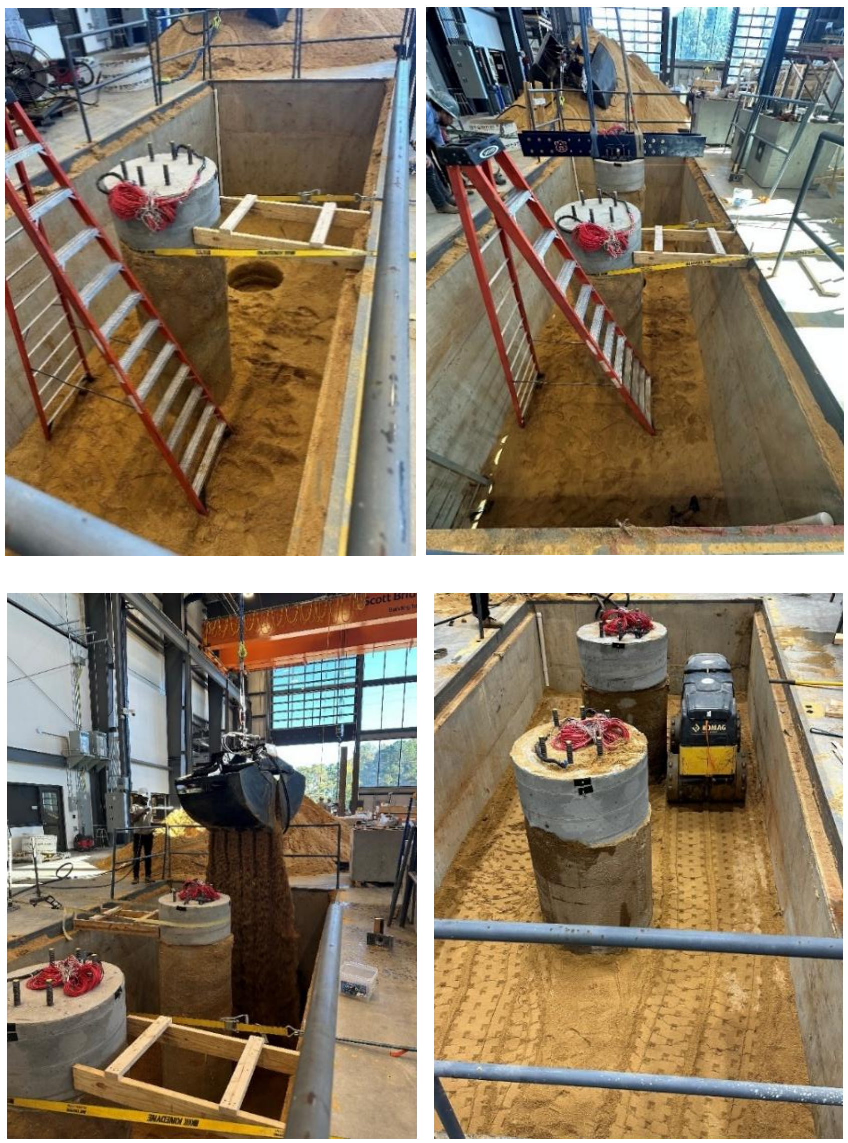

Figure 4-19. Reinstallation of drilled shafts for Phase II testing.

4.3.2. Phase II

- **Purely Lateral Test B (Shaft #1)**

In Phase II, Shaft #1 was re-tested under purely lateral loading to quantify changes in lateral resistance after torsional deformation and subsequent soil recompaction.

The lateral test followed the same loading increments and hold periods used in Phase I, allowing direct comparison of load–displacement behavior between phases.

Figure 4-20. Purely lateral test B setup.

Figure 4-21. Purely lateral test B prior to and after failure.

- **Purely Torsional Test B (Shaft #2)**

Shaft #2 was subjected to a repeat torsional loading sequence under the same conditions used for Test A. The test aimed to quantify potential softening or hardening effects after combined loading; evaluate soil-structure interaction under recompacted conditions; and compare torque-rotation curves between Phase I and Phase II.

Figure 4-22. Purely torsional Test B setup.

- **Lateral After Torsional Test B (Shaft 2)**

The final test involved applying a lateral load to Shaft 2 immediately after completing the torsional loading in Phase II. The objective was to evaluate whether torsion-induced soil disturbance influenced lateral response.

Figure 4-23. Lateral after torsional test B setup.

- **FINAL EXCAVATION AND EXHUMATION**

Upon completion of all tests, both shafts were excavated to document final soil conditions and structural response. **Figure 4-24** shows the exhumation of Shaft 2.

Figure 4-24. Exhumation of Shaft 2

Figure 4-25. Exhumed shafts

4.3.3. Load Testing Summary

A total of seven (7) full-scale load tests were performed on two drilled shafts constructed inside the Auburn University geotechnical chamber. All tests were executed using a consistent loading setup and standardized instrumentation layout. The testing program consisted of two phases, each designed to evaluate the torsional, lateral, and combined lateral–torsional behavior of drilled shafts under controlled, repeatable conditions. A summarized description of the performed load tests is presented in **Table 4-1** and **Table 4-2** for Phase I and Phase II respectively.

Table 4-1. Summary of the test setups of Phase I

Setup Index	Test Setup Description	Illustration
T1. Torsional Test A	This loading setup involved applying pure torsional loads to the test shaft to examine its rotational response within the shaft–soil system. Loads of equal magnitude but opposite direction were applied at 1.2 m (4 ft) from the shaft center on the H-pile, aiming to generate a nearly pure torsional response. A minor load imbalance between the sides was anticipated and deemed acceptable. The load steps were managed through shaft rotation in stages: first, 0.1° increments up to 1°, then 0.3° increments up to 5°, and finally 1.0° increments until the target of 12° was reached. Each load step was maintained for about 20 minutes to ensure stabilization and data collection, resulting in a total test duration of roughly 13 hours.	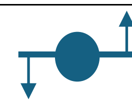

Setup Index	Test Setup Description	Illustration
T2. Lateral after Torsional Test A	In this loading sequence, a lateral load test was conducted on the shaft after it had already failed under torsional loading. Equal-magnitude, equal-direction loads were applied at 0.61 m (2 ft) from the shaft center on the H-pile. The purpose was to assess how prior torsional failure affects the lateral load–displacement behavior of the drilled shaft. Loads were applied in magnitude-controlled increments with ~20-minute hold periods. The test duration was approximately 3 hours.	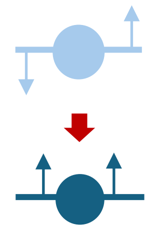
T3. Combined Lateral-Torsional Test	In this loading setup, the test shaft was subjected simultaneously to torsional and lateral loads to assess its combined response. A single lateral load was applied to one side of the loading arm, 1.2 m (4 ft) from the shaft center. This unilateral application produced a lateral force and a torsional moment due to the eccentricity. This method simulated the eccentric resultant load transferred to shafts supporting mast arms under imposed wind forces. Each load step was maintained for 10–15 minutes, for a total test duration of around 8 hours.	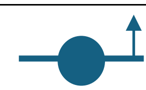

Setup Index	Test Setup Description	Illustration
T4. Lateral after Combined Lateral-Torsional Test	In this testing setup, a lateral load was applied to the shaft after it had previously undergone combined lateral-torsional loading to failure. The purpose was to evaluate how the earlier failure impacted the subsequent lateral resistance of the shaft. The loading increments and hold times were similar to those used in the previous lateral tests. The shafts were excavated after this load test to allow for their later reinstallation and compaction as part of phase two.	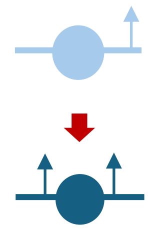

Table 4-2. Summary of the test setups of Phase II

Setup Index	Test Setup Description	Illustration
T5. Lateral Test	This was the first test of the second phase of testing. The test shaft was subjected to a lateral loading configuration to evaluate its horizontal load–displacement response. This test followed the same loading increments and hold periods used in Phase I, allowing direct comparison of load–displacement behavior between phases.	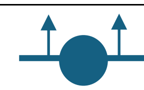

Setup Index	Test Setup Description	Illustration
T6. Torsional Test B	In this testing setup, the shaft was subjected to a repeated torsional loading sequence under the same conditions used for T1. The test aimed to evaluate soil-structure interaction under recompacted conditions and to compare torque-rotation curves between Phase I and Phase II.	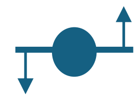
T7. Lateral after Torsional Test B	This final test involved applying a lateral load to the shaft immediately after completing the torsional loading in Phase II. The objective was to evaluate whether torsion-induced soil disturbance influenced lateral response.	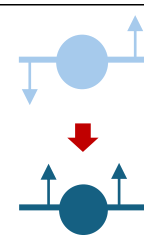

4.4. Test Results

4.4.1. Torque-Rotation Response for Torsional and Combined Tests

Pure torsional tests were conducted in both phases of the experimental program (T1 and T6). For these tests, hyperbolic torque-rotation relationships were observed.

In test T1, the measured torque increased rapidly at very small rotations, reaching approximately 103 kip·ft (~70% of the ultimate capacity) at rotations of less than 1°. Beyond this stage, the torque continued to increase at a reduced rate, indicating nonlinear stiffness degradation with increasing rotation. The torque gradually approached a peak value of 148 kip·ft at approximately 7° rotation, beyond which no further increase was observed, indicating that the shaft had reached its ultimate torsional capacity.

Following re-positioning and recompaction, test T6 was conducted in Phase II using a configuration like T1. The torque–rotation response of T6 exhibited a bilinear trend, closely resembling an elastic–perfectly plastic behavior. The torque increased rapidly at very small rotations, reflecting high initial torsional stiffness, and reached approximately 144 kip·ft (~100% of the ultimate capacity) at rotations of less than 1°. Beyond this point, no significant increase in torque was observed, indicating torsional failure shown by continued rotation without additional resistance.

Figure 4-26 presents the measured torque-rotation responses for tests T1 and T6. Both tests reached comparable ultimate torsional capacities; however, T6 exhibited a steeper initial slope, indicating a higher mobilized torsional stiffness compared to T1. Although both tests were performed under similar loading conditions, they differed in shaft installation procedures.

In T1, shafts were constructed by excavating the soil and casting concrete, a process that can induce stress relief and disturbance in the surrounding soil, potentially leading to imperfect shaft-soil contact. In contrast, T6 involved exhuming previously constructed shafts and reinstalling them in the geotechnical chamber, followed by placement and compaction of soil around the shaft.

These differences in installation procedures provide a mechanistic explanation for the observed variation in initial stiffness. The improved soil-structure interface conditions in T6 resulted in greater mobilized torsional stiffness compared to T1.

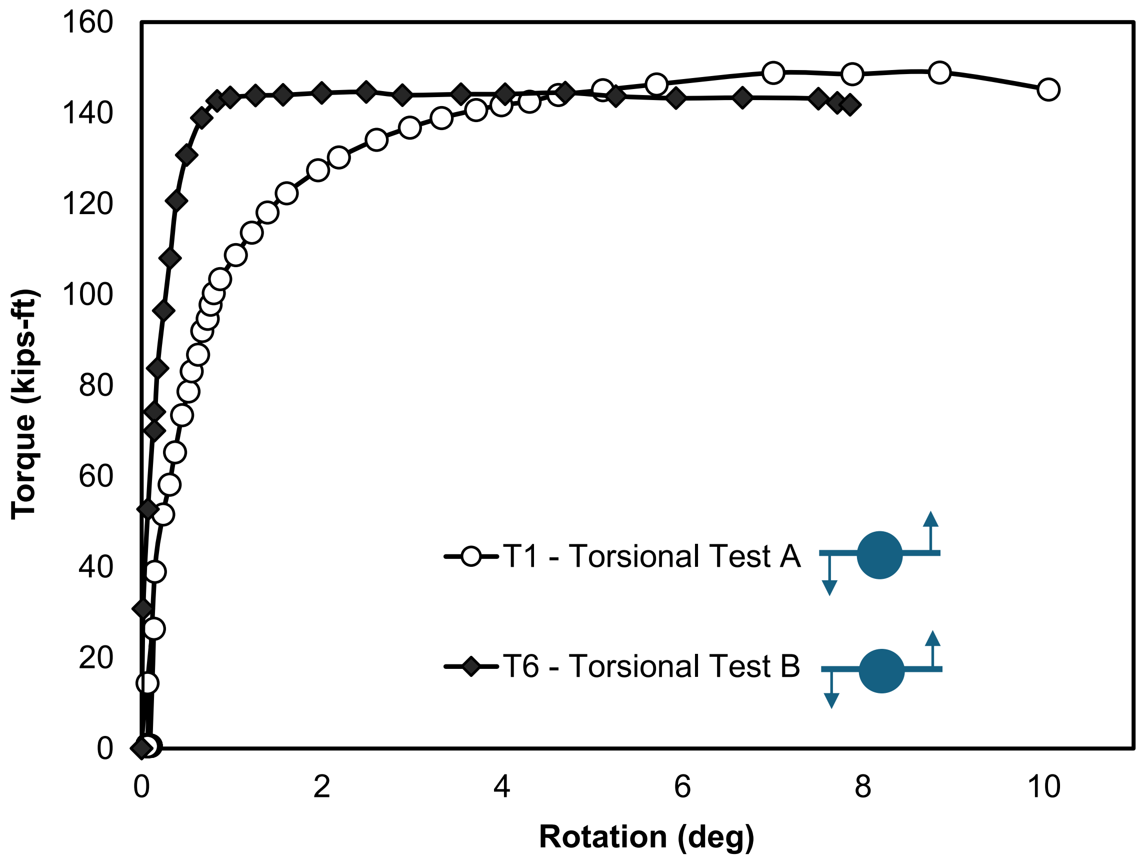

Figure 4-26. Torque vs. rotation responses of tests T1 and T6.

A combined lateral-torsional test (T3) was also performed. The torque-rotation response exhibited an approximately linear increase up to 96 kip·ft at a rotation of 1.3°. Beyond this range, the slope decreased, and the torque gradually increased to about 148 kip·ft at rotations approaching 10°. The absence of a distinct plateau suggests progressive mobilization of torsional resistance under combined loading, reflecting the interaction between lateral deformation and torsional response at the shaft head.

Figure 4-27 compares the torque-rotation responses of the combined test (T3) and the pure torsional test (T1). These tests are compared because both were conducted during Phase I under similar soil and loading conditions. The results highlight differences in the nonlinear transition region of the T-θ curves, which might be associated with progressive mobilization of shear resistance. This behavior is influenced by the coupled lateral-torsional loading effect.

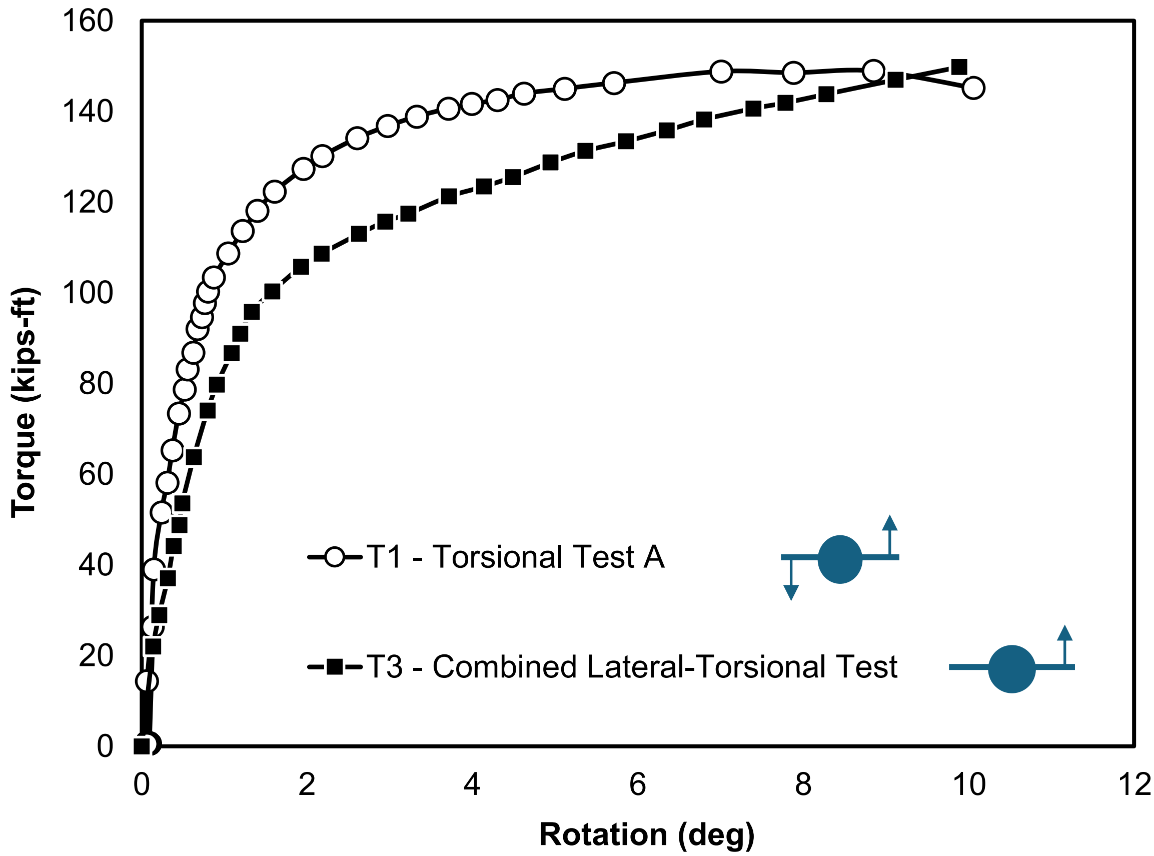

Figure 4-27. **Torque vs. rotation responses of tests T1 and T3.**

4.4.2. Load-Displacement Response for Lateral and Combined Tests

Load-displacement responses were grouped and compared by testing phase. Tests T2 (lateral after pure torsion A) and T4 (lateral after combined loading) were conducted during Phase I. **Figure 4-28** presents the load-head displacement responses for these tests.

For both configurations, the applied load increased rapidly at small displacements, indicating a relatively stiff initial response. As displacement exceeded approximately 1.4 in., the rate of load increase diminished, reflecting progressive nonlinearity in the system. Both tests reached peak loads of approximately 139 kips at head displacements near 2.4 in., beyond which the response exhibited a plateau followed by a reduction in capacity with continued displacement.

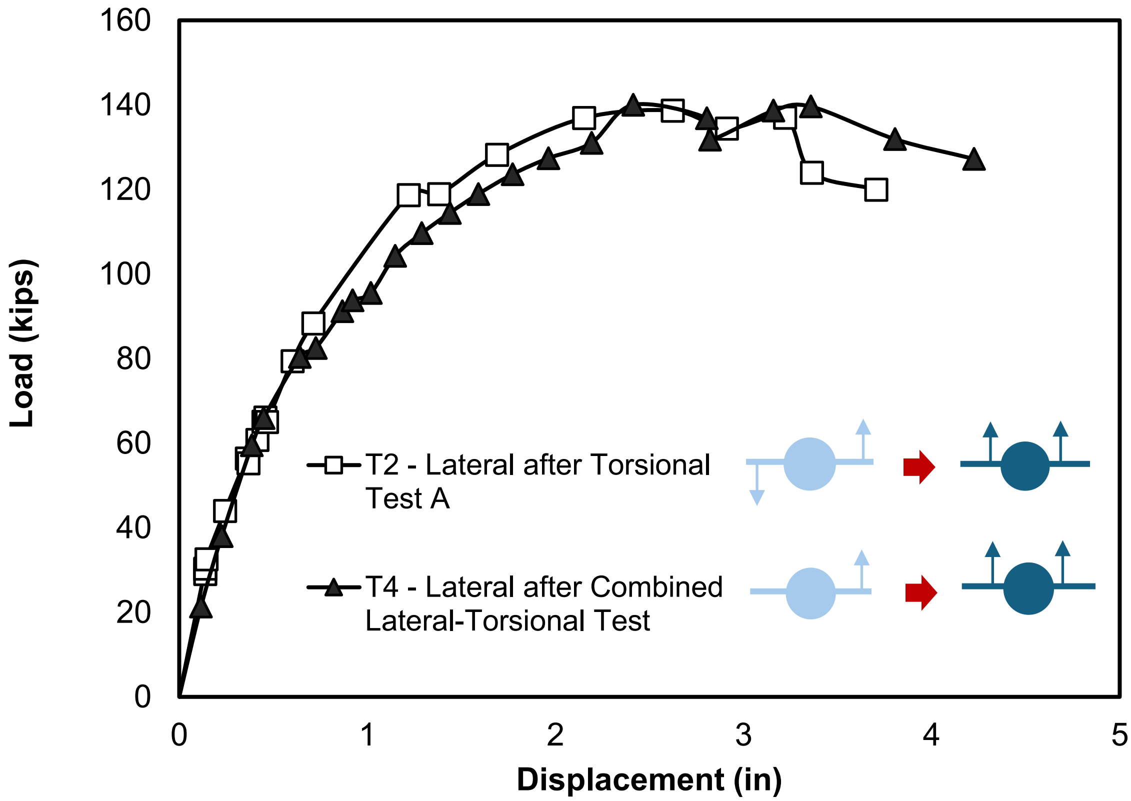

Figure 4-28. Load vs. displacement responses of tests T2 and T4.

Figure 4-29 shows the load-head displacement responses of tests T5 (lateral test) and T7 (lateral after torsional test) conducted during the second phase of testing. In both cases, the applied load increased approximately linearly up to 56 kips at about 0.8 in displacement. Beyond this point, the response became nonlinear with increasing displacement. Test T5 reached a higher peak load of approximately 112.4 kips at a head displacement of 4.7 in., followed by a plateau. In contrast, T7 reached a lower peak load of approximately 103.4 kips at a significantly larger displacement of about 7.5 in., with a more gradual transition toward peak resistance.

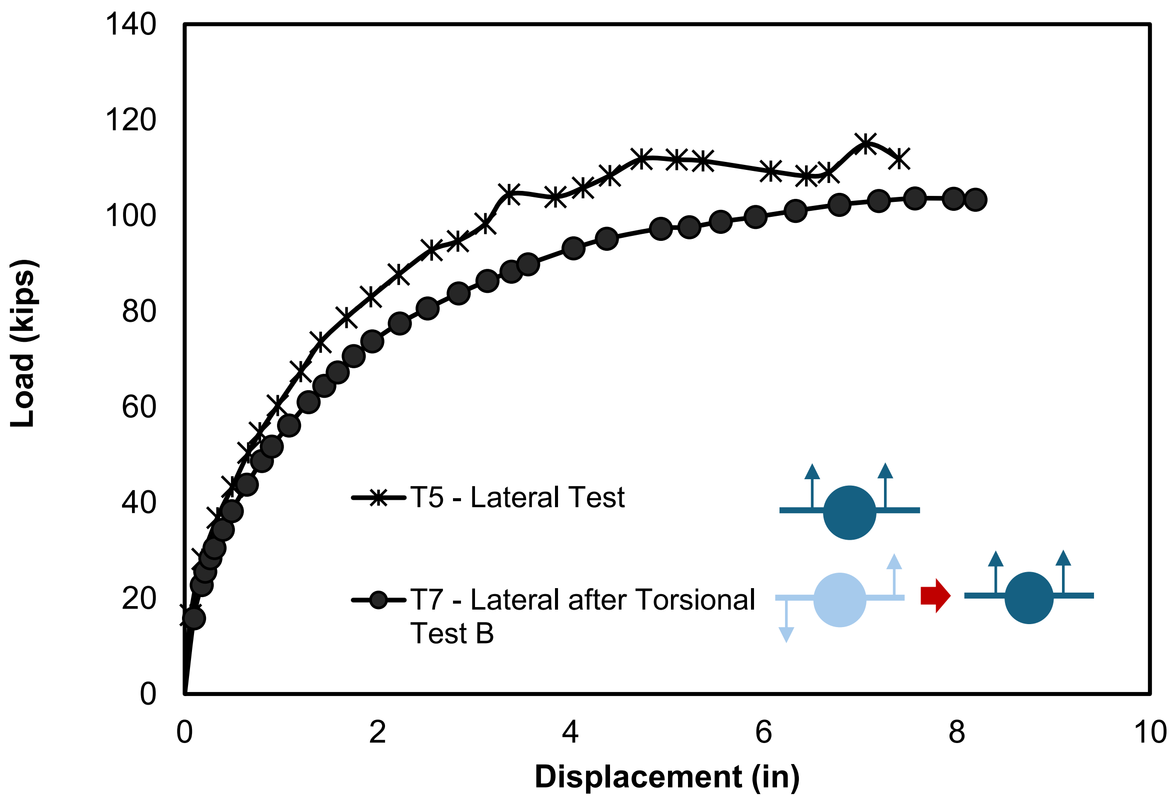

Figure 4-29. Load vs. displacement responses of tests T5 and T7.

4.4.3. Discussion of Results

- **Combined versus Pure Torsional Loading**

A comparison between the combined loading test (T3) and the pure torsional test (T1), shown in **Figure 4-27**, indicates that although both tests reached similar ultimate capacities (~147.5 kip·ft), the mobilization paths differed significantly.

The pure torsional test developed higher torque at much smaller rotations, reflecting a stiffer shaft-soil interface response. In contrast, the combined loading case required substantially larger rotations to mobilize comparable torsional resistance. This behavior suggests that lateral loading alters the stress state along the shaft-soil interface, reducing the initial torsional stiffness and delaying the mobilization of torsional resistance.

- **Lateral Capacity After Pure Torsional Failure versus After Combined Failure**

The similarity in the overall load-displacement envelopes for T2 and T4 suggests that the ultimate lateral resistance is primarily governed by the global soil response rather than localized interface conditions.

However, within the displacement range of approximately 0.75 in. to 2.5 in., corresponding to the nonlinear transition of the curve, T4 exhibits a noticeably softer response compared to T2. This difference may be attributed to the governing failure mechanism of the tests performed before the lateral ones.

- **Lateral Capacity: Effect of Prior Torsional Failure**

The reduced load capacity and softer response observed in T7 (**Figure 4-29**) highlight the influence of prior torsional failure on lateral performance. Compared to T5 (pure lateral), T7 exhibited consistently lower stiffness and reduced peak resistance.

Specifically, T7 showed a peak load approximately 9 kips lower than T5 under similar soil conditions. At larger displacements, this difference decreased to approximately 4 kips, which may partially be attributed to initial imbalance in the load cells observed during testing.

- **Lateral Capacity: Differences between Phase I and Phase II**

A factor that may have influenced the measured lateral responses is the presence of the geotechnical chamber boundaries. The approximately 40% higher lateral resistance observed in the Phase I tests compared to the corresponding Phase II tests may not be solely attributable to loading history or installation effects. Because the loading direction was changed between testing phases, the mobilized soil wedges interacted with different regions of the chamber, potentially altering the degree of confinement provided by the boundaries. Although the individual contributions of boundary effects and loading sequence cannot be quantified independently using the available data, the chamber boundaries likely influenced the measured ultimate lateral resistance. This additional confinement may also partially explain why the numerical models required mobilized strength parameters greater than those indicated by laboratory and in-situ testing, since the Beam-Winkler formulation does not explicitly account for boundary-induced confinement effects.

- **Lateral Load Reduction Factor**

The lateral resistance reduction factor, RT, was calculated as:

RT = (Lateral resistance under combined loading / Lateral resistance under pure lateral loading) × 100

To maintain consistency with the methodology adopted by Hu et al. (2006), the comparison was performed at a common head displacement rather than at the ultimate load. For the present study, the common displacement was approximately 0.24 in., which marks the onset of the ultimate lateral resistance plateau observed during the combined loading test (T3). The lateral resistance measured during the combined loading test was compared with that measured during the Phase I lateral test following torsional loading (T2), since both tests were conducted under the same chamber conditions and soil state.

The results of this study (**Figure 4-30**), when considered alongside previous centrifuge and full-scale experiments, provide additional insight into the reduction in lateral capacity of drilled shafts subjected to combined loading. Prior studies have shown that combined lateral and torsional loading reduces mobilized lateral resistance, with the magnitude of reduction increasing with load eccentricity. Centrifuge tests by Herrera (2001) and Hu et al. (2006) reported significant reductions at high torque-to-lateral load ratios, while full-scale mast arm tests by Thiyyakkandi et al. (2016) demonstrated severe reductions under highly eccentric loading conditions.

The present results, obtained at a torque-to-lateral load ratio of 1.2 m (48 in.), fall between these extremes. Collectively, the available evidence highlights the importance of explicitly accounting for load coupling effects in the evaluation of drilled shaft lateral performance, rather than assuming independent mobilization of torsional and lateral resistance.

It is important to note that, in this study, failure under combined loading was predominantly governed by rotation rather than lateral displacement. Unlike the findings of Thiyyakkandi et al. (2016), where clear lateral failure and a softer torque-rotation response (peak at ~8°) were observed, the combined test in this study exhibited limited lateral displacement (~0.8 in) and reached peak torque at approximately 1.5° rotation. This behavior is likely associated with the shorter moment arm and the relatively stiffer soil conditions, combined with interface effects.

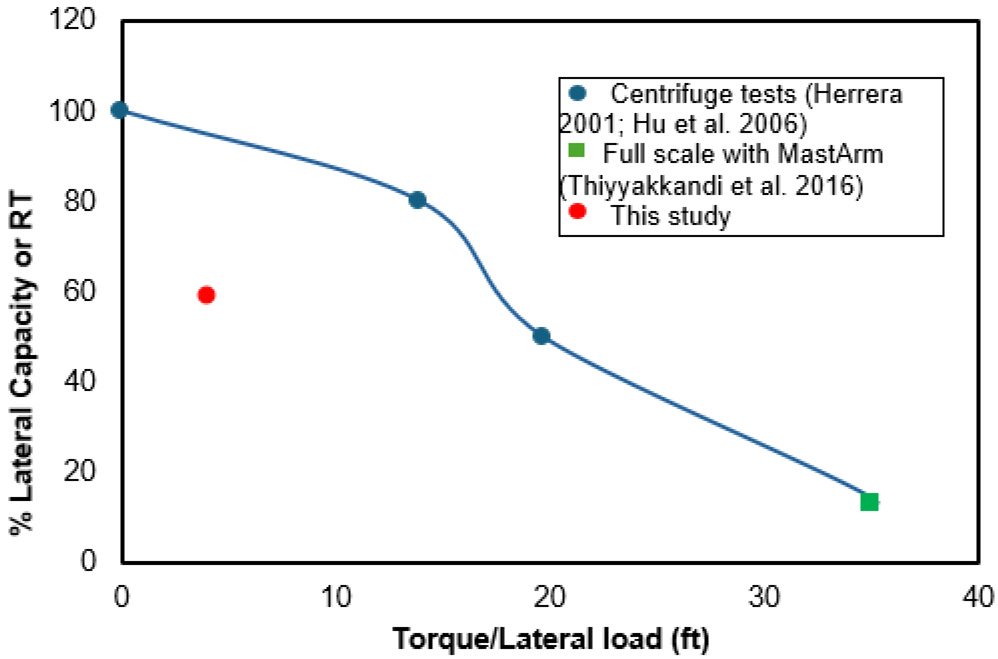

Figure 4-30. Lateral resistance reduction factor due to torsion.

Overall, the experimental results demonstrate that both loading sequence and load interaction significantly influence the response of drilled shafts. While ultimate capacities remain comparable in some cases, the mobilization pathways, small-strain stiffness characteristics, and governing failure mechanisms vary depending on prior loading history and the presence of load coupling. These findings highlight the importance of considering loading sequence and interaction effects when analyzing experimental data and evaluating drilled shaft performance under realistic loading scenarios.

4.5. Chapter Summary

Seven full-scale tests were conducted to evaluate the lateral, torsional, and combined lateral-torsional behavior of drilled shafts under controlled conditions. The results demonstrated that both loading sequence and load interaction significantly affected the mobilized response of the shaft-soil system. While ultimate capacities remained similar for several loading cases, substantial differences were observed in stiffness and resistance mobilization. The results further indicated that shaft installation procedures and interface conditions strongly influenced torsional behavior. These observations provide the experimental basis for the numerical best-fit estimation and interpretation presented in Chapter 5.

CHAPTER 5. Numerical Modeling and Best-Fit Estimation Analyses

This chapter presents the numerical model and best-fit estimation developed to reproduce the lateral and torsional response of a drilled shaft subjected to monotonic loading. The best-fit estimate was obtained from results of large-scale experimental testing conducted in a geotechnical chamber under controlled conditions. The primary objective of this process was to ensure that the numerical model accurately captured both the stiffness-dominated response at small deformations and the strength-controlled response at larger displacements.

Initial soil parameters were derived from in-situ and triaxial test data and semiempirical correlations. These parameters served as baseline inputs for the numerical model. Subsequent adjustments were made through a systematic best-fit estimate process to account for construction effects and mobilized soil-structure interaction mechanisms. The best-fit analysis was conducted separately for Phase I and Phase II of the experimental program to reflect differences in construction processes and confinement conditions.

To isolate governing mechanisms and avoid masking individual effects, purely lateral and purely torsional loading cases were best-fit approximated independently prior to evaluating sequential or combined loading conditions. This approach enables a clearer interpretation of parameter influence and provides a consistent baseline for subsequent coupled analyses.

5.1. Role of Soil Parameters in Lateral and Torsional Response

The best-fit estimated model of the soil-structure interaction was performed by explicitly linking each soil parameter to the physical mechanisms governing the lateral (p-y) and torsional (T-θ) responses of the drilled shaft. Rather than adjusting parameters simultaneously, a best-fit estimate was carried out by identifying which parameters predominantly influence specific regions of the response curves and modifying them in a manner consistent with established soil mechanics principles.

For lateral loading, the p-y curve (as shown in **Figure 5-1**) may be divided into an initial linear segment corresponding to small-strain soil behavior (Reese et al. 1974), a nonlinear transition region associated with progressive mobilization of shear resistance, and an ultimate plateau governed by soil failure mechanisms. Similarly, the T-θ curve for torsional loading consists of an initial linear stiffness-controlled segment, followed by nonlinear softening, and finally an ultimate torsional resistance governed by interface and soil failure.

Understanding the role of each parameter in shaping these curve segments is essential to ensure that the best-fit estimate reflects the physical soil behavior rather than numerical curve fitting.

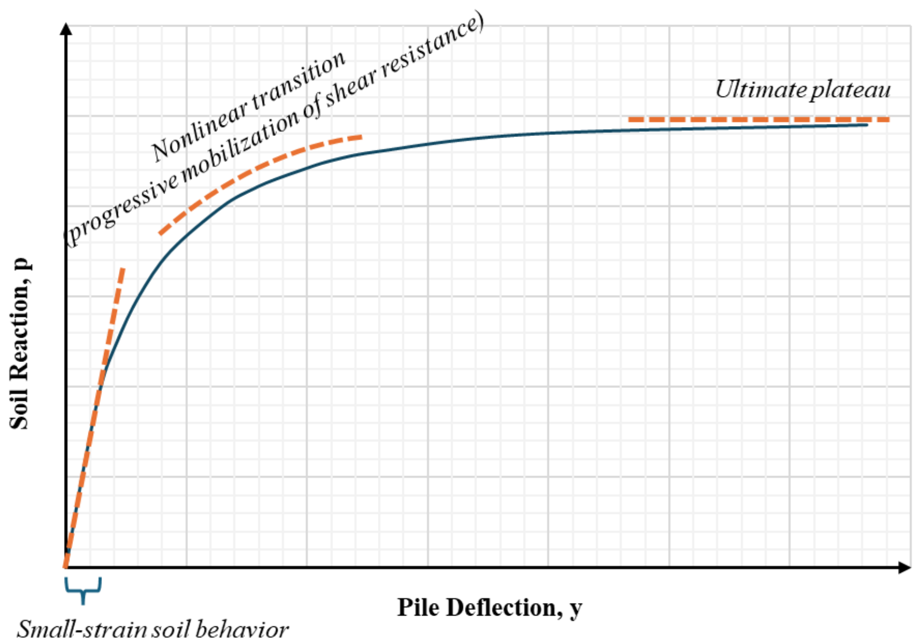

Figure 5-1. P-y curve segments

5.2. Best-Fit Estimation Strategy and Parameter Influence

The best-fit approximation strategy followed a sequential and mechanism-based approach. Parameters controlling small-strain stiffness were best-fitted first to match the initial linear portions of the p-y and T-θ curves. Parameters governing nonlinear behavior and ultimate resistance were subsequently adjusted to reproduce the observed curvature and asymptotic response. This approach ensures that stiffness-related parameters are not used to artificially compensate for strength-related discrepancies, and vice versa.

The soil parameters considered in the best-fit analysis in FB-MultiPier include the internal friction angle (ϕ), total unit weight (γ), coefficient of horizontal subgrade reaction (k), shear modulus (G), and torsional shear stress (τ). The internal friction angle and unit weight were considered from the CPT, SPT, triaxial testing, and sand cone results presented in 3.1, while the remaining parameters were evaluated using empirical and semi-empirical relationships and refined through best-fit estimation.

5.3. Influence of Individual Parameters

5.3.1. Internal Friction Angle, ϕ

The internal friction angle governs the ultimate lateral resistance of the drilled shaft by controlling the magnitude of passive earth pressures mobilized in the surrounding soil. In p-y formulations, ϕ primarily affects the asymptotic portion of the p-y curve, corresponding to large lateral displacements where soil failure mechanisms dominate.

While the intrinsic friction angle is a material property, the mobilized friction angle depends on density, confinement, and stress path. In the present study, the high density achieved within the geotechnical chamber and the associated lateral confinement may result in mobilized ultimate friction angles that are equal to or higher than laboratory-derived values. Consequently, variations in ϕ during best-fit approximation are interpreted as adjustments to the mobilized strength level rather than changes in soil type.

5.3.2. Unit Weight, γ

The total unit weight influences both lateral and torsional responses by controlling the effective vertical stress with depth. For lateral loading, γ contributes to the magnitude of passive resistance and therefore affects the ultimate value of the p-y curve. In torsional loading, unit weight affects the normal stress acting along the shaft-soil interface, which in turn governs the ultimate shear resistance.

In the geotechnical chamber, confinement and placement procedures may partially densify the sand, increasing its unit weight relative to free-field conditions. Adjustments to γ account for these density-related effects and their influence on stress distribution around the shaft.

5.3.3. Shear Modulus, G

The shear modulus controls the initial torsional stiffness and the small-rotation segment of the T-θ response. In granular soils, G is highly dependent on density, stress level, and soil fabric. Dense sands develop interlocked particle contacts and persistent force chains, resulting in higher stiffness and pronounced dilative behavior under shear.

In the present best-fit estimation, reductions in G are interpreted as reflecting construction disturbance, interface effects, or differences in stress path between laboratory specimens and the modeled system.

5.3.4. Coefficient of Horizontal Subgrade Reaction, k

The coefficient of horizontal subgrade reaction controls the initial linear portion of the p-y curve and represents the soil response under small lateral deflections. Physically, k reflects the small-strain stiffness of the soil mass surrounding the shaft. In cohesionless soils, k increases with depth due to increasing effective stress and confinement.

Because the initial straight segment of the p-y curve applies only at very small deflections, variations in k primarily influence model predictions under low lateral loads and have minimal effect on ultimate capacity. Accordingly, k is approximated to match the initial slope of the p-y response without affecting the nonlinear or failure regions.

5.3.5. Torsional Shear Stress, τ

The torsional shear stress parameter controls the nonlinear transition and ultimate capacity of the T-θ curve. This parameter represents the limiting shear resistance mobilized along the shaft-soil interface and is influenced by normal stress, relative density, and interface conditions.

Variations in τ during best-fit estimate were used to capture the observed ultimate torsional resistance, accounting for potential enhancement of interface strength due to confinement within the chamber, as well as possible degradation mechanisms under combined lateral and torsional loading.

5.4. Parameter-to-Curve Influence Summary

The relationship between soil parameters and the characteristic regions of the p-y and T-θ curves is summarized conceptually in **Figure 5-2**. This framework guided the best-fit estimation process and ensured that each parameter adjustment was physically justified.

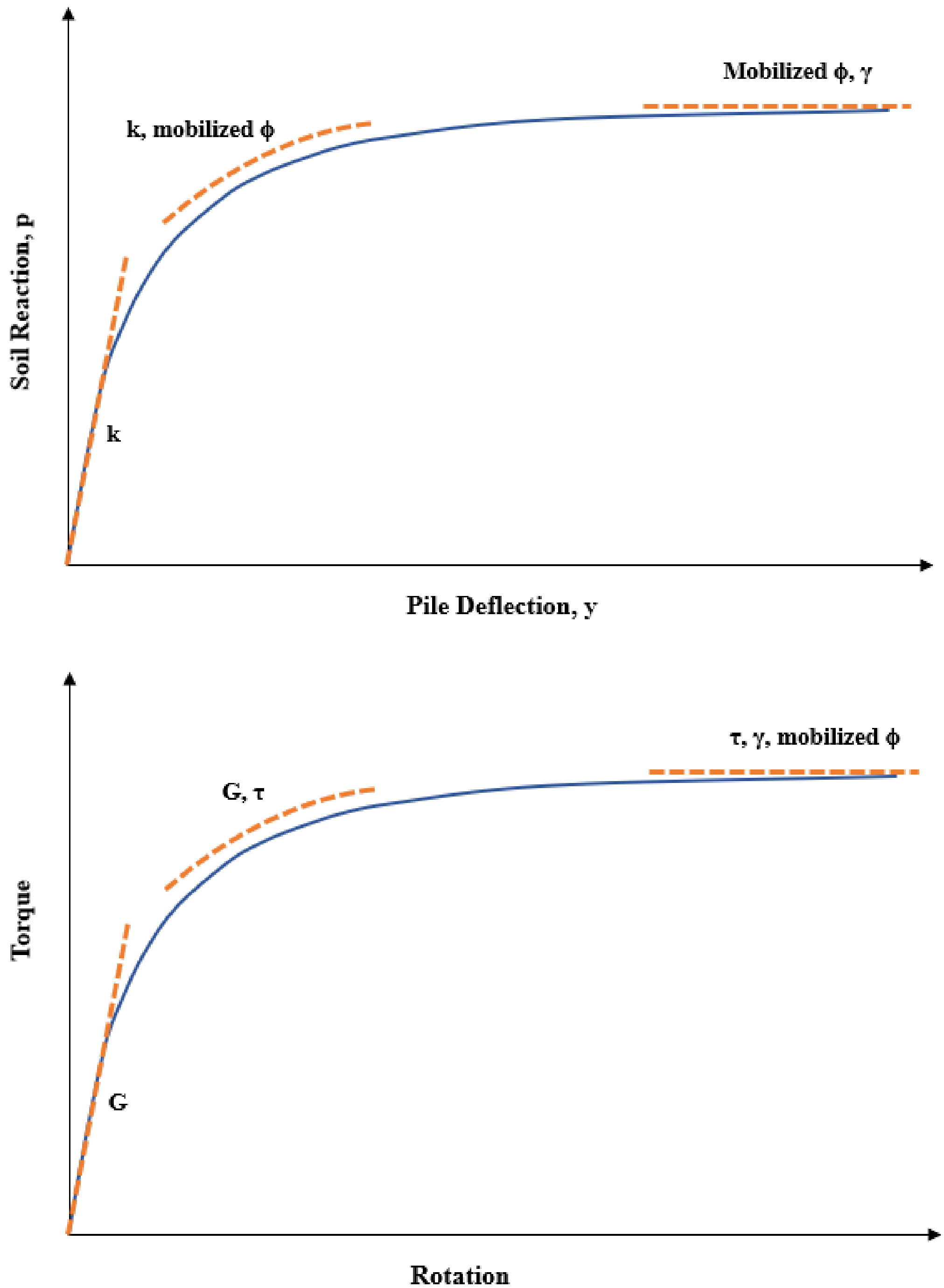

Figure 5-2. Parameter-to-curve influence for p-y and T-θ plots.

5.5. Initial Parameter Estimation for Phase I and Phase II Load Testing

The soil properties used to model the Phase I and Phase II load tests, including unit weight and internal friction angle, were obtained from laboratory and in situ testing. However, the construction of the drilled shafts was expected to modify the stiffness characteristics of the surrounding soil. Therefore, stiffness-related parameters, such as the shear modulus and the coefficient of horizontal subgrade reaction, were initially estimated using empirical correlations commonly used in geotechnical practice and subsequently refined via a best-fit model approximation.

The shear modulus was calculated using the principles of linear elasticity (Equation 16). The Young's modulus values for both testing phases were selected based on the recommendations of Samtani and Nowatzki (2006), who reported a typical range of 4.7 ksi to 7.8 ksi for medium-dense sands. For Phase II, the lower bound of this range was adopted to account for the lower dry unit weight measured during the sand cone tests. The values of the soil modulus computed from in-situ tests (presented in **Table 3-1**) were merely considered as a reference for the possible maximum values for the undisturbed soil.

The coefficient of horizontal subgrade reaction was estimated using empirical relationships that relate soil stiffness to pile diameter and elastic modulus. Following the recommendations of the FB-MultiPier Manual (citing FHWA, 1993), the parameter was constrained within a range of 25 to 225 pci, corresponding approximately to loose and dense sand conditions. These initial estimates provided a rational basis for the model and ensured consistency between stiffness-related parameters and the density state of the sand within the geotechnical chamber.

The torsional side-shear parameters were initially estimated using the β-method, which relates interface shear resistance to the effective normal stress. This approach was selected based on the evaluation of side-shear resistance prediction methods reported by Aguilar (2018), who found that the β-method provided the best agreement with measured torsional shear resistance for drilled shafts.

Table 5-1 presents three sets of soil parameters considered during model development. The first column summarizes soil properties reported by Okafor (2024) and represents laboratory and in-situ measurements obtained from the M&M sand used in the geotechnical chamber. These values served as reference soil properties but were not directly used in the numerical models. The second and third columns present the initial parameter sets adopted for the Phase I and Phase II numerical models, respectively. These values were derived from laboratory and in-situ testing results, empirical correlations, and the measured density conditions associated with each testing phase. The Phase II initial estimates differ from those of Phase I primarily because recompaction testing indicated lower dry unit weight conditions. These parameter sets served as the starting point for the subsequent best-fit estimation procedure.

Table 5-1. Initial set of parameters for Phase I and Phase II of testing

	M&M Sand (Okafor 2024)	First set of tests Phase I In-situ and Loehr (2025)	Second set of tests Phase II
γ (pcf)	107.7	111	100
ϕ (deg)	41.5	45	41.5
ν	0.25	0.25	0.25

	M&M Sand (Okafor 2024)	First set of tests Phase I	Second set of tests Phase II
		In-situ and Loehr (2025)	
E_{50} (ksi)	5.2	6.1	4.7
G (ksi)	2.0	2.5	1.9
k (pci)	190.4	182	139
τ (psf)*	431	680	600

* Calculated using β method and mid shaft length

5.6. Best-fit Parameter Estimation Results

The best-fit parameter estimation are presented separately for purely torsional, purely lateral, and sequential loading cases for Phase I and Phase II. This separation was intentionally adopted to isolate the governing mechanisms associated with each loading mode and to ensure that stiffness and strength related parameters were approximated independently. Combined loading effects are therefore interpreted relative to well-defined baseline lateral and torsional responses.

Although individual best-fit parameter sets were developed for each test configuration, an alternative modeling strategy would be to identify a single representative parameter set capable of approximating the response of all tests. Such an approach would improve predictive capability and reduce the need for test-specific parameter adjustments. However, the objective of the present study was to identify how construction effects, loading sequence, and load interaction influenced the apparent mobilized parameters; therefore, separate best-fit parameter sets were adopted for each loading condition.

Phase I

5.6.1. Purely Torsional Response - Phase I

The best-fit parameter estimation of the purely torsional response in Phase I required a reduction of the initial shear modulus to approximately 0.5 ksi and an increase in the torsional shear stress to approximately 1100 psf. The reduction in shear modulus reflects the influence of construction-induced disturbance and stress relief associated with shaft excavation, which reduces the effective stiffness of the shaft-soil interface relative to intact in-situ conditions.

These adjustments allowed the numerical model to accurately reproduce both the initial stiffness and the ultimate torque observed experimentally (**Figure 5-3**).

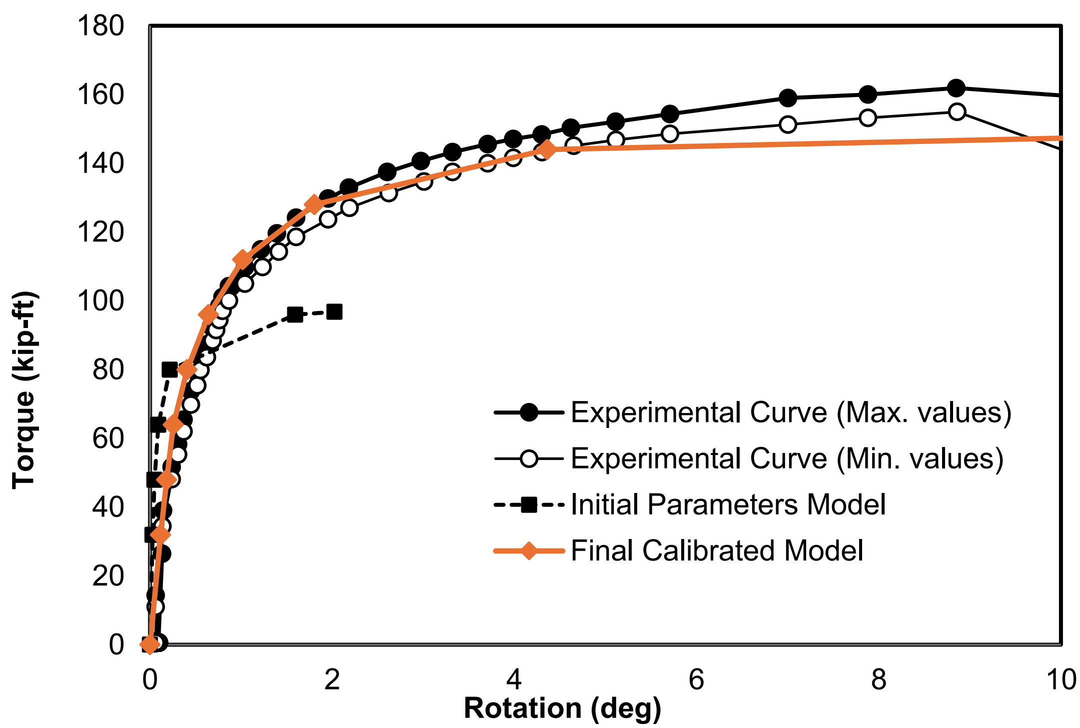

Figure 5-3. Torque vs. Rotation of Purely Torsional Load Test Phase I

5.6.2. Lateral Loading Following Purely Torsional Loading – Phase I

For the lateral response following torsional loading in Phase I, the parameters controlling lateral resistance were increased relative to their initial estimates to account for the stiffer response observed during testing. The modulus of horizontal subgrade reaction, *k*, was increased by approximately 20%, which improved the fit of the initial slope of the load-displacement curve, corresponding to the linear elastic portion of the response and indicating greater mobilized lateral stiffness. Modest increases of approximately 10% in the soil unit weight and mobilized internal friction angle were also implemented. These parameters primarily influenced the nonlinear and ultimate portions of the *p*-*y* response, resulting in improved agreement between the numerical predictions and the experimental measurements, as shown in **Figure 5-4**. The increase in lateral resistance parameters following torsional loading can be attributed to densification and particle rearrangement of the surrounding sand, which enhanced the mobilized soil stiffness and strength around the shaft.

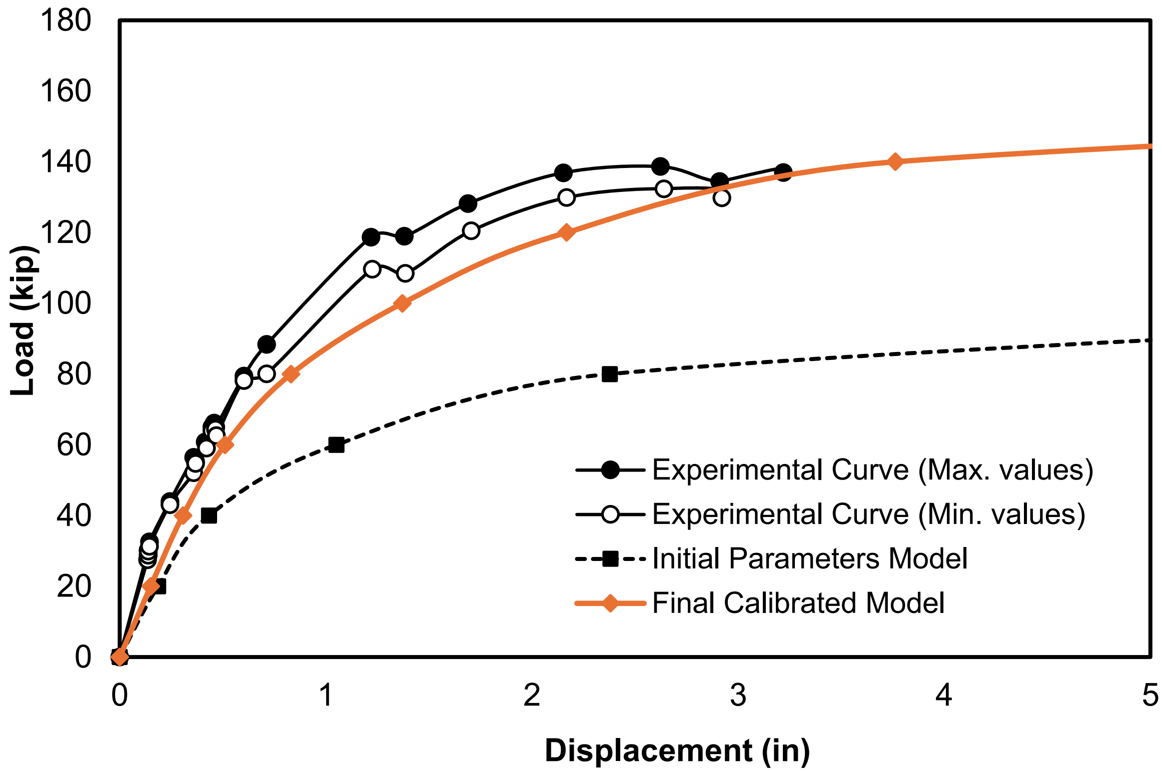

Figure 5-4. Load vs. Displacement of Lateral Load Test after Purely Torsional Test Phase I

5.6.3. Combined Lateral-Torsional Response – Phase I

The best-fit approximation of the combined lateral-torsional response in Phase I required adjustments to all model parameters relative to the values adopted in the isolated torsional and lateral loading analyses. The parameters governing lateral resistance, namely unit weight and internal friction angle, were reduced by approximately 5% and 10%, respectively. In contrast, the modulus of horizontal subgrade reaction was increased by 20%, consistent with the best-fit estimation of the lateral response following torsional loading. The most significant adjustment was applied to the shear modulus, which was reduced to approximately 10% of its initial value to reproduce the initial linear portion of the measured torque-rotation response.

This substantial reduction in the best-fit shear modulus value indicates that the stiffness mobilized under combined loading was significantly lower than that inferred from the isolated torsional loading case, for which the fitted shear modulus was approximately twice the value required to reproduce the combined response. The reduced stiffness may reflect the combined effects of construction-induced disturbance, nonlinear soil behavior, and the interaction between lateral displacement and torsional loading, which can alter stress redistribution and stiffness mobilization within the surrounding soil. In this context, the best-fit shear modulus should be interpreted as an equivalent modeling parameter representing the overall soil response under combined loading rather than a direct measure of the in-situ small-strain shear modulus. The final model successfully reproduced both the reduced initial stiffness and the observed nonlinear torque-rotation behavior, as shown in **Figure 5-5** and **Figure 5-6**.

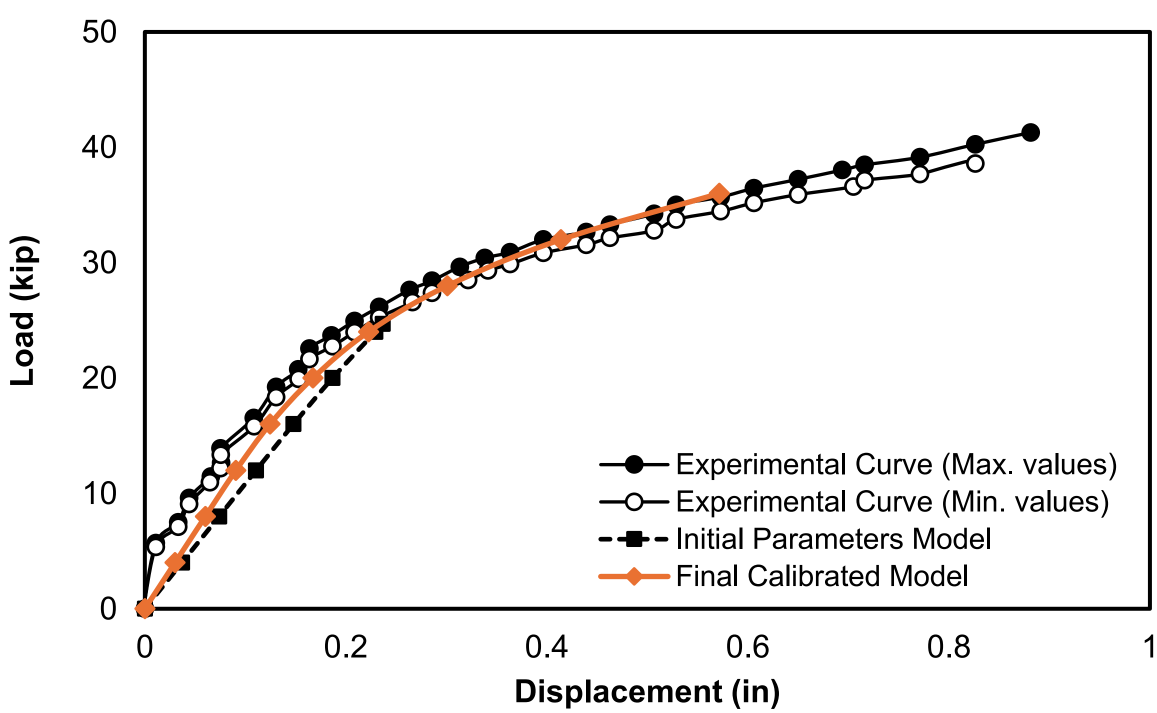

Figure 5-5. Load vs. Displacement of Combined (Lateral-Torsional) Load Test Phase I

The pronounced reduction in shear modulus observed under combined lateral-torsional loading in Phase I highlights the sensitivity of mobilized torsional stiffness to multidirectional shearing when interface conditions are affected by construction disturbance.

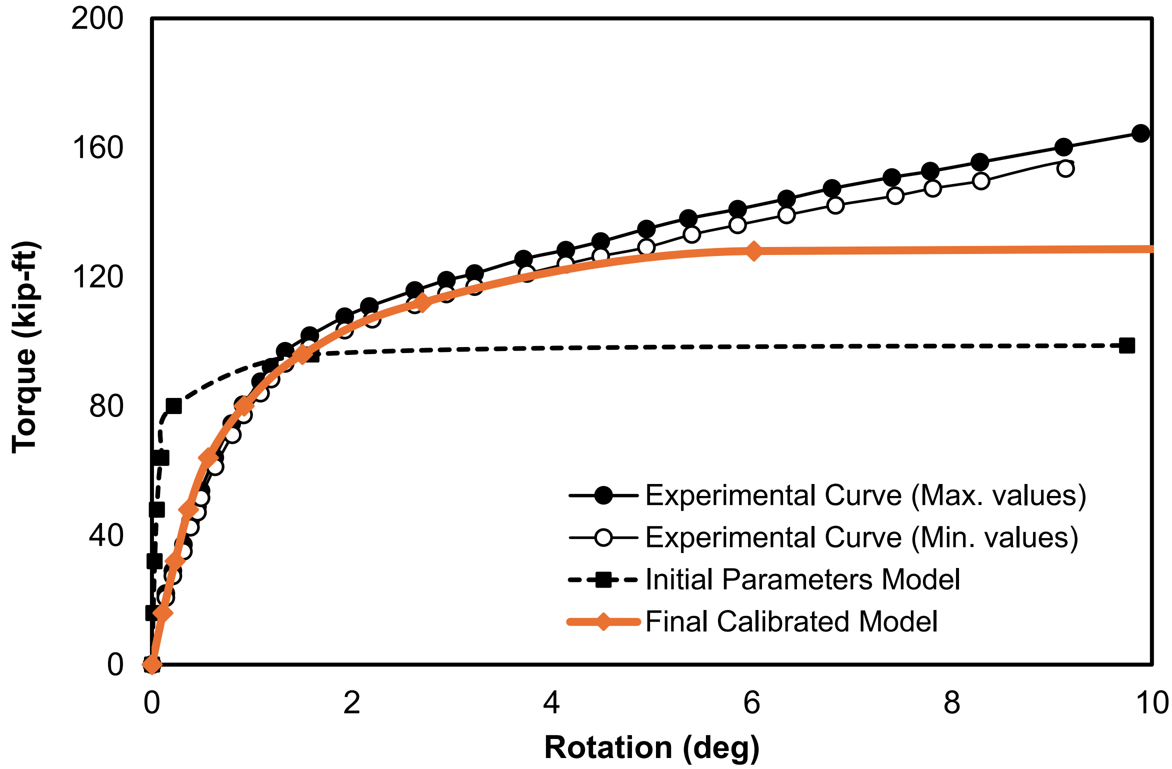

Figure 5-6. Torque vs. Rotation of Combined (Lateral-Torsional) Load Test Phase I

5.6.4. Lateral Loading Following Combined (Lateral-Torsional) Response – Phase I

For the lateral response following the combined loading test in Phase I, parameters governing lateral resistance were increased by approximately 10% relative to their initial values, consistent with the adjustments made for the lateral loading test conducted after the purely torsional test in Phase I.

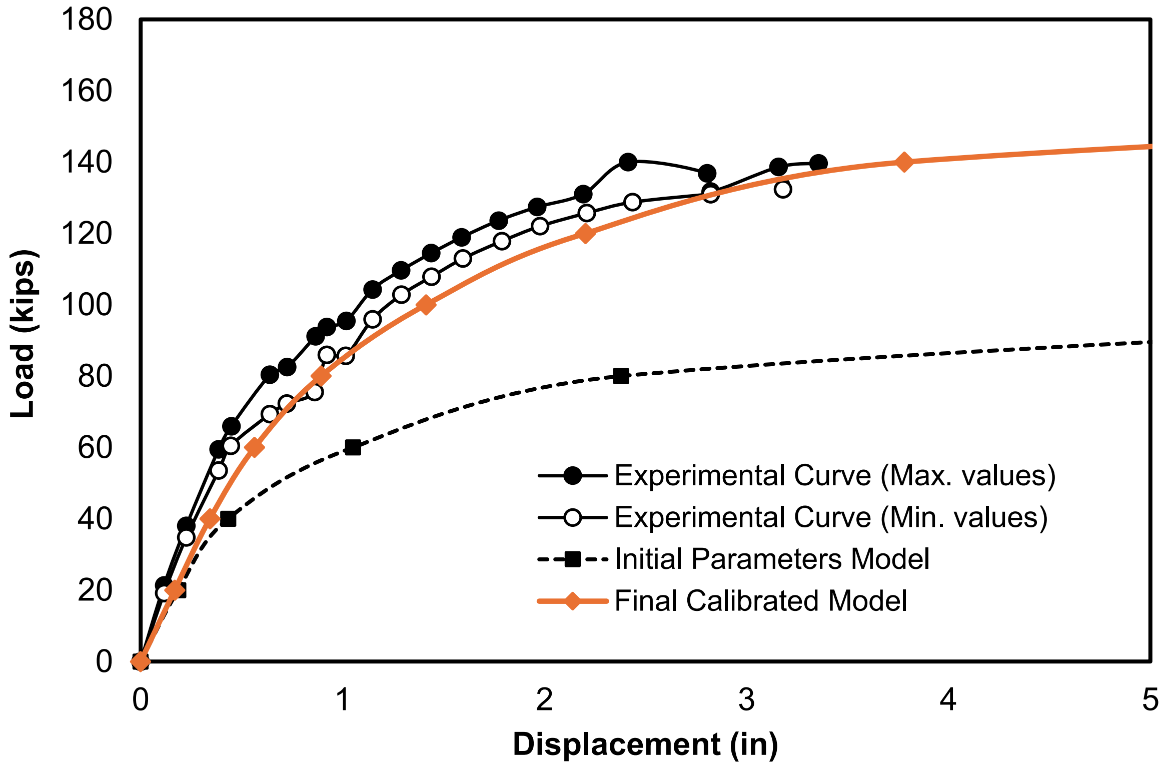

Figure 5-7. Load vs. Displacement of Lateral Load Test after Combined Test Phase I

Phase II

5.6.5. Purely Lateral Response – Phase II

The best-fit estimate of the purely lateral response in Phase II required adjustments to the parameters similar to those in Phase I. The unit weight was increased by approximately 20%, the mobilized internal friction angle by 10%, while the modulus of horizontal subgrade reaction was not increased, as shown in **Figure 5-8**.

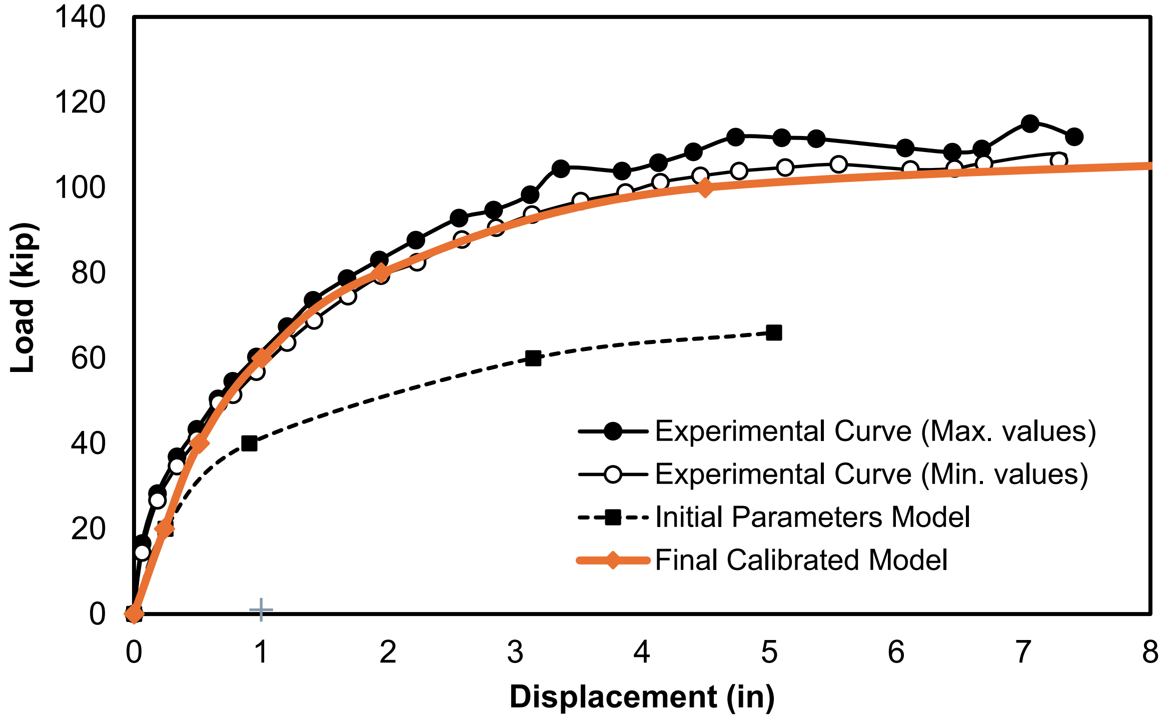

Figure 5-8. Load vs. Displacement of Purely Lateral Load Test Phase II

5.6.6. Purely Torsional Response – Phase II

The best-fit estimate of the purely torsional response in Phase II required only an adjustment to the torsional shear resistance. The torsional side-shear strength parameter was increased by a factor of 1.8 from its initial estimate, resulting in a resistance of approximately 1,100 psf. This value is consistent with the torsional shear resistance required to reproduce the measured response in the Phase I torsional load tests, suggesting similar shaft-soil interface behavior between the two testing phases despite differences in the measured soil density. The best-fitted model provided a satisfactory representation of the measured torque-rotation response, indicating that the initial stiffness and ultimate torsional resistance were primarily governed by the mobilized shaft-soil interface shear strength (**Figure 5-9**).

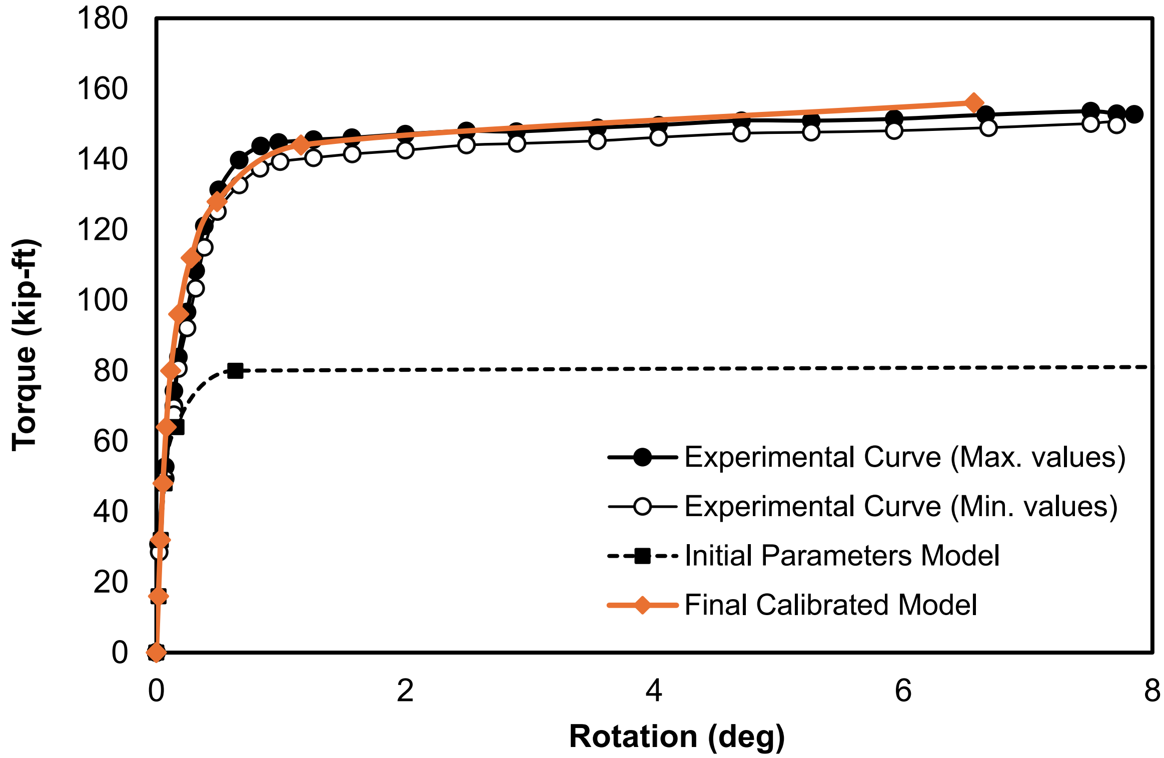

Figure 5-9. Torque vs. Rotation of Purely Torsional Load Test Phase II

5.6.7. Lateral Loading Following Purely Torsional Loading – Phase II

The lateral response following purely torsional loading in Phase II exhibited trends similar to those observed in Phase I. To achieve improved agreement with the measured response, the soil unit weight and mobilized internal friction angle were increased by approximately 10%. These adjustments primarily influenced the nonlinear and ultimate portions of the *p-y* response, resulting in a closer match between the numerical predictions and the experimental data. Similar to the best-fit estimate of the pure lateral load test in Phase II, no adjustment to the modulus of horizontal subgrade reaction was required, indicating that the initial estimate provided an adequate representation of the mobilized lateral stiffness. The best-fit model successfully reproduced both the initial and nonlinear portions of the load-displacement response, as shown in **Figure 5-10**.

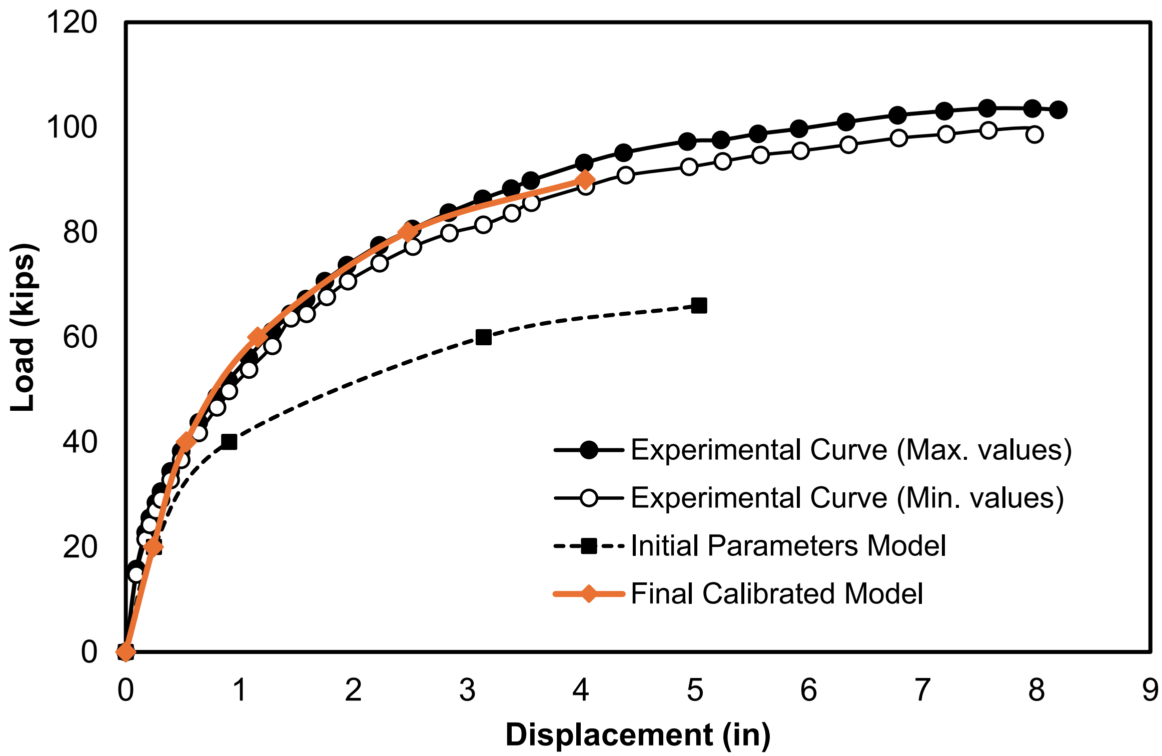

Figure 5-10 Load vs. Displacement of Lateral Load Test after Pure Torsional Test Phase II

Comparison of identical loading cases across Phase I and Phase II highlights the influence of construction effects and stress history in addition to soil density. Although the sand in Phase II exhibited a lower density than that in Phase I, the best-fitted estimated responses suggest that factors related to shaft installation and soil-structure interaction also played a significant role in controlling the mobilized behavior.

An important distinction between the two testing phases is the method of drilled shaft installation and the resulting shaft-soil interface conditions. In Phase I, the shafts were constructed by excavating the soil and placing concrete. This process inherently induces stress relief and disturbance in the surrounding soil mass, resulting in localized loosening and imperfect contact along the shaft-soil interface. In contrast, the shafts used in Phase II had been previously constructed during Phase I, subsequently exhumed, and reinstalled in the geotechnical chamber. The surrounding sand was then placed and compacted around the shafts, resulting in improved confinement and enhanced shaft-soil contact conditions.

These differences in installation procedures provide a mechanistic explanation for the best-fit trends observed under both purely lateral and purely torsional loading. Despite the lower sand density in Phase II, the improved confinement and interface conditions resulted in greater mobilized torsional stiffness and resistance compared to Phase I. In contrast, the stress relief and soil disturbance associated with shaft excavation and concrete placement during Phase I likely contributed to reduced mobilized stiffness. This effect became particularly evident during the combined lateral-torsional loading tests, which were conducted exclusively in Phase I and required substantial reductions in the best-fit estimated stiffness parameters to reproduce the measured response. The results suggest that construction-induced changes in stress state and interface conditions can influence shaft behavior comparable to, or greater than, the influence of soil density alone.

5.7. Summary of Best-Fit Estimated Trends

The results from both testing phases revealed consistent trends regarding the influence of loading mode, construction effects, and loading sequence on the mobilized soil response. The summaries of the best-fit parameters and ratios (best-fit/initial values) are presented in **Table 5-2**, **Table 5-3**, and **Table 5-4**. The friction angle adjustments should not be interpreted as changes in the intrinsic soil strength. Rather, they represent equivalent mobilized strength parameters required for the FB-MultiPier model to reproduce the observed response under different loading histories and stress paths.

Table 5-2. Summary of the parameters used for the best-fit estimation of load test models of Phase I

	Initial Parameters	Purely Torsional	Multiplier (Ratio best-fit/initial)	Lateral after Torsional	Multiplier (Ratio best-fit/initial)	Combined	Multiplier (Ratio best-fit/initial)	Lateral after Combined	Multiplier (Ratio best-fit/initial)
γ (pcf)	**111**	111	**1**	122	**1.1**	106	**0.95**	122	**1.1**
ϕ (deg)	**45**	45		49.5	**1.1**	40.5	**0.9**	49.5	**1.1**
υ	**0.25**	0.25		0.25		0.25		0.25	
G (ksi)	**2.5**	0.5	**0.20**	2.5		0.25	**0.10**	2.5	
k (pci)	**182**	182		225	**1.2**	225	**1.2**	200	**1.1**
τ (psf)	**680**	1100	**1.6**	680		1000	**1.5**	680	

Table 5-3. Summary of the parameters used for the best-fit estimation of load test models of Phase II

	Initial Parameters	Purely Lateral	Multiplier (Ratio)	Purely Torsional	Multiplier (Ratio)	Lateral after Torsional	Multiplier (Ratio)
γ (pcf)	**100**	120	**1.2**	100	**1.0**	110	**1.1**
ϕ (deg)	**41.5**	45	**1.1**	41.5		45	**1.1**
υ	**0.25**	0.25		0.25		0.25	
G (ksi)	**1.9**	1.9		1.9	**1.0**	1.9	
k (pci)	**139**	139	**1.0**	139		139	**1.0**
τ (psf)	**600**	600		1100	**1.8**	600	

Table 5-4. Summary of ultimate torque and load values from numerical models and full-scale tests

		Numerical Model				Field Tests				Ratio (Field/Numerical)	
		Max Torque (kip-ft)	@ rotation (deg)	Max. Lat. Load (kip)	@Y Disp. (in)	Max Torque (kip-ft)	@ rotation (deg)	Max. Lat. Load (kip)	@Y Disp. (in)	Torque	Lateral Load
PHASE I	Pure Torsion A	144	4.36			143.6	4.62			**0.997**	
	Lateral after Torsion A			132.4	2.64			138.64	2.6		**1.047**
	Combined (4ft eccent.)	128	5.02	36	0.68	134.84	4.94	38.03	0.69	**1.053**	**1.056**
	Lateral after Combined A			133.9	2.8			136.8	2.8		**1.022**
PHASE II	Pure Lateral B			100	4.12			105.81	4.13		**1.058**
	Pure Torsion B	144	4.7			144.4	4.7			**1.003**	
	Lateral after Torsion B			92.4	4.95			97.3	4.93		**1.053**

5.7.1. Influence of Construction on Torsional Stiffness

The most significant best-fit adjustments were associated with the shear modulus used to reproduce torsional behavior. For the Phase I torsional tests, the approximated shear modulus was substantially lower than the value estimated from laboratory and in-situ testing. This reduction is attributed to stress relief, soil disturbance, and reduced confinement resulting from shaft excavation and concrete placement.

In contrast, the torsional response of Phase II exhibited substantially greater initial stiffness despite the lower density of the recompacted soil. This behavior suggests that shaft-soil interface conditions and confinement effects had a greater influence on torsional stiffness than relative density alone. The improved soil contact achieved during recompaction allowed mobilization of significant torsional resistance at small rotations.

5.7.2. Influence of Combined Lateral-Torsional Loading

Combined loading required the largest overall deviation from the baseline best-fit parameters. Unlike the isolated loading cases, the combined lateral-torsional loading required reductions in the equivalent model parameters associated with strength and stiffness. While changes in shear modulus can be linked to altered stiffness mobilization under multidirectional loading, adjustments to unit weight and friction angle should be interpreted as effective fitting parameters within the FB-MultiPier framework rather than actual changes in soil properties.

The pronounced reduction in the estimated shear modulus further suggests that the mobilized torsional stiffness under combined loading was significantly lower than that observed during purely torsional loading. This finding supports previous research indicating that lateral displacement negatively influences torsional stiffness and resistance mobilization.

5.7.3. Influence of Prior Loading on Lateral Response

For both phases, the lateral response following torsional loading required increased values of mobilized unit weight and internal friction angle relative to the initial estimates. These adjustments suggest that prior torsional loading produced localized densification and particle rearrangement, resulting in enhanced lateral resistance.

However, the estimated strength parameters required for post-torsional loading cases remained slightly lower than those associated with isolated lateral loading, indicating that previous loading altered the soil structure and limited the full mobilization of lateral resistance.

5.7.4. Variability of the Horizontal Subgrade Reaction

The coefficient of horizontal subgrade reaction exhibited different trends between phases. In Phase I, moderate increases in the best-fit estimated values were required to reproduce the observed initial lateral stiffness. In Phase II, satisfactory agreement with the measured response was generally achieved without modifying the initial estimates.

These observations suggest that the influence of the subgrade reaction coefficient is strongly linked to confinement conditions and construction effects and should not be treated as a constant material property.

5.7.5. Overall Modeling Observations

The best-fit estimation results indicate that stiffness-related parameters were more sensitive to loading history and construction effects than strength-related parameters. The results also demonstrate that lateral and torsional resistance cannot be considered independent mechanisms. Loading sequence, interface conditions, and multidirectional stress paths significantly influenced the mobilized foundation response and should be considered in the analysis and design of drilled shafts supporting mast arm structures.

Given the limited set of experimental tests, the objective of the numerical modeling effort was not to establish a unique, calibrated parameter set representative of the sand deposit, but rather to identify equivalent parameter combinations that reproduce the measured responses of individual experiments. Consequently, the resulting parameter sets should be interpreted as best-fit estimates of mobilized behavior under specific loading histories, installation conditions, and boundary effects rather than as direct measurements of intrinsic soil properties.

Examination of the best-fit trends suggests that a common set of soil strength parameters could potentially reproduce most test responses with reasonable accuracy. In particular, unit weights near 110 pcf and friction angles near 45° generally fall within the range required to approximate multiple loading conditions. Future work should investigate the use of a single physically defensible parameter set for all tests while allowing stiffness-related parameters, such as shear modulus and horizontal subgrade reaction, to vary in response to construction effects, confinement conditions, and loading history. Such an approach would provide a more traditional calibration framework and improve the generality of the numerical models.

CHAPTER 6. Conclusions

Seven load tests were conducted on two drilled shafts in two phases of testing in the Auburn University Geotechnical Chamber. This study represents the first full-scale experimental investigation of relatively short-drilled shafts (typical of mast arm foundations) subjected to coupled and uncoupled lateral and torsional loading under controlled laboratory conditions.

The experimental program enabled direct evaluation of torsional mobilization mechanisms and interaction effects between torsion and lateral loading. The results provide insight into the governing role of shaft-soil interface conditions and the implications of load coupling on drilled shaft performance.

6.1. Summary of Key Findings

6.1.1. Experimental Findings

- Torsional behavior was governed primarily by the shaft-soil interface. Construction-induced disturbance in drilled and cast-in-place shafts resulted in reduced initial interface stiffness and more gradual mobilization of torsional resistance.
- Pure torsional loading produced a nonlinear torque-rotation response characterized by rapid initial mobilization of resistance followed by progressive stiffness degradation up to ultimate capacity.
- Lateral load responses measured after pure torsional failure and after combined loading were generally similar, indicating that ultimate lateral capacity is primarily

governed by the surrounding soil mass. However, under combined loading, failure was dominated by rotational mechanisms.

- Despite similar overall response envelopes, the lateral test conducted after combined loading exhibited reduced stiffness beyond approximately 0.75 in., indicating degradation of the shaft-soil interface following coupled rotational deformation.
- Following exhumation and recompaction, the shaft exhibited a significantly stiffer torsional response, with near-complete mobilization of torsional capacity at very small rotations. This highlights the importance of interface quality, confinement, and shaft-soil contact.
- Under combined lateral-torsional loading, torsional stiffness was reduced, and larger rotations were required to mobilize torque comparable to pure torsion, indicating stress redistribution along the shaft-soil interface due to concurrent lateral deformation.
- Lateral loading following torsional loading failure resulted in reduced lateral stiffness and lower initial lateral resistance compared to pure lateral loading; however, differences in ultimate capacity diminished at larger displacements.

6.1.2. Numerical Modeling Findings

- FB-MultiPier successfully reproduced the measured lateral and torsional responses of the tested drilled shafts through the best-fit estimation of a limited set of physically meaningful soil parameters.
- A mechanism-based approach proved effective for separating stiffness and strength effects. The modulus of horizontal subgrade reaction and shear modulus

primarily controlled the initial portions of the p-y and T-θ responses, while unit weight, friction angle, and torsional shear resistance controlled the nonlinear and ultimate responses.

- Torsional response was highly sensitive to shaft-soil interface conditions. Similar ultimate torsional capacities were observed in both phases; however, large differences in initial stiffness demonstrated the importance of construction effects and confinement conditions.
- The β method underestimated the torsional shear resistance required to reproduce the measured torque-rotation responses in both testing phases.
- The shear modulus was the most sensitive parameter in the numerical analyses. Significant reductions were required to reproduce the measured torsional response, particularly under combined loading conditions, indicating that mobilized torsional stiffness is strongly affected by stress path and loading interaction.
- Combined lateral-torsional loading produced responses that could not be adequately represented using best-fitted parameters from isolated loading cases. Additional reductions in stiffness and strength parameters were necessary, demonstrating that coupled loading modifies soil behavior and strength mobilization mechanisms.
- Construction-induced disturbance associated with excavation and concrete placement significantly affected the mobilized stiffness of the shaft-soil system. The observed differences between Phase I and Phase II highlight the importance

of considering installation effects when selecting soil parameters for numerical modeling.

- The best-fit estimated models provide a benchmark dataset for future studies involving combined lateral-torsional loading of drilled shafts and support the development of improved design methodologies that account for loading interaction and construction effects.

6.2. Conclusions

- The results demonstrate that lateral and torsional loading are inherently coupled, with loading sequence influencing stiffness, resistance mobilization, and governing failure mechanisms. Under combined loading, torsional stiffness decreased, and larger rotations were required to mobilize resistance than under pure torsion, indicating a redistribution of stresses along the shaft-soil interface. While the ultimate lateral capacity remained largely controlled by the surrounding soil mass, prior torsional loading reduced lateral stiffness and delayed the mobilization of resistance.
- The results confirm that the torsional behavior of drilled shafts is governed primarily by shaft-soil interface conditions and is sensitive to installation method. Shafts constructed using conventional drilling and casting exhibited reduced initial torsional stiffness and more gradual resistance mobilization due to construction-induced disturbance at the interface. In contrast, shafts subjected to exhumation and re-compaction demonstrated significantly higher initial stiffness and near-complete mobilization of torsional capacity at small rotations, reflecting improved confinement and interface contact. These findings highlight the critical

role of interface quality in controlling the torsional response, while indicating that ultimate capacity is less sensitive to installation effects than stiffness.

- Multidirectional loading altered stress redistribution and reduced the mobilized torsional stiffness around the shaft. The combined lateral-torsional loading case required the largest deviations from the initial parameter estimates and could not be adequately reproduced using parameter sets derived from isolated lateral or torsional loading conditions. These results indicate that coupled loading influences the mechanisms governing stiffness and resistance mobilization and should not be represented solely through superposition of independent lateral and torsional responses.
- The best-fit trends were generally consistent between phases and demonstrated that shaft-soil interface conditions, confinement, and loading sequence had a greater influence on mobilized stiffness than density alone. This conclusion is supported by the higher torsional stiffness observed in Phase II despite the lower density of the recompacted sand.
- Although one of the initial objectives of this research was to investigate the development of a design-oriented correlation for combined lateral-torsional loading, the limited number of combined full-scale tests and the specific geometry considered in this study do not support the development of a generalized design factor applicable to all drilled shaft foundations in sands. Nevertheless, the results clearly identify the governing mechanisms, influential parameters, and behavioral trends associated with coupled loading. These findings provide a valuable experimental database and a foundation for future

studies aimed at developing design correlations and reduction factors applicable to mast arm foundations under combined loading conditions.

6.3. Engineering Implications

The results of this study provide the following several practical observations relevant to the design and analysis of drilled shaft foundations supporting mast arm structures.

- Coupled lateral-torsional loading should be considered when significant torsional demands are present: The experimental and numerical results demonstrated that combined loading altered the mobilization of torsional resistance and reduced the initial torsional stiffness relative to purely torsional loading. Consequently, analyses that consider lateral and torsional components independently may not fully represent actual foundation behavior.
- Construction effects can significantly influence mobilized foundation stiffness: Soil parameters derived from laboratory and in-situ testing performed prior to shaft installation may not accurately reflect post-construction conditions. Excavation, concrete placement, and changes in confinement can modify the mobilized stiffness of the shaft-soil system.
- Ultimate capacity and stiffness should be evaluated separately: While several loading configurations produced similar ultimate capacities, substantial differences were observed in the initial stiffness and resistance mobilization pathways. Therefore, stiffness-based evaluations may provide additional insight into foundation performance beyond ultimate capacity alone.

- Loading history should be considered in performance assessments: Prior torsional loading altered the subsequent lateral response and reduced mobilized stiffness. This observation indicates that loading sequence may influence foundation performance under extreme loading events where multiple load components act simultaneously.

6.4. Limitations of the Study

Although the full-scale experimental program provides a valuable dataset for evaluating drilled shafts under lateral, torsional, and combined loading, the results should be interpreted with consideration of several experimental and modeling limitations. These limitations do not invalidate the findings; rather, they define the range of conditions represented by the study and identify areas where additional investigation is needed. Acknowledging these sources of uncertainty is important for interpreting the experimental observations and for guiding future research efforts.

6.4.1. Experimental Limitations

- The full-scale tests were conducted within a controlled geotechnical chamber rather than under natural field conditions. Although the chamber provided repeatable and well-characterized soil conditions, the finite chamber dimensions may have influenced soil deformation patterns at large displacements. As lateral displacement increased, portions of the mobilized soil mass approached the chamber boundaries, potentially increasing confinement compared to an infinite soil medium.
- The drilled shafts were constructed and tested within a controlled laboratory environment. Although the construction procedures were designed to replicate

field practices, factors such as groundwater conditions, natural soil variability, weather effects, and large-scale field construction tolerances were not represented.

- The testing program was limited to two drilled shafts and seven load tests. Although these tests provided a unique full-scale experimental database, the sample size limits the statistical evaluation of variability associated with soil conditions, construction practices, and material properties.
- The study focused on a single shaft geometry, embedment depth, and soil type. Consequently, the conclusions are most directly applicable to relatively short drilled shafts constructed in dense granular soils similar to those used in the geotechnical chamber.
- Combined lateral-torsional loading was evaluated through a single eccentric loading configuration. Different load eccentricities, shaft aspect ratios, and loading combinations may produce interaction mechanisms that differ from those observed in this study.
- Loading was monotonic and quasi-static. The effects of cyclic loading, repeated wind events, fatigue, and dynamic soil behavior were outside the scope of this investigation.
- The maximum lateral displacements reached during some tests exceeded serviceability limits that would typically govern practical mast arm foundation design. Therefore, the observed behavior at large displacements should primarily be interpreted as providing insight into failure mechanisms and the mobilization of resistance rather than as evidence of expected in-service performance.

6.4.2. Numerical Modeling Limitations

- FB-MultiPier utilizes a Beam-on-Winkler-Foundation formulation in which soil behavior is represented through independent nonlinear springs. Although computationally efficient, this approach does not explicitly model three-dimensional continuum soil behavior or stress transfer between adjacent soil elements.
- The torsional resistance evaluated in this study was assumed to be governed primarily by shaft-soil interface shear resistance. Although end-bearing contributions to torsional resistance are generally considered small relative to side shear, the test shafts were not constructed with a frictionless or isolated base. Consequently, some contribution from toe resistance may have been present during the full-scale tests. Furthermore, the FB-MultiPier Beam-on-Winkler formulation represents torsional resistance through shaft-side interaction springs and does not explicitly model torsional shear resistance at the shaft toe. While a Q-z spring is included to represent axial end-bearing behavior, the software does not account for torsional load transfer through the base of the shaft. Therefore, any toe contribution that may have been mobilized during testing could not be directly captured in the numerical models.
- The p-y and T-θ relationships implemented in FB-MultiPier were originally developed from simplified idealizations of soil-structure interaction and may not fully capture the complex stress redistribution associated with simultaneous lateral and torsional loading.

- The best-fit parameter estimation process was conducted independently for individual tests. As a result, the resulting parameter sets should not necessarily be interpreted as unique soil properties, but rather as equivalent parameters required to reproduce the observed responses.
- Soil properties were assumed uniform with depth within each model. Potential stress-dependent and depth-dependent variations in stiffness and strength were not explicitly incorporated into the analyses.
- The best-fit numerical models were developed using monotonic load responses and did not include time-dependent effects, cyclic degradation, gapping, or progressive interface deterioration that may occur under long-term field loading conditions.

6.5. Recommendations for Future Research

The findings of this study identify several areas where additional research is needed to improve understanding of drilled shaft behavior under combined lateral-torsional loading.

- Additional full-scale tests should be conducted using different shaft diameters, embedment depths, and soil profiles to evaluate the generality of the trends observed in this study.
- Future studies should investigate the influence of varying eccentricities and torque-to-lateral-load ratios on foundation performance to better quantify load interaction effects.

- The effects of cyclic and dynamic loading should be evaluated to better represent hurricane wind events and the long-term performance of mast arm foundations subjected to repeated load histories.
- Future studies should investigate the relative contributions of shaft-side resistance and shaft-toe resistance to the torsional behavior of drilled shafts. Previous full-scale studies, including the work conducted at Oregon State University, have demonstrated methods for separating these resistance components. Similar instrumentation and testing approaches could provide a more detailed understanding of torsional load-transfer mechanisms and improve the development of numerical modeling approaches for torsionally loaded foundations.
- Additional research should focus on developing direct measurements of shaft-soil interface behavior during construction and loading, particularly for drilled shafts constructed using different installation techniques.
- Numerical analyses using three-dimensional finite element methods should be performed to evaluate stress redistribution mechanisms and boundary effects that cannot be explicitly represented by Beam-on-Winkler formulations.
- Future studies should investigate stress-dependent and depth-dependent stiffness formulations to improve representation of granular soil behavior under combined loading conditions.
- Additional large-scale testing should be conducted in larger geotechnical chambers or field environments to further evaluate the influence of boundary confinement on mobilized lateral and torsional resistance.

- The experimental database developed in this study should be expanded to include multiple combined loading configurations. A larger database could support the development of practical design-oriented interaction factors or modification coefficients for use in mast arm foundation design.
- Future research should evaluate serviceability-based performance limits under combined loading conditions, with particular emphasis on acceptable rotations and lateral displacements for traffic signal structures.

This research combined full-scale experimental testing and numerical modeling to investigate the behavior of drilled shafts subjected to lateral, torsional, and combined lateral-torsional loading. The results demonstrated that construction effects, shaft-soil interface conditions, loading sequence, and load coupling significantly influence the mobilized response of drilled shaft foundations. While ultimate capacities were often similar across loading conditions, substantial differences were observed in stiffness and in the mobilization of resistance. The best-fit numerical models successfully reproduced these behaviors and provided insight into the mechanisms controlling soil-structure interaction. Collectively, the findings contribute to an improved understanding of drilled shaft performance under realistic loading conditions and support the development of future design methodologies that explicitly account for combined lateral-torsional effects.

CHAPTER 7. References

AASHTO. (2015). *LRFD Specifications for Structural Supports for Highway Signs, Luminaires, and Traffic Signals*. AASHTO.

ACI Committee 318. (2025). *Building Code for Structural Concrete Code Requirements and Commentary*.

Aguilar, V. (2018). *Torsional Resistance of Drilled Shaft Foundations* [Master, Auburn University]. https://etd.auburn.edu/handle/10415/6399

Aguilar, V., Stallings, M., Anderson, J. B., & Nowak, A. (2018). *Torsional resistance of drilled shafts* (p. 128). The Auburn University Highway Research Center.

Anderson, J. B. (1997). *A Laterally Loaded Pile Database* [Master]. University of Florida.

Basack, S., & Sen, S. (2014). Numerical Solution of Single Piles Subjected to Pure Torsion. *Journal of Geotechnical and Geoenvironmental Engineering*, *140*(1), 74-90. https://doi.org/10.1061/(ASCE)GT.1943-5606.0000964

Bridge, J., Consolazio, G., Gurley, K., DeMello, N., & Smith, J. (2018). *Wind Effects on Mast Arms* (No. 2018/127208; p. 83). Florida Department of Transportation - Research Management Center. https://rosap.ntl.bts.gov/view/dot/36439

Broms, B. (1964a). Lateral Resistance of Piles in Cohesive Soils. *Journal of the Soil Mechanics and Foundations Division*, *90*(2). https://doi.org/10.1061/JSFEAQ.0000611

Broms, B. (1964b). Lateral Resistance of Piles in Cohesionless Soils. *Journal of the Soil Mechanics and Foundations Division*, *90*(3). https://doi.org/10.1061/JSFEAQ.0000614

Brown, D., Turner, J., Castelli, R., & Loehr, E. (2018). Drilled shafts: Construction procedures and design methods. *NHI Course No. 132014*, *1*(1), 756. https://doi.org/10.1016/0886-7798(90)90101-O

Cai, Y., Chen, G., Xu, C., & Wu, D. (2006). Torsional response of pile embedded in a poroelastic medium. *Soil Dynamics and Earthquake Engineering*, *26*(12), 1143-1148. https://doi.org/10.1016/j.soildyn.2005.10.009

Campbell Scientific. (n.d.). *CR1000 measurement and control datalogger*. Retrieved July 2026, from https://www.campbellsci.com/cr1000

Chen, G., Cai, Y., Liu, F., & Sun, H. (2008). Dynamic response of a pile in a transversely isotropic saturated soil to transient torsional loading. *Computers and Geotechnics*, *35*(2), 165-172. https://doi.org/10.1016/j.compgeo.2007.05.009

Chow, Y. K. (1985). Torsional Response of Piles in Nonhomogeneous Soil. *Journal of Geotechnical Engineering*, *111*(7), 942-947. https://doi.org/10.1061/(ASCE)0733-9410(1985)111:7(942)

Chung, F., Yunchao, Y., Chaoran, X., & Kuangyuan, H. (2017). *Fatigue Resistant Design Criteria for MD SHA Cantilevered Mast Arm Signal Structures* (No. MD-17-SHA/UM/4-20; p. 85). Maryland Department of Transportation - State Highway Administration. https://www.roads.maryland.gov/OPR_Research/MD-17-SHA-UM-4-20_Signal-Poles-Fatigue_Report.pdf

Dutt, R. N., & O’Neill, M. W. (1983). Torsional Behavior of Model Piles in Sand. *Offshore Engineering Practice - Model Piles Behavior*, 315-334.

Eslami, A., & Ebrahimipour, A. (2024). Load-displacement appraisal and analysis for driven piles; a data-centric approach. *Computers and Geotechnics*, *171*, 106377. https://doi.org/10.1016/j.compgeo.2024.106377

Faquir, T., Hodges, D., & Hoke, P. (2005). *Florida Department of Transportation Hurricane Response Evaluation and Recommendations* (p. 111) [Technical Memorandum]. Florida Deparment of Transportation. www.fdot.gov/docs/default-source/traffic/traf_incident/pdf/HurricaneRprt.pdf

FlaglerLive. (2024, August). *Traffic mast arm failure in Flagler Beach*. https://flaglerlive.com/mast-arm/

GeoData. (2020). *Surface mount vibrating wire strain gauges* [Technical document]. https://www.geodata.com/wp-content/uploads/2020/07/Surface-mount-strain-gauges_20200723.pdf

Geokon. (n.d.). *Model 4900 vibrating wire load cell*. Retrieved July 2026, from https://www.geokon.com/4900

GeoLogismiki Geotechnical Software. (2022). *"CPeT-IT User's Manual v.3.0*." <https://www.geologismiki.gr/Documents/CPeT-IT/HTML/index.html>(July, 2026).

Georgiadis, M. (1987). Interaction between torsional and axial pile responses. *International Journal for Numerical and Analytical Methods in Geomechanics*, *11*(6), 645-650. https://doi.org/10.1002/nag.1610110609

Georgiadis, M., & Saflekou, S. (1990). Piles Under Axial and Torsional Loads. *Computer and Geotechnics*, *9*, 291-305.

Getty Images. (2024, October 10). *Traffic light pole down in downtown Orlando after Hurricane Milton* [Photograph]. https://www.gettyimages.co.uk/detail/news-photo/traffic-light-pole-is-down-in-downtown-orlando-florida-due-news-photo/2177021883

Guo, W. D., Chow, Y. K., & Randolph, M. F. (2007). Torsional Piles in Two-Layered Nonhomogeneous Soil. *International Journal of Geomechanics*, *7*(6), 410-422. https://doi.org/10.1061/(ASCE)1532-3641(2007)7:6(410)

Guo, W. D., & Randolph, M. F. (1996). Torsional piles in non-homogeneous media. *Computers and Geotechnics*, *19*(4), 265-287. https://doi.org/10.1016/S0266-352X(96)00009-2

Hache, R. A. G., & Valsangkar, A. J. (1988). Torsional Resistance of Single Pile in Layered Soil. *Journal of Geotechnical Engineering*, *114*(2), 216-220. https://doi.org/10.1061/(ASCE)0733-9410(1988)114:2(216)

Hu, Z. (2003). *Determining the Optimum Depth of Drilled Shafts Subject to Combined Torsion and Lateral Loads in Saturated Sand from Centrifuge Testing* [Master]. University of Florida.

Hu, Z., McVay, M., Bloomquist, D., Herrera, R., & Lai, P. (2006). Influence of Torque on Lateral Capacity of Drilled Shafts in Sands. *Journal of Geotechnical and Geoenvironmental Engineering*, *132*(4), 456-464. https://doi.org/10.1061/(ASCE)1090-0241(2006)132:4(456)

Huang, J. (2019). *Performance of Drilled Shaft Under Combination of Complicated Loads under Hurricane Event* (No. 18GTTSA02; p. 82). The University of Texas at San Antonio.

Kalavar, S., & Ealy, C. (2000). FHWA Deep Foundation Load Test Database. *New Technological and Design Developments in Deep Foundations*, 192-206. https://doi.org/10.1061/40511(288)14

Li, Q., Stuedlein, A. W., & Barbosa, A. R. (2017). Torsional Load Transfer of Drilled Shaft Foundations. *Journal of Geotechnical and Geoenvironmental Engineering*, *143*(8), 04017036. https://doi.org/10.1061/(ASCE)GT.1943-5606.0001701

Matlock, H. (1970). Correlation for Design of Laterally Loaded Piles in Soft Clay. *All Days*, OTC-1204-MS. https://doi.org/10.4043/1204-MS

McVay, M., Bloomquist, D., & Thiyyakkandi, S. (2014). *Field Testing of Jet-Grouted Piles and Drilled Shafts* (Nos. BDK75-977-41; p. 314). Florida Deparment of Transportation. https://rosap.ntl.bts.gov/view/dot/26983

MSN News. (2024). *Hurricane Helene: Car survives landslide in North Carolina*. https://www.msn.com/en-us/news/us/hurricane-helene-car-survives-landside-in-north-carolina-see-the-damage/ar-AA1rc7px

Ohio Power Tool. (n.d.). *Power Team SPX RH6010 hydraulic cylinder*. Retrieved July 2026, from https://www.ohiopowertool.com/power-team-spx-rh6010

Okafor, C. C. (2024). *Full Scale Testing and Three-Dimensional Numerical Simulation of a Mechanically Reinforced-Earth System*.

Poulos, H. G. (1975). Torsional Response of Piles. *Journal of the Geotechnical Engineering Division*, 1019-1035.

Prakash, S., & Sharma, H. D. (1990). *Pile foundations in engineering practice*. John Wiley & Sons, Inc.

Randolph, M. F. (1983). Design Considerations for Offshore Piles. *Offshore Engineering Practice - Offshore Piles Design*, 422-439.

Reese, L. C., Cox, W. R., & Koop, F. D. (1974). Analysis of Laterally Loaded Piles in Sand. *All Days*, OTC-2080-MS. https://doi.org/10.4043/2080-MS

Rodriguez, C. M., Pando, M. A., Whelan, M., Weggel, D., & Fang, H. (2020). *State of Practice and Literature Review on Foundations for Coastal Traffic Signal Mast Arm Structures* (p. 120).

Rollins, K. M., Gerber, T. M., Lane, J. D., & Ashford, S. A. (2005). Lateral Resistance of a Full-Scale Pile Group in Liquefied Sand. *Journal of Geotechnical and Geoenvironmental Engineering*, *131*(1), 115-125. https://doi.org/10.1061/(ASCE)1090-0241(2005)131:1(115)

Samtani, N. C., & Nowatzki, E. A. (2006). Soils and Foundations Reference Manual-Volume II. Federal Highway Administration – FHWA-NHI-06-088.

Tawfiq, K. (2000). *Drilled Shaft Under Torsional Loading Conditions* (No. WPI 0510704; p. 319). Florida Department of Transportation. https://trid.trb.org/View/655455

TE Connectivity. (n.d.). *Cable-actuated position sensors*. Retrieved July 2026, from https://www.te.com/en/products/sensors/position-sensors/potentiometer-sensors/cable-actuated-position-sensors.html

The Virginian-Pilot. (2024, August 8). *Traffic light structure falls on car in Newport News*. https://www.pilotonline.com/2024/08/08/traffic-light-structure-falls-on-car-newport-news/

Thiyyakkandi, S., McVay, M., Lai, P., & Herrera, R. (2016). Full-scale coupled torsion and lateral response of mast arm drilled shaft foundations. *Canadian Geotechnical Journal*, *53*(12), 1928-1938. https://doi.org/10.1139/cgj-2016-0241

Thiyyakkandi, S., McVay, M., Lai, P., & Herrera, R. (2017). Suitability of jetted and grouted precast pile for supporting mast arm structures. *Canadian Geotechnical Journal*, *54*(9), 1231-1244. https://doi.org/10.1139/cgj-2016-0467

TML. (n.d.). *Foil strain gauges*. Tokyo Measuring Instruments Laboratory Co., Ltd. Retrieved July 2026, from https://tml.jp/e/product/strain_gauge/wf_list.html

Tommy, A., Widjaja, B., & Hutabarat, G. M. (2023). *P-y Curve for Estimation Lateral Bearing Capacity of Single Bored Pile in Overconsolidated Soils Using The Three-Dimensional Finite Element Method.* 10. https://doi.org/10.1088/1755-1315/1249/1/012028

Wang, K., Zhang, Z., Leo, C. J., & Xie, K. (2008). Dynamic torsional response of an end bearing pile in saturated poroelastic medium. *Computers and Geotechnics*, *35*(3), 450-458. https://doi.org/10.1016/j.compgeo.2007.06.013

Zhang, L. (2010). Nonlinear Analysis of Torsionally Loaded Piles in a Two-Layer Soil Profile. *International Journal of Geomechanics*, *10*(2), 65-73. https://doi.org/10.1061/(ASCE)GM.1943-5622.0000038

Appendix A. Structural Design of the Drilled Shafts

Design Input Data

Shaft Diameter: 36 in. Concrete Cover: 3.0 in.

Longitudinal Reinforcement: 14 #8 Ties: #4 ties @ 6 in. c/c

Applied Loads

Moment (Mu): 105 kip-ft Shear (Vu): 120 kip

Axial (Pu): 4 kip

Torsion (Tu): 140 kip-ft

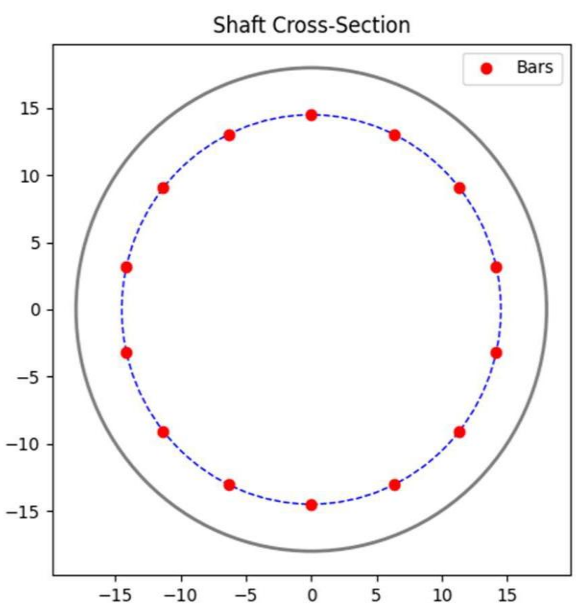

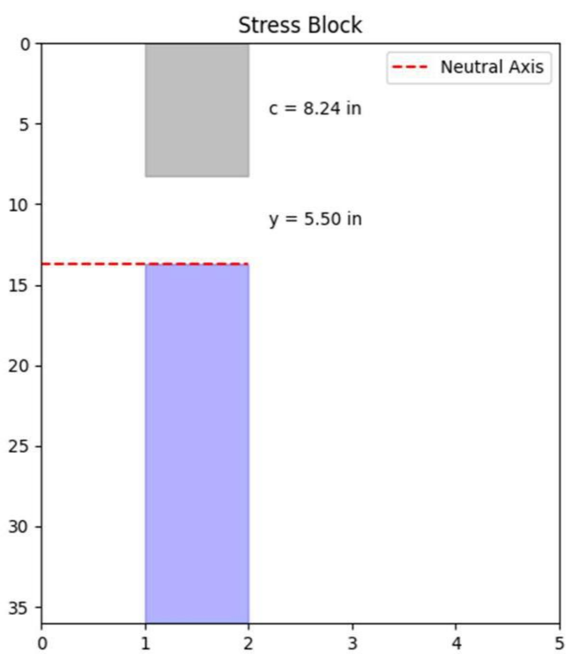

Flexural Design Summary

Flexural Design Summary (ACI 318):

Step 1: Compute required compression block area

A_comp = (As · fy) / (0.85 · fc)   [ACI 318-19 Eq. 22.2.2.4.1]

Step 2: Solve for circular segment depth a such that segment_area(a) = A_comp

[Geometry of circular segment]

Step 3: Calculate neutral axis depth

c = a / β_1 and y = (0.002/0.003) · c   [ACI 318-19 22.2.2.4.3]

Step 4: Determine effective depth d = average tension-bar depth

Step 5: Compute nominal moment

Mn = φ · As · fy · (d − a/2) [ACI 318-19 22.3.1.1]

Step 6: Mn must be greater than Mu [ACI 318-19 Eq. 10.5.1.1]

Results:

a = 7.008 in

c = 8.244 in

y = 5.496 in

Mn = 747.24 kip-ft

Mu = 105.00 kip-ft

Flexural Check = Sufficient

Longitudinal Reinforcement Limits (10.6.1.1):

ρ_provided = 1.09%

ρ_min = 1.00%, ρ_max = 8.00%

Min Check → PASS

Max Check → PASS

Shear Design Summary

Shear Design Summary (ACI 318):

Step 1: Compute concrete contribution

Vc = 2√f'c · b · d [ACI 318-19 Table 22.5.5.1] *ignores axial component

Step 2: Compute steel contribution

Vs = (Av · fy · d) / s [ACI 318-19 22.5.8.3]

Step 3: Combine and apply strength reduction

Vn = φ · (Vc + Vs) [ACI 318-19 Eq. 22.5.1.1]

Step 4: Vn must be greater than Vu [ACI 318-19 Eq. 10.5.1.1]

Results:

dh = 30.500 in

Vc = 138.89 kip

Vs = 61.00 kip

Vn = 149.92 kip

Vu = 120.00 kip

Shear Check = Sufficient

Minimum Shear Reinforcement:

Required? Yes [ACI 318-19 10.6.2.1]

Av1 = 0.171 in² [ACI 318-19 10.6.2.2(a)]

Av2 = 0.180 in² [ACI 318-19 10.6.2.2(b)]

$Av\_min = 0.180 in^2$

$Av\_provided = 0.400 in^2$ → PASS

Axial Design Summary

Axial Design Summary (ACI 318):

Step 1: Compute concrete compression

Pc = 0.85.f'c · (Ac - Ast) [ACI 318-19 22.4.2.2]

Step 2: Compute steel compression

Ps = fy · Ast [ACI 318-19 22.4.2.2]

Step 3: Combine and apply φ

Pn = φ · (Pc + Ps) [ACI 318-19 22.4.2.1]

Step 4: Pn must be greater than Pu [ACI 318-19 Eq. 10.5.1.1]

Results:

Pn = 2799.08 kip

Pu = 4.00 kip

Axial Check = Sufficient

Longitudinal Reinforcement Limits (10.6.1.1):

ρ_provided = 1.09%

ρ_min = 1.00%, ρ_max = 8.00%

Min Check → PASS

Max Check → PASS

Torsion Design Summary

Torsion Design Summary (ACI 318):

Step 1: Threshold torsion

$T\_threshold = \sqrt{f'c} \cdot Acp^2 / Pcp$ [ACI 318-19 Eq. 22.7.4.1(a)]

Step 2: Cracking torsion

$Tcr = 4\sqrt{f'c} \cdot Acp^2 / Pcp$ [ACI 318-19 Eq. 22.7.4.1(b)]

Step 3: Nominal torsion

$Tn = \varphi \cdot 2Ao \cdot At \cdot fy / (s \cdot \tan\theta)$ [ACI 318-19 22.7.6.1a]

Step 4: Tn must be greater than Tu [ACI 318-19 Eq. 10.5.1.1]

Results:

T_threshold = 48.28 kip-ft

Tcr = 193.13 kip-ft

Tn = 182.80 kip-ft

Tu = 140.00 kip-ft

Torsion Check = Sufficient

Appendix B. Headed Anchors Bolt Design

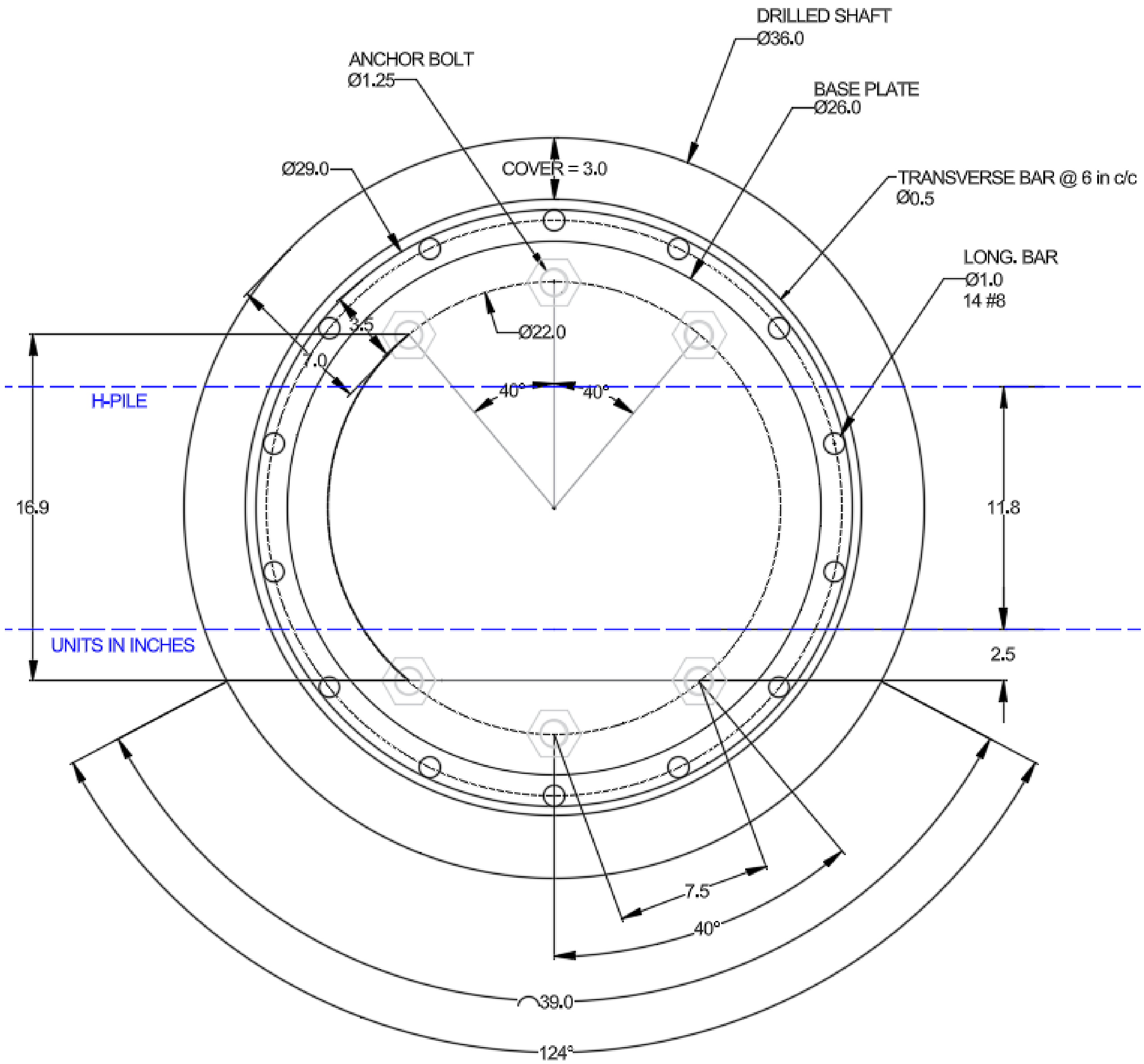

Depth of embedment (in) - h_{ef}	30
Bolt diameter (in) - do	1.25
Center-to-center diameter of bolts (in) - db	22
Number of bolts - n	6
Specified yield strength of anchor steel (ksi) - f_{ya}	120
Minimum anchor spacing (in) - s	7
Maximum anchor spacing (in) - s_{max}	7.5
Anchor-edge distance (in) - c	16.85
Influencing edge distance (in) - c_{a1}	5.21
Maximum influencing edge distance (in) - c_{a1max}	5.21

TENSILE STRENGTH – CH17.6

- **Steel strength of anchor (individual anchor in a group) in tension, N_{sa}**

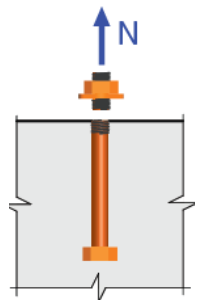

$N_{sa} = A_{se,N} f_{uta}$ =	**153.4 kips**	*17.6.1.2*
$A_{se,N}$ – Effective cross-sectional area of an anchor in tension	1.227 in^2	
f_{uta} – Specified tensile strength of anchor steel	125 ksi	
Reduction factor, ϕ =	0.75	
ϕN_{sz} – Reduced steel strength of one anchor in tension =	**115.1 kips**	

- **Concrete breakout strength of anchors (anchors as a group) in tension, N_{cbg}**

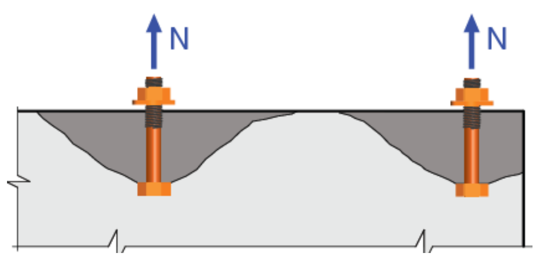

Critical Spacing = $3h_{ef}$		17.5.1.4.1
For a single anchor	$N_{cb} = \frac{A_{Nc}}{A_{Nco}} \psi_a \psi_{ed,N} \psi_{c,N} \psi_{cp,N} \psi_{cm,N} N_b$	*17.6.2.1 a*
For an anchor group	$N_{cbg} = \frac{A_{Nc}}{A_{Nco}} \psi_a \psi_{ec,N} \psi_{ed,N} \psi_{c,N} \psi_{cp,N} \psi_{cm,N} N_b$	*17.6.2.1 b*
h'_{ef} (in)	$h'_{ef} = max\left(\frac{c_{a,max}}{1.5\frac{s}{3}}()\right)$ = 3.48 in	*17.6.2.1 .2*
A_{Nc} – Total projected area for anchor group =	326.091 in^2	
A_{Nco} - Projected concrete failure area of a single anchor if not limited by edge distance or spacing.	$A_{Nco} = 9h'^{2}_{ef}$ = 108.7 in^2	*17.6.2.1.4*

Ψ_a – Anchor strength modification factor =	0.95	*17.5.4.1*
$\Psi_{ec,N}$ – Breakout eccentricity factor	$\psi_{ec,N} = \frac{1}{\left(1+\frac{e'_N}{1.5h_{ef}}\right)} \leq 1.0$= 0.296	*17.6.2.3.1*
$\Psi_{ed,N}$ – Breakout edge factor	$\psi_{ed,N} = 0.7 + 0.3\frac{c_{a,min}}{1.5h_{ef}}$= 0.735	*17.6.2.4.1b*
$\Psi_{c,N}$ – Breakout cracking factor =	1.0	*17.6.2.5*
$\Psi_{cp,N}$ – Breakout splitting factor =	1.0	*17.6.2.6.2*
$\Psi_{cm,N}$ – Breakout compression field factor =	1.0	*17.6.2.7.2*
N_b – Basic single anchor concrete breakout strength	$N_b = k_c\lambda_a(\sqrt{f_c'})(h'_{ef})^{1.5}$= **270.6 kip**	*17.6.2.2*
N_{cbg} – Nominal concrete breakout strength in tension for the anchor group =	**168 kips**	
Reduction factor, ϕ =	0.75	
ϕN_{cbg} – Reduced concrete breakout in tension for the anchor group =	**126 kips**	

- **Pullout strength of a single cast-in anchor, N_{pn}**

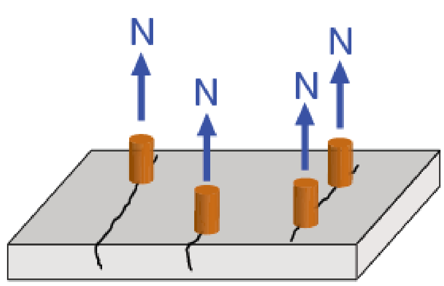

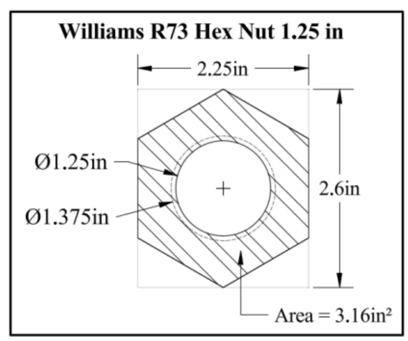

$N_{pn} = \psi_a\psi_{c,P}N_p$ =	**108.1 kip**	*17.6.3.1*
Ψ_a – Anchor stress modification factor =	0.95	*17.5.4.1*
$\Psi_{c,P}$ – Pullout cracking factor =	1.0	*17.6.3.3*
N_p – Basic single anchor pullout strength	$N_p = 8A_{brg}f_c'$ = 113.760 kip	*17.6.3.2.2a*
A_{brg} – Net bearing area of the head of the anchor bolt	3.16 in^2	
Reduction factor, ϕ =	0.75	
ϕN_{pn} – Reduced pullout strength of a single anchor =	**81.1 kip**	

- **Concrete side-face blowout strength of headed anchor in tension, N_{sb}**

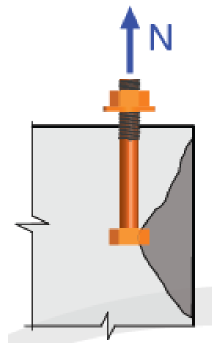

If $h_{ef} > 2.5c_{a1}$

$N_{sb} = \psi_a 160 c_{a1}\sqrt{A_{brg}}\lambda_a\sqrt{f_c'}$ = **2987.9 kips** *17.6.4.1*

Ψ_a – Anchor stress modification factor = 0.95 *17.5.4.1*

c_{a1} - Influencing edge distance = 5.32 in

For group anchor $N_{sbg} = \left(1 + \frac{s}{6c_{a1}}\right) N_{sb}$ = **3704.4 kips** *17.6.4.2*

s - Min Anchor spacing = 7.5 in

Reduction factor, ϕ = 0.75

ϕN_{sbg} – Reduced concrete side-face blowout strength for the anchor group **2778.3 kips**

SHEAR STRENGTH – CH 17.7

- **Steel strength of anchor in shear (individual anchor in a group), V_{sa}**

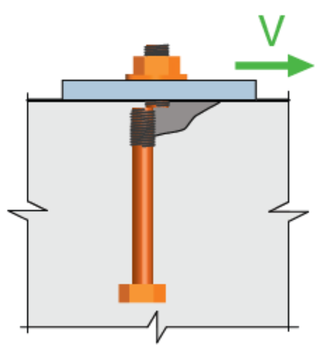

$V_{sa} = 0.6A_{se,V}f_{uta}$ = **72.7 kips** *17.7.1.2b*

$A_{se,V}$ – Effective cross-sectional area of an anchor = 0.969 in^2

$f_{uta} = min(1.9f_{ya}, 125ksi)$ = 125 ksi

Reduction factor, ϕ = 0.75

ϕV_{sa} – Reduced steel strength of an anchor in shear = **54.5 kips**

- **Concrete breakout strength of anchor in shear, V_{cb}**

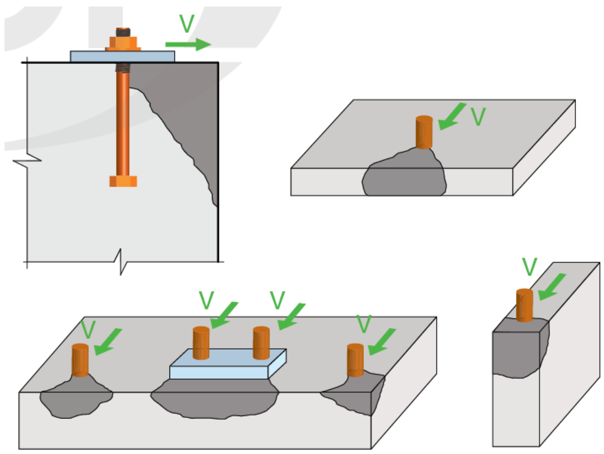

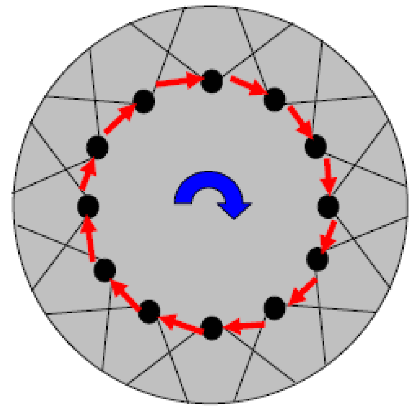

Shear failure causing concrete breakout of an anchor, oriented parallel to the edge on a circular foundation (Cook and Halcovage, 2007).

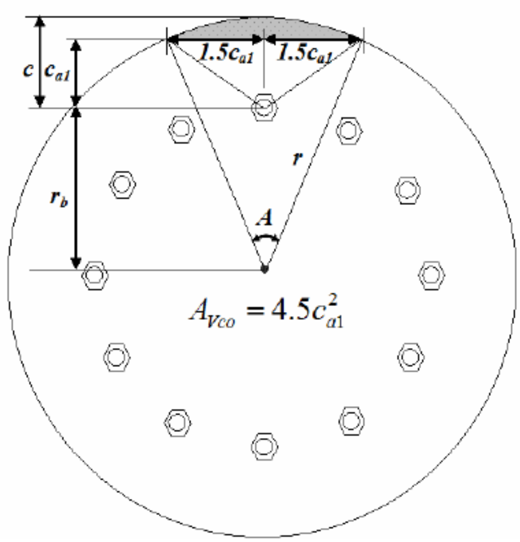

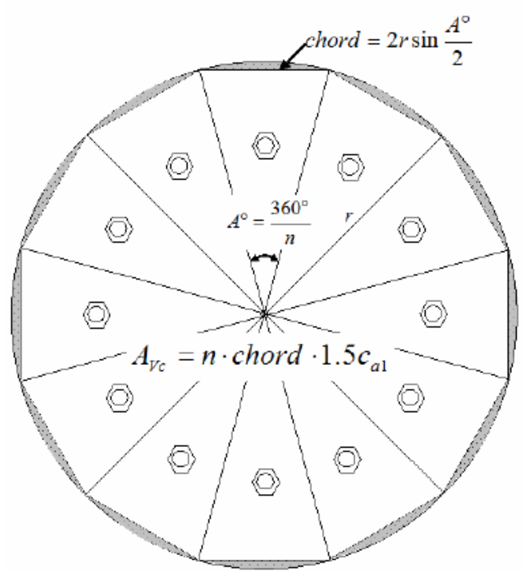

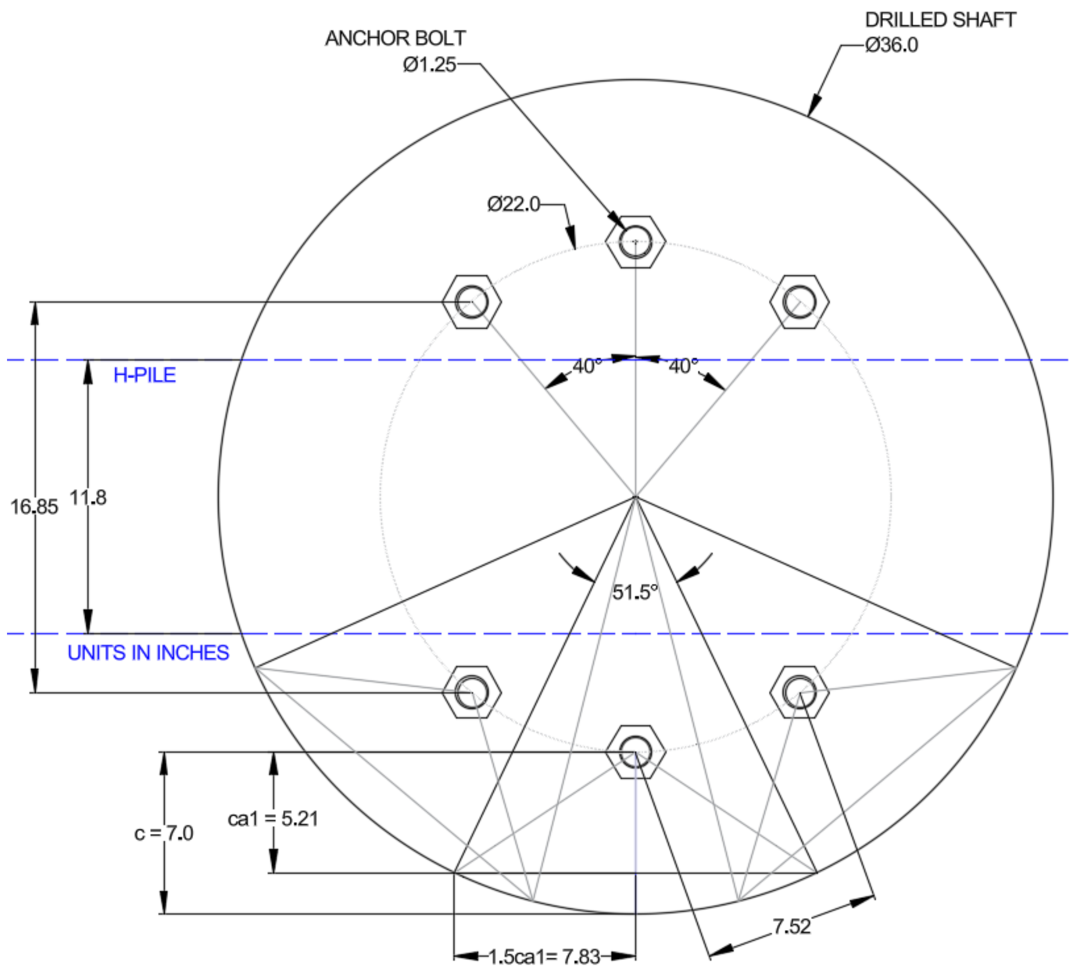

Shear perpendicular to the edge on a single anchor	$V_{cb} = \frac{A_{Vc}}{A_{Vco}}\psi_a\psi_{ed,V}\psi_{c,V}\psi_{h,V}V_b$	*17.7.2.1a*
Shear perpendicular to the edge on an anchor group	$V_{cbg} = \frac{A_{Vc}}{A_{Vco}}\psi_a\psi_{ec,V}\psi_{ed,V}\psi_{c,V}\psi_{h,V}V_b$	*17.7.2.1b*
A_{Vc} – Total projected area for anchor group =	733.705 in^2	
A_{Vco} – Maximum projected area of a single anchor	$A_{Vco} = 4.5{c_{a1}}^2$= 122.284 in^2	
Ψ_a – Anchor strength modification factor =	0.95	*17.5.4.1*
$\Psi_{ec,V}$ – Breakout eccentricity factor	$\psi_{ec,V} = \frac{1}{\left(1+\frac{e'_V}{1.5c_{a1}}\right)} \le 1.0$= 1.0	*17.7.2.3.1*
$\Psi_{ed,V,}$ – Breakout edge effect factor	= 1.0 (for shear parallel to an edge)	*17.7.2.4.1a*
$\Psi_{c,V}$ – Breakout cracking factor =	1.2	
$\Psi_{h,V}$ – Breakout thickness factor =	1.0	*17.7.2.6.1*

V_b – Basic single anchor concrete breakout strength	= **17.6**
V_{cbg} – Nominal concrete breakout strength in shear for the anchor group =	**104.3 kips**
$V_{cbg\_parallel}$ =	**208.6 kips**
$T_{n.breakout}$ =	**2294.3 kip-in**
Reduction factor, ϕ =	0.75
$\phi T_{n.breakout}$ =	**1985.1 kip-in**

- **Concrete pryout strength of anchor in shear, V_{cpg}**

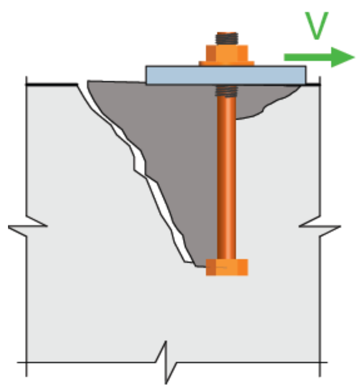

$V_{cpg} = k_{cp}N_{cpg}$ = **336 kip** *17.7.3.1b*

$N_{cpg} = N_{cbg}$ = 167.985 kip

k_{cp} = 2